Strong Modulation of THz Optical Properties of Layered Materials by Thermal and Ultrafast Heating

Im Fachbereich Physik
der Freien Universität Berlin
eingereichte Dissertation

Martin Scheuch

August 2012

Diese Arbeit entstand in der Arbeitsgruppe von Prof. Dr. Martin Wolf
an der Freien Universität Berlin
und dem Fritz-Haber-Institut der Max-Planck-Gesellschaft

Berlin, im August 2012

Erstgutachter: Prof. Dr. Martin Wolf
Zweitgutachter: Prof. Dr. Karsten Heyne

Datum der Disputation: 15. Oktober 2012

Wahr sind auch die Erinnerungen, die wir mit uns tragen;
die Träume, die wir spinnen, und die Sehnsüchte, die uns treiben.
Damit wollen wir uns bescheiden.

Heinrich Spoerl, *Die Feuerzangenbowle*

Contents

Introduction

Optical properties of materials are of key relevance for various applications, for instance data transfer through optical fibers. For light at optical frequencies, sources (e.g. lasers), detectors (such as photodiodes) and passive or active devices (such as lenses, filters and modulators) are readily available. However, the so-called terahertz (THz) frequency window is still underexplored. It extends from about 0.3 to 30 THz, thus covering the far-infrared and lower part of the mid-infrared spectral region. THz radiation is highly relevant for basic research and spectroscopy, as many resonances or excitations of physical systems are located at these frequencies [THM+11]. Examples are rotations and vibrations of molecules, intraband transitions in semiconductors and energy gaps in superconductors. THz radiation is also under consideration as an information carrier in short-range wireless communication at THz bit rates, thereby potentially replacing current GHz-based technology [FM10].

Such exciting applications require the ability to actively modulate the propagation of THz radiation. Several methods have been used to achieve this goal, such as modulation via a magnetic field [CTPP03, OeYK+06, BMR+12], via an electric field [YLC+12] or via application of periodic arrays [IRH09]. However, modulation could also be realized by temperature variation, provided the THz-optical properties of the modulator material are sensitive to this perturbation. Promising candidates are materials that exhibit strongly temperature-dependent low-energy excitations. In this thesis, several examples of such materials are investigated: the semimetal graphite and the superconductors $Bi_2Sr_2CaCu_2O_{8+\delta}$ and MgB_2.

The semimetal graphite has a small Fermi surface and a rapidly varying electronic density of states around the Fermi energy, which is in sharp contrast to most metals. Therefore, thermally and optically excited electrons should affect the strength of optical interband transitions around the Fermi energy [KPS+05,PLM+04]. We further consider superconductors, which exhibit a band gap in the ground state, making them transparent at certain frequency intervals in the THz range. Upon heating, the superconductor turns into a normal metal without band gap, which leads to a strong increase of the absorption of THz radiation.

This Thesis

In this thesis, the THz-optical properties of graphite and superconducting compounds are investigated by means of THz spectroscopy, both for samples in equilibrium as well as after photoexcitation with a femtosecond laser pulse. We monitor the THz-optical properties as a function of temperature or of delay since sample excitation. Appropriate modeling will provide insights into the microscopical processes that govern the THz response of these materials and their ultrafast dynamics. The following issues are addressed in detail:

- How do the peculiar electronic and phononic properties of graphite around the Fermi energy affect its optical properties? How does photoexcitation affect the optical properties? What are the mechanisms of energy relaxation after photoexcitation?
  We find that graphite shows a significant bleaching of about 20% for THz radiation following heating or photoexcitation. A two-step process of energy relaxation is found: on

a femtosecond timescale, electrons thermalize and concurrently heat few strongly coupled optical phonons, followed by phonon cooling on a picosecond timescale.

- How does the superconducting phase transition affect the THz optical properties of superconductors? Are there differences between cuprates and BCS-type superconductors? How does photoexcitation affect the superconducting state?
  Thermal heating or photoexcitation leads to a phase transition and increased absorption of THz radiation. Also, an indication for a pseudogap phase is found for the cuprate supercondcutor $Bi_2Sr_2CaCu_2O_{8+\delta}$.

Answering these questions required some effort in experiment as well as theoretical modeling. For this purpose, an existing THz spectrometer was extended to enable temperature-dependent measurements with high accuracy. Due to the transmission geometry chosen, thin samples on THz transparent substrates were needed. Hence, much attention was paid to sample preparation of graphite and $Bi_2Sr_2CaCu_2O_{8+\delta}$. For MgB_2, larger crystals have not been available so far, thus a new method of sample growing was realized in a collaborating group from the Universität Bielefeld. In order to gain a microscopic understanding of the THz optical properties of graphite, linear-response theory including band structure information was used. A new approach to quasi-equilibrium properties has been successfully implemented by using pump-probe technique that extends the scope of equilibrium measurements.

Chapter 1

Theoretical Background

Solids exhibit various fundamental excitations, such as lattice vibrations and electronic transitions. These excitations rule e.g. the conductivity as well as the energy relaxation in a material, which renders a detailed understanding necessary. In graphite, the electron-phonon coupling is of special interest, since here, excited electrons thermalize and subsequently relax via phonon-mediated cooling. One piece of the puzzle to an understanding is electron pairing. The theoretical description of all mentioned excitations is presented in Section 1.1.

Due to its peculiar small Fermi surface and the rapidly changing electronic density of states around the Fermi energy, graphite is a promising candidate for applications in electronics and optics. Superconductors are found to have a bandgap of some 10 meV around the Fermi level which determines the temperature dependence of the superconducting state. Especially low-energy excitations should be highly sensitive to temperature changes. Thus, optical properties should exhibit significant changes with temperature for low-energy excitations in the cases of graphite and superconductors. Therefore, Section 1.2 introduces the microscopic concept of the dielectric function $\varepsilon(\omega)$ that is measured in optical experiments.

For the study of low-energy excitations in the vicinity of the Fermi level, electromagnetic radiation in the THz range provides the tool of choice due to its photon energy in the meV range. Therefore, the generation of THz radiation by application of ultrashort laser pulses to induce nonlinear processes in matter will be discussed in Section 1.3 followed by the presentation of the phase and amplitude sensitive electro-optic sampling.

1.1 Fundamental Excitations in Solids

Solids exhibit various different fundamental excitations in equilibrium. These excitations are characterized by different energy scales, such as:

- lattice vibration, so-called phonons ($\Delta E \sim 0.1$ eV),
- electronic transitions ($\Delta E \sim 1$ eV),
- bound electron pairs, so-called Cooper pairs ($\Delta E \sim 0.01$ eV),
- bound electron-hole pairs, so-called excitons ($\Delta E \sim 0.01$ eV),
- core-level transitions ($\Delta E \sim 10$ eV).

These excitations can be probed using light-matter interaction in experiments where scattered light is measured. If one wants to probe low-energy exciations, THz radiation is well-suited, since 1 THz$\hat{=}$4.1 meV.

Below, the considered interactions of phonons and electrons are introduced first separately, then in terms of electron-phonon coupling (EPC) that will lead to Cooper pairs.

1.1.1 Separation of Different Degrees of Freedom

In general, the hamiltonian, including all interaction of a many-particle system, is given by

$$\hat{H} = \hat{H}_{\text{ion}} + \hat{H}_{\text{e}} + \hat{H}_{\text{e-ion}} \, .$$

It is necessary to decouple different degrees of freedom and consider their interaction with only limited partners and a background potential. This will be done in the following sections.

The large ionic mass M leads to a simplification that allows us to treat the problem in two distinct steps, the so-called Born-Oppenheimer approximation [BO27, FW03, Czy04]:

1. Due to their small amplitude and slow motion, the ions may be considered as fixed at their equilibrium position to compute the electrons' behavior.
2. The low-frequency ionic motion can be computet by assuming the electrons to have their wave function appropriate to the instantaneous ionic configuration, i.e. treating the eigenenergies of the electronic states as the effective potentials of the ions.

Thus, in a good approximation, the electronic system and the ionic system are considered decoupled. A closer look reveals different time scales for both systems: the electrons see a quasi-static potential formed by the ions even when they are in motion since the electronic system matches the ionic motion instantaneously. Then, the ionic motion is treated as a perturbation to the electronic system, leading to the EPC, since the limit of the Born-Oppenheimer approximation is given by the ratio of electron and ion mass:

$$\left(\frac{m}{M}\right)^{1/4} \approx 10^{-1} - 10^{-2} \, . \tag{1.1}$$

1.1.2 Lattice Vibration

Since lattice and electrons are considered to be decoupled, the lattice vibrations shall discussed first. Consider N ion masses M_l with interaction $V(\boldsymbol{R}_1, \ldots, \boldsymbol{R}_N)$. Then the hamiltonian is given by

$$H = \sum_{l=1}^{N} \frac{\boldsymbol{P}_l^2}{2M_l} + V(\boldsymbol{R}_1, \ldots, \boldsymbol{R}_N) \, .$$

The equilibrium positions of the ions may be $\boldsymbol{R}^0 = \left(\boldsymbol{R}_1^0, \ldots, \boldsymbol{R}_N^0\right)$. For small changes $\boldsymbol{R}_l = (R_{l1}, \ldots, R_{ld}) = \boldsymbol{R}_l^0 + \boldsymbol{u}_l$ with $\alpha = 1, \ldots, d$, the dimension in cartesian coordinates, one can expand the interaction potential into a series:

$$V(\boldsymbol{R}_1, \ldots, \boldsymbol{R}_N) = V\left(\boldsymbol{R}^0\right) + \sum_{l\alpha} u_{l\alpha} \left.\frac{\partial V}{\partial R_{l\alpha}}\right|_{\boldsymbol{R}^0} + \frac{1}{2} \sum_{l\alpha, m\beta} u_{l\alpha} u_{m\beta} \left.\frac{\partial^2 V}{\partial R_{l\alpha} \partial R_{m\beta}}\right|_{\boldsymbol{R}^0} + \mathcal{O}^3 \, . \tag{1.2}$$

Since zero and first order terms vanish, only the second order term contributes.

A crystal showing a Bravais lattice and N unit cells with a base consisting of r atoms and periodic boundary conditions in reciprocal space $(\boldsymbol{R}, t) \to (\boldsymbol{q}, \omega)$ then yields:

- N non-equivalent wavevectors $\boldsymbol{q}$ in the first Brillouin zone (BZ),
- Nrd eigenfrequencies $\omega_\eta(\boldsymbol{q})$.

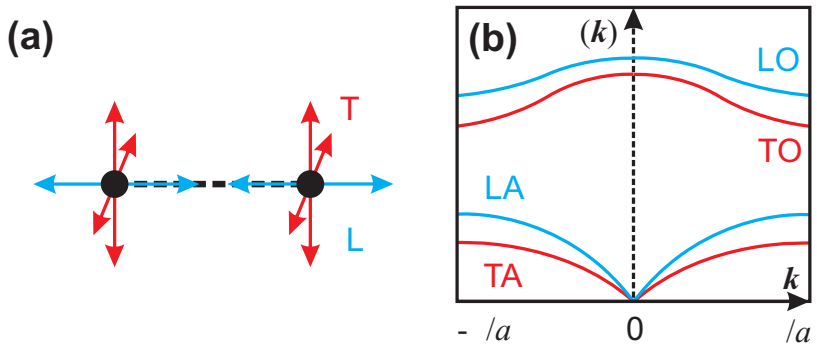

Figure 1.1: *(a) Ionic motion of two atoms in transversal (T) and longitudinal (L) direction. (b) Schematic of the resulting dispersion relation including acoustic and optical branches.*

The hamiltonian in second quantization is given by [Czy04]:

$$\hat{H}_{\text{harm}} = \sum_{\boldsymbol{q}} \sum_{\eta=1}^{rd} \hbar\omega_\eta\left(\boldsymbol{q}\right)\left(\hat{b}^\dagger_{\eta\boldsymbol{q}}\hat{b}_{\eta\boldsymbol{q}} + \frac{1}{2}\right),$$

introducing annihiliation and creation operators $\hat{b}^\dagger, \hat{b}$, fulfilling the bosonic commutator relations [FW03, GR86]. Eigenenergies then are given by

$$E = \sum_{\eta\boldsymbol{q}} \hbar\omega_\eta\left(n_{\eta\boldsymbol{q}} + \frac{1}{2}\right),$$

with occupation numbers $n_{\eta\boldsymbol{q}} \in \mathbb{N}$. Each state can be occupied various times and for all $\boldsymbol{q}$, there exist rd frequencies $\omega_{\eta\boldsymbol{q}}$, i.e. the phonon dispersion shows rd branches. All $\omega_\eta\left(\boldsymbol{q}\right)$ are periodic concerning a reciprocal lattice vector $\boldsymbol{G}$. For d branches, the dispersion is linear around $|\boldsymbol{q}| = 0$ and $\omega_\eta\left(\boldsymbol{q}\right) \to 0$ for $|\boldsymbol{q}| \to 0$. These d branches are called *acoustic*, since their motion corresponds to acouctic waves. The remaining $d(r-1)$ branches are called *optical*, since atoms in the unit cell oscillate against each other leading to large dipole moments in ionic crystals. In some contexts it is useful to additionally distinguish the displacement parallel or perpendicular to the wave vector $\boldsymbol{q}$, called longitudinal and transversal, respectively. A sketch is shown in Figure 1.1(a). Thus, we discern:

- *LO*: longitudinal optical phonon branches,
- *LA*: longitudinal acoustic phonon branches,
- *TO*: transversal optical phonon branches, and
- *TA*: transversal acoustic phonon branches.

A scheme of the resulting dispersion relation $\omega(\boldsymbol{k})$ is shown in Figure 1.1(b). Optical branches usually obtain higher energies than acoustic branches. Thus the highest phonon energies are found in LO branches, while TA and LA modes are of lower energy as can be found in thermal excitations. High energy phonon branches will play a major role in energy relaxation in graphite as well as in superconductivity in magnesium diboride, in both cases due to the strong EPC.

$\hat{H}_{\text{harm}}$ describes a system of non-interacting bosons, the so-called phonons. Here, the Bose-Einstein distribution function applies in equilibrium:

$$\langle\, n_{\eta\boldsymbol{q}} \,\rangle = b(E,T) = \frac{1}{e^{\hbar\omega/kT} - 1}\,. \tag{1.3}$$

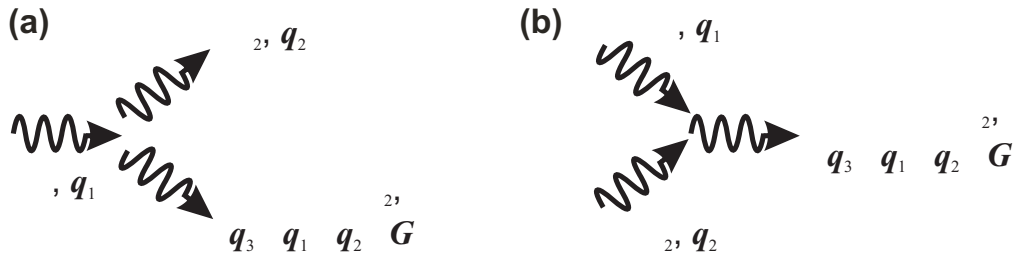

Figure 1.2: *Schematic of three phonon processes: (a) decay of phonon (1) with energy $\hbar\omega_1$ into two phonons (2) and (3) with energies $\hbar\omega_2$ and $\hbar\omega_1 - \hbar\omega_2$, respectively; (b) creation of phonon (3) with energy $\hbar\omega_1 + \hbar\omega_2$, the sum in energy of (1) and (2). In all processes momentum conservation is found.*

Phonon-Phonon Interaction

Phonons have an infinite lifetime, hence phonon-phonon interaction has to be included to $\hat{H}_{\mathrm{harm}}$ from Equation (1.2). Here, expansion to third order leads to:

$$V^3 = \frac{1}{6}\sum_{nml}\sum_{\alpha\beta\gamma} u_{n\alpha}u_{m\beta}u_{l\gamma}\left.\frac{\partial^3 V}{\partial R_{n\alpha}\partial R_{m\beta}\partial R_{l\gamma}}\right|_{\boldsymbol{R}^0} .$$

For further insight, one rewrites this expression in terms of creation and annihilation operators:

$$V^3 = \sum_{\boldsymbol{q}_1\lambda_1,\boldsymbol{q}_2\lambda_2,\boldsymbol{q}_3\lambda_3} D^{\lambda_1\lambda_2\lambda_3}_{\boldsymbol{q}_1\boldsymbol{q}_2\boldsymbol{q}_3}\left(\hat{b}_{\boldsymbol{q}_1\lambda_1}+\hat{b}^\dagger_{-\boldsymbol{q}_1\lambda_1}\right)\left(\hat{b}_{\boldsymbol{q}_2\lambda_2}+\hat{b}^\dagger_{-\boldsymbol{q}_2\lambda_2}\right)\left(\hat{b}_{\boldsymbol{q}_3\lambda_3}+\hat{b}^\dagger_{-\boldsymbol{q}_3\lambda_3}\right) .$$

Applying perturbation theory then leads to momentum and energy conservation:

$$\pm\boldsymbol{q}_1 \pm \boldsymbol{q}_2 \pm \boldsymbol{q}_3 = \boldsymbol{G} , \qquad \pm\omega(\boldsymbol{q}_1) \pm \omega(\boldsymbol{q}_2) \pm \omega(\boldsymbol{q}_3) = 0 . \tag{1.4}$$

For third and higher order terms $\hat{H}_{\mathrm{harm}}$ does not diagonalize any longer and three-phonon processes occur in V^3. Whereas energy and momentum are conserved, this is not the case for the particle number (see Figure 1.2).

A process found to be important for energy relaxation in graphite, presented in Section 3.4, is the annihilation of a high energy phonon by emitting two low energy phonons, i.e. $\hat{b}^\dagger_{\boldsymbol{q}_3}\hat{b}^\dagger_{\boldsymbol{q}_2}\hat{b}_{\boldsymbol{q}_1}$ as presented in Figure 1.2(a). Here, a phonon with momentum $\boldsymbol{q}_1$ and frequency ω_1 scatters into two newly created phonons with momenta $\boldsymbol{q}_2$ and $\boldsymbol{q}_3$ and frequencies ω_2 and ω_3. Scattering rates for such three-phonon processes are found to be described sufficiently by the distributions of the emitted phonon modes [Orb67, LvdLK71] with γ_0, the scattering rate for $T \to 0$:

$$\gamma_1 = \gamma_0\left[1 + b(\omega_2, T) + b(\omega_1 - \omega_2, T)\right] . \tag{1.5}$$

Concerning Equation (1.4), one distinguishes *normal processes* with $\boldsymbol{G} = 0$, and *umklapp processes* with $\boldsymbol{G} \neq 0$. Normal processes are restricted to the first BZ. Thus, umklapp processes are important for the heat conductivity, since they lead to momentum relaxation in a crystal lattice.

1.1.3 Electronic Transitions

After examining the ionic motion, we now consider the electrons. The hamiltonian of the electronic system is given by

$$\hat{H} = \underbrace{\sum_{i=1}^{N_e} \frac{\boldsymbol{p}_i^2}{2m}}_{\hat{H}_0} + \underbrace{\frac{1}{2} \sum_{i \neq j} \frac{e^2}{|\boldsymbol{r}_i - \boldsymbol{r}_j|}}_{\hat{H}_{\mathrm{e-e}}} , \tag{1.6}$$

finding a free electron part $\hat{H}_0$ and a part $\hat{H}_{\mathrm{e-e}}$ describing the electron-electron interaction. Eigenfunctions of $\hat{H}_0$ are Bloch states $\mid \boldsymbol{k}\sigma \rangle$. Since effects of spin interaction such as ferromagnetism or spin-orbit coupling are neglected, the band structure does not depend on the spin σ, and the Bloch states factorize into a spin and an orbit term: $\mid \boldsymbol{k}\sigma \rangle = \mid \boldsymbol{k} \rangle \otimes \mid \uparrow\downarrow \rangle$. Equation (1.6) can be rewritten in second quantization:

$$\hat{H} = \underbrace{\sum_{\boldsymbol{k}} E(\boldsymbol{k})\, \hat{c}_{\boldsymbol{k}}^{\dagger} \hat{c}_{\boldsymbol{k}}}_{\hat{H}_0} + \underbrace{\frac{1}{2} \sum_{\boldsymbol{k}_1 \boldsymbol{k}_2, \boldsymbol{k}_3 \boldsymbol{k}_4} u_{\boldsymbol{k}_1 \boldsymbol{k}_2, \boldsymbol{k}_3 \boldsymbol{k}_4} \hat{c}_{\boldsymbol{k}_1}^{\dagger} \hat{c}_{\boldsymbol{k}_2}^{\dagger} \hat{c}_{\boldsymbol{k}_3} \hat{c}_{\boldsymbol{k}_4}}_{\hat{H}_{\mathrm{e-e}}} .$$

Here, annihalition and creation operators $\hat{c}$, $\hat{c}^{\dagger}$ have been introduced, which fulfill the fermionic anticommutator relations [GR86, Gro05]. Information on the band structure $E_n(\boldsymbol{k})$ is needed, especially if more than one band is considered. In contrast to phonons, fermionic occupation in equilibrium is subject to the Fermi-Dirac distribution function:

$$f(E) = \frac{1}{e^{(\hbar\omega - \mu)/kT} + 1} .$$

By some perturbation $\hat{H}_{\mathrm{per}}$, an electronic transition between two states $\mid n\boldsymbol{k} \rangle \rightarrow \mid n'\boldsymbol{k}' \rangle$ can be induced, e.g. via photons, phonons or impurities. Thus, the photon energy $\hbar\omega$ has to match the difference in energy between initial and final states. The probability for such events is given by Fermi's golden rule:

$$\mathcal{W}\left(n\boldsymbol{k} \rightarrow n'\boldsymbol{k}'\right) = \frac{1}{2} \mid \langle n\boldsymbol{k} \mid \hat{H}_{\mathrm{per}} \mid n'\boldsymbol{k} \rangle \mid^2 \delta\left(E_{n'} - E_n + \hbar\omega\right) .$$

Here, the simplest case may be the annihilation of an electron in the valence band in state $\mid n\boldsymbol{k} \rangle$ and the parallel creation of an electron in the conduction band in state $\mid n'\boldsymbol{k}' \rangle$. It turns out to be sufficient to describe this excited state by an electron in the conduction band and a hole in the valence band [Fre31]. Here, $\boldsymbol{k}' = \boldsymbol{k} + \boldsymbol{k}_{\hbar\omega}$ accounts for the momentum of the photon with $\boldsymbol{k} \approx 0$.

Electronic Density of States

In most cases we do not need the full information on $E_n(\boldsymbol{k})$ for electrons. Thus, we define the electronic density of states (eDOS):

$$D(E) = \frac{2}{N} \sum_{n\boldsymbol{k}} \delta\left(E - E_n(\boldsymbol{k})\right) . \tag{1.7}$$

Here, the factor 2 accounts for the spin degeneracy. $D(E)$ provides information on the existence of electronic states in a given energy range $\Delta E = E - E_n(\boldsymbol{k})$. Consequently, the Fermi energy E_F at $T = 0$ is given by:

$$\int_{-\infty}^{E_F} \mathrm{d}E\, D(E) = Z_e .$$

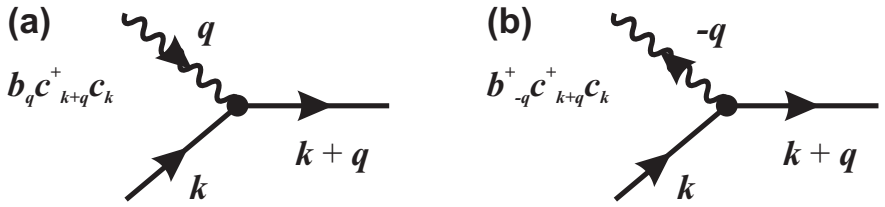

Figure 1.3: *Vortex diagram of electron-phonon processes: (a) Absorption of a phonon with momentum $\boldsymbol{q}$, (b) emission of a phonon with momentum $-\boldsymbol{q}$.*

1.1.4 Electron-Phonon Interaction

So far, electronic and phononic degrees of freedom have been considered to be decoupled. This simple picture will be corrected in the lowest non-vanishing order [Czy04]. To do this, assume the ionic vector as a sum of lattice vector and the displacement of the l^{th} ion to be $\boldsymbol{R}_l = \boldsymbol{R}_{l0} + \boldsymbol{u}_l$. Expansion into a series leads to:

$$\nu\left(\boldsymbol{r} - \boldsymbol{R}_l\right) = \nu\left(\boldsymbol{r} - \boldsymbol{R}_{l0}\right) - \nabla\nu\left(\boldsymbol{r}_i - \boldsymbol{R}_{l0}\right)\boldsymbol{u}_l \ .$$

Thus, the hamiltonian becomes:

$$\hat{H}_0 = \sum_{i=1}^{N_e} [\ \underbrace{\frac{\boldsymbol{p}_i^2}{2m}}_{T} + \underbrace{\sum_{n=1}^{N} \nu\left(\boldsymbol{r} - \boldsymbol{R}_{n0}\right)}_{V_{\text{per}}(\boldsymbol{r}_i)} - \underbrace{\sum_{n=1}^{N} \nabla\nu\left(\boldsymbol{r}_i - \boldsymbol{R}_{n0}\right)\boldsymbol{u}_n}_{V_{\text{e-ph}}(\boldsymbol{r}_i)}\ ] \ .$$

Here, the term V_{per} diagonalizes in second quantization together with the kinetic part T, whereas $V_{\text{e-ph}}$ does not diagonalize. Now, consider the one-particle hamiltonian

$$\hat{H}_0 = \sum_{\boldsymbol{k}} E\left(\boldsymbol{k}\right) \hat{c}^\dagger_{\boldsymbol{k}} \hat{c}_{\boldsymbol{k}} - \sum_{\boldsymbol{k}\boldsymbol{k}'} M_{\boldsymbol{k}\boldsymbol{k}'} \hat{c}^\dagger_{\boldsymbol{k}'} \hat{c}_{\boldsymbol{k}} \ ,$$

with matrix element $M_{\boldsymbol{k}\boldsymbol{k}'} = \langle\ \boldsymbol{k}\ |\ V_{\text{e-ph}}\ |\ \boldsymbol{k}'\ \rangle$. Further proceeding, especially using creation and annihilation operators, leads to the so-called Fröhlich model for the EPC [Czy04]:

$$\hat{H}_0 = \sum_{\boldsymbol{k}} E\left(\boldsymbol{k}\right) \hat{c}^\dagger_{\boldsymbol{k}} \hat{c}_{\boldsymbol{k}} + \sum_{\boldsymbol{k}\boldsymbol{q}\boldsymbol{G}j} M^j_{\boldsymbol{k},\boldsymbol{q}+\boldsymbol{G}} \left(\hat{b}_{\boldsymbol{q}j} + \hat{b}^\dagger_{-\boldsymbol{q}j}\right) \hat{c}^\dagger_{\boldsymbol{k}+\boldsymbol{q}+\boldsymbol{G}} \hat{c}_{\boldsymbol{k}} \ . \tag{1.8}$$

The first term describes the interaction of the electrons, while the second term represents the EPC, as can be seen from mixed terms in $\hat{b}$ and $\hat{c}$. The matrix element of the interaction is given by

$$M^j_{\boldsymbol{k},\boldsymbol{q}+\boldsymbol{G}} = -\mathrm{i}\sqrt{\frac{\hbar N}{2M\omega_j\left(\boldsymbol{q}\right)}}\left(\boldsymbol{q}+\boldsymbol{G}\right)\cdot\boldsymbol{e}_j\left(\boldsymbol{q}\right)\frac{\nu_{\boldsymbol{q}+\boldsymbol{G}}}{V_{\text{uc}}}\int_{\text{uc}} \mathrm{d}^3 r\ u^*_{\boldsymbol{k}+\boldsymbol{q}+\boldsymbol{G}}\left(\boldsymbol{r}\right) u_{\boldsymbol{k}}\left(\boldsymbol{k}\right) \ . \tag{1.9}$$

Integration runs over the unit cell with volume V_{uc}. To emphazise a picture: the lattice displacements lead to electronic transitions or electron scattering $\boldsymbol{k} \to \boldsymbol{k}' = \boldsymbol{k} + \boldsymbol{q}$ by absorption of a phonon with momentum $\boldsymbol{q}$ or emission of a phonon with momentum $-\boldsymbol{q}$.

Usually, the processes are shown in *vortex diagrams*, as presented in Figure 1.3. Here, momentum conservation takes place at the vortex, since the computation of the electronic matrix elements leads to δ-functions [Czy04]. This picture is restricted to the first BZ, otherwise a reciprocal lattice vector $\boldsymbol{G}$ has to be introduced:

$$\boldsymbol{k} \to \boldsymbol{k}' = \boldsymbol{k} + \boldsymbol{q} + \boldsymbol{G} \ .$$

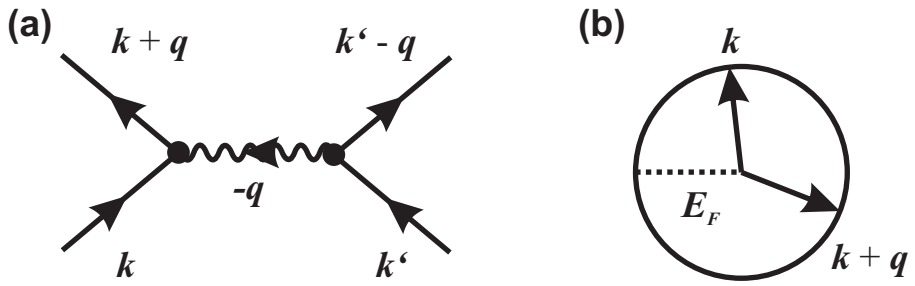

Figure 1.4: *(a) Vortex diagram of a cooper pair consisting of two electrons with momenta $\boldsymbol{k}$ and $\boldsymbol{k}'$ mediated by a phonon with momentum $-\boldsymbol{q}$. (b) Fermi surface with radius E_F together with momenta $\boldsymbol{k}$ and $\boldsymbol{k}+\boldsymbol{q}$. If both match the Fermi surface, the Fröhlich interaction is attractive.*

Again, normal and umklapp processes occur as introduced in Section 1.1.2. In terms of Equation (1.9) only longitudinal phonon modes couple to electrons. Otherwise the matrix element $M^j_{\boldsymbol{k},\boldsymbol{q}+\boldsymbol{G}}$ vanishes because of $\boldsymbol{q}\cdot\boldsymbol{e}_j = 0$.

The discussed derivation of $\hat{H}_0$ is correct, provided that three conditions are met:

1. the expansion just included first order terms,
2. since phonons usually do not cause interband transitions, a one-band model was used, and
3. one atom per unit cell has been considered.

The most important restriction is number 3. Including more than one atom per unit cell would lead to additional coupling to electrons, and thus optical phonon modes (see Section 1.1.2).

1.1.5 Cooper Pairing

The previous section has introduced the interaction of electrons and phonons. Now, consider two electrons interacting via an effective potential V^{eff}. If V^{eff} is attractive, both electrons are described altogether forming a so-called Cooper pair. This bound state has been postulated by Leon Cooper [Coo56, Coo72] and points toward the BCS theory for superconductors [BCS57, Bar72, Sch72]. Effective attractive electron-electron interaction [Frö50, Frö52] is mediated by a phonon in the BCS case. Here, the Fröhlich model applies. An intuitive picture is provided in Figure 1.5. An electron with momentum $\boldsymbol{k}$ induces a polarization of the lattice that attracts a second electron with momentum $\boldsymbol{k}'$. The attractive electron-electron interaction is retarded since the first electron has already left due to the different time scales applying for electronic and ionic motion (see Section 1.1.1 and [Czy04]). For this reason, the Coulomb interaction plays a minor role. In fact, the coherence length of a Cooper pair bound by phonons is found to be $\xi = 100 - 1000$ nm. Since Cooper pairing has more general features and does not only occur phonon-mediated, its main idea shall be discussed here, as well as the excitation scheme of Cooper pairs. The type of interaction V^{eff} itself will be discussed in Section 4.1.2.

Consider the second term of Equation (1.8) with coupling to only one longitudinal phonon branch and neglect umklapp processes. For the perturbed system, the energy is given by $W_k = E_k + (\delta E_k)^{(1)} + (\delta E_k)^{(2)}$. Here, perturbation theory yields:

$$
\begin{aligned}
(\delta E_k)^{(1)} &= \langle\phi_k|\,\hat{H}_{e-ph}\,|\phi_k\rangle = 0\,; \\
(\delta E_k)^{(2)} &= \sum_{\mu\neq(1_k,0_{ph})} \frac{\langle\phi_k|\,\hat{H}_{e-ph}\,|\mu\rangle\,\langle\mu|\,H_{e-ph}\,|\phi_k\rangle}{E_k - W_\mu} = \sum_q \frac{|V_q|^2}{E_k - (E_{k+q} + \omega_{-q})}\,.
\end{aligned}
$$

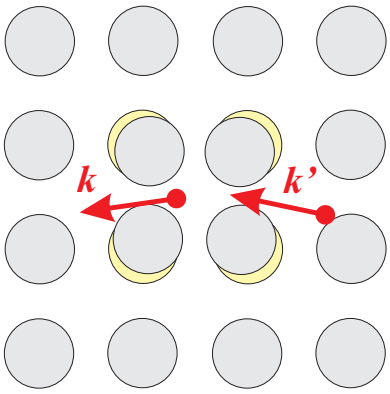

Figure 1.5: *Interpretation of a Cooper pair: Schematic of the polarization of the ion lattice induced by an electron. The first electron with momentum $\boldsymbol{k}$ induces a polarization of the lattice. Then, a second electron with momentum $\boldsymbol{k}'$ feels an attractive potential caused by the induced polarization.*

While the first order vanishes, the second order describes the interaction of the electron gas with the phonons.

The insight of Cooper was to consider the initial state consisting of two electrons with $\boldsymbol{k}$, $\boldsymbol{k}'$ as well as attractive interaction. This pair is put into a system of non-interacting electrons, filled to E_F. They scatter into states with $\boldsymbol{k}+\boldsymbol{q}$ and $\boldsymbol{k}'-\boldsymbol{q}$, while the total momentum is conserved as $\boldsymbol{K}=\boldsymbol{k}+\boldsymbol{k}'$. This is shown in Figure 1.4(a). From $(\delta E_k)^{(2)}$, the so-called Fröhlich interaction can be calculated:

$$V^{\text{eff}}(k,q)=\frac{2\left|V_q\right|^2\omega_q}{\left(E(k)-E(k+q)\right)^2-\omega_q^2}\,.$$

An attractive potential is achieved if $E(k)=E(k+q)$, as shown in Figure 1.4(b):

$$V^{\text{eff}}=\frac{-2\left|V_q\right|^2}{\omega_q}\,.$$

The resulting non-interacting Cooper pair is given by the product:

$$\phi\left(\boldsymbol{r}_1,\boldsymbol{r}_2\right)=\left(e^{i\boldsymbol{k}_1\cdot\boldsymbol{r}_1}\chi_\uparrow\right)\left(e^{i\boldsymbol{k}_2\cdot\boldsymbol{r}_2}\chi_\downarrow\right)$$

where the single particle wavefunction is a product of position and spin. A spin singlet and the pair at rest with $\boldsymbol{k}_1=-\boldsymbol{k}_2$ is favored. This then leads to

$$\phi\left(\boldsymbol{r}_1,\boldsymbol{r}_2\right)=e^{i\boldsymbol{k}\cdot(\boldsymbol{r}_1-\boldsymbol{r}_2)}\chi_\uparrow^{(1)}\chi_\downarrow^{(2)}\,.$$

Considering a pair with Fröhlich interaction in combination with the Pauli principle ($|\boldsymbol{k}'|\,,|\boldsymbol{k}|>k_F$) and $E_k-E_{k'}<\hbar\omega_q\approx\hbar\omega_D$, the interaction becomes attractive

$$\left\langle\boldsymbol{k}\left|V^{\text{eff}}\right|\boldsymbol{k}'\right\rangle=\begin{cases}-W_0: & E_k-E_{k'}\leq\hbar\omega_D \text{ and } \left|\boldsymbol{k}'\right|,|\boldsymbol{k}|>k_F\\ 0: & \text{otherwise}\end{cases}$$

and the Fermi energy is reduced by [Gro06, Czy04]:

$$\Delta=2\hbar\omega_D e^{-\frac{2}{W_0 D(\epsilon_F)}} \tag{1.10}$$

Since pairs are bound, it takes a certain amount of energy to break them up, leading to what is known as the superconducting gap. In a superconductor, nothing happens until one supplies an amount of energy equal to the binding energy, and once one bridges that gap, energy can be absorbed. In this so-called order parameter Δ, the Debye frequency ω_D occurs. Since the coupling constant W_0 shows a non-analytic dependency, no perturbation theory can be applied.

So the problem of the superconducting particles is solved by reducing the number of interacting electrons to just two and treating all the other electrons as fixed in place in the Fermi sea. Then it is possible to show that an arbitrarily small attraction between these two electrons makes pairing up together cost less energy than single floating. Cooper pairs thus are stable entities. Cooper showed that pairing will inevitably occur as long as there is a weak interaction [Coo72]. This does not need to be neccessarily a phonon mediated interaction.

To summarize, Cooper pairs show four fundamental properties, that will be exploited in Chapters 4 and 5. Cooper pairs have

1. a small binding energy with exponential development (Equation (1.10)),
2. a critical temperature T_c below which they exist,
3. a large coherence length,
4. a Bose distribution due to integer spin.

The concept of electron pairing then leads to a description of the superconducting state. Cooper pairs additionally have to condensate into a coherent state with fixed phase. So all pairs are locked together, leading to a state that is not affected by scattering events because pair states scatter into pair states. Since it would cost a lot of energy to break up Cooper pairs, they remain locked and are able to sustain a current without Ohmic losses.

1.2 Light-Matter Interaction: Dielectric Function

Light-matter interaction reveals information on the fundamental excitations in solids. The basic concept of all optical experiments is as follows: an incoming electromagnetic wave with electric field $\boldsymbol{E}$ modifies the distribution of the charge carriers in matter and induces a polarization $\boldsymbol{P}$. This polarization is a source of new electromagnetic radiation that can be measured as scattered light. The scattered light reveals information on the optical properties of a sample via the complex dielectric function $\varepsilon(\omega) = \varepsilon_1(\omega) + \mathrm{i}\varepsilon_2(\omega)$. In general, all excitations show a fingerprint in $\varepsilon(\omega) = 1 + 4\pi\chi(\omega)$. This connects the induced polarization $\boldsymbol{P}$ to the total electric field $\boldsymbol{E}$ by

$$\boldsymbol{P} = \chi \boldsymbol{E} \,. \tag{1.11}$$

Starting with a macroscopic interpretation, the quantum-mechanical description will be introduced. Here, the microscopic model

$$\hat{H} = \hat{H}_0 + \hat{H}_{e-em} + \hat{H}_{e-x} \tag{1.12}$$

includes several scattering terms accounting for the interaction of light and electrons ($e - em$) as well as other sources for electron scattering ($e - x$).

1.2.1 Macroscopic Interpretation

Here, the imaginary part ε_2 of the dielectric function represents the absorption, the real part ε_1 a phase shift between the induced polarization $\boldsymbol{P}$ and the driving electric field $\boldsymbol{E}$. Real and imaginary parts are usually linked by Kramers-Kronig relations [Gre02], assuming the knowledge of one part's full frequency range. As will be seen in Section 1.3.3, electro-optic sampling allows to measure both the real and imaginary part of $\varepsilon(\omega)$. Therefore, Kramers-Kronig relations are not applied.

The macroscopic response of a sample can be linked to microscopic processes inside the sample by using appropriate models. It turns out that both classical models and quantum-mechanical description lead to an adequate description of different aspects of the samples response.

Lorentz Oscillator

First, consider a dielectric medium as a sum of harmonic oscillators with electron displacement $\boldsymbol{x}$ to the ion cores $\boldsymbol{X}$ via an oscillating electric field $\boldsymbol{E}$. Every electron then is forced to oscillate, damped by dipole emission. For small amplitudes the equation of motion holds [KH07]:

$$\ddot{\boldsymbol{x}} + \gamma\dot{\boldsymbol{x}} + \omega_0^2\boldsymbol{x} = -\frac{e}{m}\boldsymbol{E}(\boldsymbol{X},\omega) \; .$$

Here, γ is a damping constant to the undamped frequency ω_0 . The stationary solution after a relaxation time given by $\tau = \gamma^{-1}$ then is [KH07]:

$$\boldsymbol{x}(\omega) = -\frac{e}{m}\frac{\boldsymbol{E}(\boldsymbol{X},\omega)}{\omega_0^2 - \omega^2 - \mathrm{i}\gamma\omega} \; .$$

The caused dipole moment $\boldsymbol{p} = -e\boldsymbol{x}$ leads to a polarization of all N dipoles in a given volume V around $\boldsymbol{X}$:

$$\boldsymbol{P}(\boldsymbol{X},\omega) = -\frac{N}{V}e\boldsymbol{x}(\omega) \; .$$

Using Equation (1.11) then leads to the dielectric function [KH07]:

$$\varepsilon(\omega) = 1 + \frac{\omega_{\mathrm{pl}}^2}{\omega_0^2 - \omega^2 - \mathrm{i}\gamma\omega} \; , \tag{1.13}$$

introducing the plasma frequency $\omega_{pl} = \sqrt{Ne^2/Vm}$, i.e. the resonance frequency of the system.

Drude Model

Without restoring force ($\omega_0 = 0$), we find the solution for a free electron gas:

$$\varepsilon(\omega) = 1 - \frac{\omega_{\mathrm{pl}}^2}{\omega^2 + \mathrm{i}\gamma\omega} \; . \tag{1.14}$$

This generalization of Ohm's law is called the Drude response [Dru04a, Dru04b] and suitable also from a quantum-mechanical point of view. Here, the basic concept considers an electron gas which drifts in the direction of an applied voltage and assumes that the motion of an electron is not damped by collision with other electrons.

1.2.2 Microscopic Models

From Equation (1.12), light-electron interaction to the first order in the Coulomb gauge is given by [Czy04]

$$\hat{H}_{e-em} = -\frac{1}{c}\int \mathrm{d}^3x \; \hat{j}(\boldsymbol{x})\hat{A}(\boldsymbol{x},t) \; .$$

Here, the current density operator

$$\hat{j}(\boldsymbol{x}) = -\frac{e}{2m}\sum_i [\hat{\pi}_i\delta(\boldsymbol{x} - \hat{x}_i) + \delta(\boldsymbol{x} - \hat{x}_i)\hat{\pi}_i]$$

with positions $\hat{x}_i$ and canonical momenta $\hat{\pi}_i$ for all electrons i occur. First order perturbation theory leads to the tensor of the dielectric function, the so-called *Kubo formula* [Czy04]:

$$\varepsilon_{\alpha\beta}(\omega) = -\frac{4\pi N_e e^2}{m\omega^2} + \frac{4\pi}{V\omega^2}\sum_{nn',\boldsymbol{k}\boldsymbol{k}'}\frac{\langle n'\boldsymbol{k}'|\,\hat{j}_\alpha\,|n\boldsymbol{k}\rangle\,\langle n\boldsymbol{k}|\,\hat{j}_\beta\,|n'\boldsymbol{k}'\rangle}{E_{n'\boldsymbol{k}'} - E_{n\boldsymbol{k}} - \hbar\omega - \mathrm{i}0^+}(\rho_{n\boldsymbol{k},n\boldsymbol{k}} - \rho_{n'\boldsymbol{k}',n'\boldsymbol{k}'}) \; . \tag{1.15}$$

We have to sum over all initial and final states of the unperturbed system, $|n\boldsymbol{k}\rangle$ and $|n'\boldsymbol{k}'\rangle$ respectively. An incoming photon is absorbed if its energy $\hbar\omega$ matches the difference of the eigenenergies $E_{n'\boldsymbol{k}'}$ and $E_{n\boldsymbol{k}}$ and if the initial population exceeds the final population. The infinitesimally small positive number 0^+ has been introduced to ensure that the perturbing electric field vanishes in the past. Note that off-diagonal elements of the density matrix ρ have been ignored and that the Kubo formula is not applicable for fast changes.

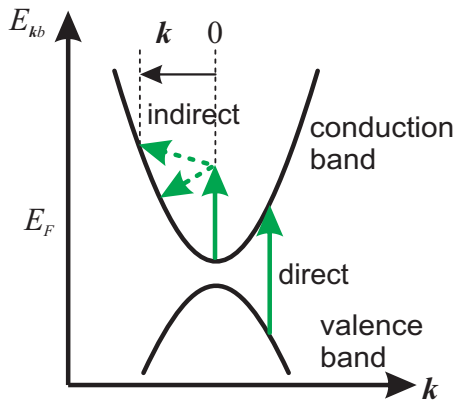

Figure 1.6: *Schematic bandstructure around E_F. A direct optical transition between two bands (interDOT) leaves the momentum of the electron virtually unchanged $\boldsymbol{\Delta k} = 0$, while an indirect optical transition leads to a change $\boldsymbol{\Delta k} \neq 0$.*

1.2.3 Optical Transitions in Crystalline Solids

Now, the Kubo formalism is applied to Bloch electrons in a crystalline solid. The absorption of a photon is possible via transitions between eigenstates of the unperturbed system

$$| n\boldsymbol{k} \rangle \xrightarrow{\hbar\omega} | n'\boldsymbol{k}' \rangle \ . \tag{1.16}$$

Using pertubation theory, the hamiltonian $\hat{H} = \hat{H}_0 + \hat{H}_{e-em}$ with the unperturbed Bloch electrons $\hat{H}_0$ results in an expression for the dielectric function which can be separated in interband ($n \neq n'$) and nonresonant intraband ($n = n'$) DOTs:

$$\varepsilon^{\mathrm{DOT}} = \varepsilon^{\mathrm{interDOT}} + \varepsilon^{\mathrm{intraDOT}} \ .$$

After the additional inclusion of indirect optical transitions, IOTs, three different processes of optical transitions can be distinguished:

interDOTs ($\boldsymbol{\Delta k} = 0$, $n \neq n'$): The electronic wavevector remains nearly unchanged since the wavevector of the light field is much smaller than the dimensions of the BZ. For an interband transition, the initial and final state $| n\boldsymbol{k} \rangle$ and $| n'\boldsymbol{k} \rangle$ are in different bands n and n', respectively.

intraDOTs ($\boldsymbol{\Delta k} = 0$, $n = n'$): The electronic wavevector remains nearly unchanged since the wavevector of the light field is much smaller than the dimensions of the BZ. For an intraband transition initial and final states are identical, i.e. they are in the same band.

IOTs ($\boldsymbol{\Delta k} \neq 0$): A higher order process involves further interaction by lattice imperfections additional to light-electron interaction. Since the electronic wavevector changes, these transitions are called an indirect optical transition.

Below, DOTs and IOTs will be explained in more detail and compared to the classical Drude model. For this, the Drude formula (1.14) is linearized in Γ:

$$\varepsilon^{\mathrm{Drude}} = 1 - \frac{\omega_{\mathrm{pl}}^2}{\omega^2} + \mathrm{i}\frac{\omega_{\mathrm{pl}}^2}{\omega^3}\Gamma \ . \tag{1.17}$$

Direct Intraband Transitions

If the occupation number only depends on the electron energy $f_k = f(E_k)$, the direct intraband part is given by [Ped03]

$$\begin{aligned} \varepsilon^{\mathrm{intraDOT}}(\omega) &= 1 + \frac{1}{\omega^2}\frac{8\pi e^2}{V}\sum_{n\boldsymbol{k}} \left.\frac{\partial f}{\partial E}\right|_{n\boldsymbol{k}} \cdot \boldsymbol{v}_{n\boldsymbol{k}} \cdot {}^t\boldsymbol{v}_{n\boldsymbol{k}} \\ &= 1 - \frac{\omega_{\mathrm{pl}}^2}{\omega^2} \ , \end{aligned} \tag{1.18}$$

defining the squared plasma frequency

$$\omega_{\mathrm{pl}}^2 = -\frac{8\pi e^2}{V} \sum_{n\boldsymbol{k}} \left.\frac{\partial f}{\partial E}\right|_{n\boldsymbol{k}} \cdot \boldsymbol{v}_{n\boldsymbol{k}} \cdot {}^t\boldsymbol{v}_{n\boldsymbol{k}} \ . \tag{1.19}$$

Here, f is the occupation number of the Bloch state $\mid n\boldsymbol{k} \rangle$ and $\boldsymbol{v}_{n\boldsymbol{k}} = (1/\hbar)\partial_{\boldsymbol{k}} E_{n\boldsymbol{k}}$ the band velocity. Considering the Fermi-Dirac distribution, only electrons around E_{F} contribute. Since the transition energy of an intraDOT vanishes, its contribution to the optical response is called *free-carrier response*. It becomes appreciable for a large eDOS and large band velocities around E_{F}, where $\partial f/\partial E \neq 0$. The intraDOTs are non-resonant and affect only the real part of the dielectric function ε. A reformulation of Equation (1.19) then leads to a generalized free-carrier plasma frequency [All71]:

$$\omega_{\mathrm{pl}}^2 = -\frac{8\pi e^2}{V} \int \mathrm{d}\epsilon \frac{\partial f}{\partial E} v^2 D(\epsilon) \ . \tag{1.20}$$

Here, the velocity-weighted eDOS has been used,

$$v^2 D(E) = \sum_k \boldsymbol{v}_k {}^t\boldsymbol{v}_k \delta\left(E - E\left(\boldsymbol{k}\right)\right) , \tag{1.21}$$

showing roughly the same spectral structure as $D(E)$ [All71] and introducing the group velocity for the n^{th} band:

$$\boldsymbol{v}_{n\boldsymbol{k}} = \frac{1}{\hbar} \boldsymbol{\nabla}_{\boldsymbol{k}} E_n\left(\boldsymbol{k}\right) \ . \tag{1.22}$$

Direct Interband Transitions

The direct interband part has to account for optical transitions

$$\mid n\boldsymbol{k} \rangle \xrightarrow{\hbar\omega} \mid n'\boldsymbol{k} \rangle$$

with resonances due to a photon energy $\hbar\omega$. As presented earlier, the linear response formalism provided by the Kubo formula is suitable for this purpose [Ped03]:

$$\varepsilon_{ii}^{\mathrm{interDOT}} = \frac{4\pi e^2 \hbar^2}{V m^2} \sum_{nn'\boldsymbol{k}} \frac{\left|\langle\, n\boldsymbol{k} \left|p_i\right| n'\boldsymbol{k} \,\rangle\right|^2 \left(f_{n'\boldsymbol{k}} - f_{n\boldsymbol{k}}\right)}{(E_{n'\boldsymbol{k}} - E_{n\boldsymbol{k}})^2 (E_{n'\boldsymbol{k}} - E_{n\boldsymbol{k}} - \hbar\omega - \mathrm{i}0^+)} \ . \tag{1.23}$$

Indirect Optical Transitions

The interaction part $\hat{H}_{e-x}$ in Equation (1.12) contains the IOTs. Perturbation theory to second order yields [DG02]

$$\varepsilon^{\mathrm{IOT}}(\omega) = \mathrm{i}\frac{\omega_{\mathrm{pl}}^2}{\omega^3}\Gamma \ .$$

Additionally taking impurity scattering and interaction with phonons into account, contributing only to the imaginary part of ε, the IOT part becomes:

$$\mathrm{Im}\, \varepsilon_{\alpha\alpha}^{\mathrm{IOT}} = \frac{2(2\pi\hbar e)^2}{(\hbar\omega)^4 V} \sum_{kk'} w_{kk'\omega} \left(v_{k\alpha} - v_{k'\alpha}\right)^2 f_k \left(1 - f_{k'}\right) , \tag{1.24}$$

with two parts of the electronic transition rate, $w_{kk'\omega}^{\mathrm{e-imp}}$ and $w_{kk'\omega}^{\mathrm{e-ph}}$, due to electron-impurity-photon coupling and electron-phonon-photon coupling, given by

$$\begin{aligned} w_{kk'\omega}^{\mathrm{e-imp}} &= \left|V_{k'k}^{\mathrm{imp}}\right|^2 \left[\delta\left(\Delta E - \hbar\omega\right) - \left(\Delta E + \hbar\omega\right)\right] , \\ w_{kk'\omega}^{\mathrm{e-ph}} &= \sum_{r\pm} \left|M_{k'k}^r\right|^2 \left(b_{q^\pm} + \frac{1}{2} \pm \frac{1}{2}\right) \left[\delta\left(\Delta E \pm \hbar\omega_{q^\pm} - \hbar\omega\right) - \left(\Delta E + \pm\hbar\omega_{q^\pm}\hbar\omega\right)\right] , \end{aligned}$$

defining the difference of the energies of initial and final state $\Delta E = E_{k'} - E_k$. In this formalism, the lattice impurities scatter more with electrons the more electrons are in the initial and the less in the final state. However, as suggested by Equation (1.24), absorption of light that is polarized along the α direction only occurs if the electrons change their band velocity $v_{k\alpha}$ along the same direction $\alpha \in \{x, y, z\}$.

According to the linearized Drude model from Equation (1.17), which represents a combination of $\varepsilon^{\mathrm{IOT}}$ and $\varepsilon^{\mathrm{intraDOT}}$ in case of $\Gamma \ll \omega$, a generalized Drude scattering rate can be motivated [All71]

$$\Gamma(\omega) = \frac{\omega^3}{\omega_{\mathrm{pl}\alpha\alpha}^2} \mathrm{Im}\, \varepsilon_{\alpha\alpha}^{\mathrm{IOT}} \,. \tag{1.25}$$

Assuming a constant band velocity $v_{k\alpha}^2 = v_{\mathrm{F}}^2/3$, matrix elements $\mid V_{k'k}^{\mathrm{imp}} \mid^2 = \mid V_{\mathrm{F}}^{\mathrm{imp}} \mid^2$ for impurity scattering and eDOS $D(E_{\mathrm{F}})$ around the Fermi energy yield an estimate

$$\Gamma^{\mathrm{imp}} \propto \frac{\pi}{\hbar} \left| V_{\mathrm{F}}^{\mathrm{imp}} \right|^2 D(E_{\mathrm{F}}) \tag{1.26}$$

for the Drude scattering rate, where the constant values can be understood as averages over the Fermi surface. A large eDOS implies many initial and final states for the scattering of electrons and therefore leads to a large velocity-relaxation rate. In general, the Drude scattering rate Γ depends on the temperature T_a and the light frequency ω according to Equation (1.25), which is especially relevant for a strongly varying eDOS around E_{F} as found in the case of graphite and for electron-phonon scattering.

Summary

The analysis has shown the real part $\mathrm{Re}\ \varepsilon^{\mathrm{Drude}}$ to be linked to direct intraband transitions (intraDOTs) and the imaginary part $\mathrm{Im}\ \varepsilon^{\mathrm{Drude}}$ to be associated with IOTs:

$$\varepsilon^{\mathrm{Drude}} = \mathrm{Re}\ \varepsilon^{\mathrm{intraDOT}} + \mathrm{i}\ \mathrm{Im}\ \varepsilon^{\mathrm{IOT}} \,.$$

Altogether, direct and indirect transitions contribute as follows:

$$\varepsilon = \varepsilon^{\mathrm{interDOT}} + \underbrace{\varepsilon^{\mathrm{intraDOT}} + \varepsilon^{\mathrm{IOT}}}_{\varepsilon^{\mathrm{Drude}}} \,.$$

1.3 Terahertz Spectroscopy

All results presented here are based on experiments using ultrashort laser pulses and resulting effects from their non-linear interaction with matter. The low-energy regime is of special interest, since sources for short THz pulses have not been available until the development of femtosecond lasers [BTS02], but various fundamental excitations in solids are found in that energy range. In recent years, the so-called 'THz-gap' has been filled by two different techniques: photo-mixing in nanostructured antennas and difference frequency generation (DFG) in non-linear crystals. THz radiation is in the far IR and MIR, 1 THz corresponds to an energy of 4.1 meV. As a consequence, low THz intensities are completely overwhelmed by the black body radiation of the surroundings. In the experimental setup used, femtosecond laser pulses generate THz pulses in the range from 1 to 5 THz and 10 to 40 THz using DFG. Here, the spectral range depends on the generating non-linear medium. Using laser pulses also allows time-resolved detection. Electro-optic sampling then enables us to measure the complete THz waveform, leading to the sample response given by the dielectric function $\varepsilon(\omega)$.The THz range has been found to be well suited to investigate the electronic properties of materials, since it is sensitive to electronic excitations around E_F.

This section presents the theoretical framework of THz generation and detection in brief, as previously done in [Sch05, Nöt07]. Subsequently, Section 2.1 provides an overview to the experimental details. Since the non-linear effects are important, first a short dicussion will point out the differences between linear and non-linear optics [vV04].

1.3.1 Nonlinear Optics

Applied high electric fields, as they can be found in ultrashort laser pulses, lead to non-linear effects in matter. Since these pulses show a broad spectral range, dispersive effects also occur. Starting with Maxwell's equations, the wave equation for a macroscopic electric field $\boldsymbol{E}(\boldsymbol{x}, t)$ in cgs units is [Gre02]:

$$\left(\boldsymbol{\Delta} + \frac{1}{c^2}\frac{\partial^2}{\partial t^2}\right)\boldsymbol{E} = -\frac{4\pi}{c^2}\frac{\partial^2}{\partial t^2}\boldsymbol{P} \,. \tag{1.27}$$

The electric field induces a polarization $\boldsymbol{P}(\boldsymbol{E})$. Since vacuum is not polarizable, $\boldsymbol{P} = 0$. If the internal fields in matter are much larger compared to the applied external field, as is still valid for ultrashort laser pulses, the polarization can be expanded into a series in $\boldsymbol{E}$:

$$\boldsymbol{P} = \boldsymbol{P}^{(0)} + \boldsymbol{P}^{(1)} + \boldsymbol{P}^{(2)} + \mathcal{O}^3 \,.$$

Equation (1.27) then becomes a non-linear partial differential equation. Following this, a Fourier transform to the frequency domain has been performed under certain conditions:

1. the medium shows a local response, so just $\boldsymbol{E}(\boldsymbol{x}_0)$ contributes to $\boldsymbol{P}(\boldsymbol{x}_0)$;
2. the medium is homogeneous in the time domain, i.e. there is no particular point in time;
3. $\boldsymbol{P}^{(0)} = 0$, no polarization without external fields.

Linear Optics

For the linear response of matter, the polarization is proportional to the applied external field. The proportionality constant is the linear dielectric susceptibility $\bar{\bar{\chi}}^{(1)}$; a second rank tensor. It follows a linear relation for the polarization:

$$\boldsymbol{P}^{(1)}(\omega) = \bar{\bar{\chi}}^{(1)}(\omega) \cdot \boldsymbol{E}(\omega) \,. \tag{1.28}$$

Here, the dielectric function $\bar{\bar{\varepsilon}} = 1 + 4\pi\bar{\bar{\chi}}^{(1)}$ and the refractive index $N = \sqrt{\varepsilon}$ are often used. Equation (1.27) then becomes a linear homogeneous differential equation, describing the linear optics:

$$\left(\boldsymbol{\Delta} - \frac{\omega^2}{c^2}\bar{\bar{\varepsilon}}\right)\boldsymbol{E} = 0 \,.$$

Dependent on the experimental geometry, the dielectric tensor $\bar{\bar{\varepsilon}}$ becomes a scalar ε.

Second Order Nonlinear Optics

For larger external fields it is necessary to also take non-linear terms of the polarization series into account. First, the second order correction will be introduced, fully describing the THz generation process. Subsequently, third order terms are presented, necessary for an understanding of the femtosecond laser pulse generation.

An example shows the second order term of the polarizations $\boldsymbol{P}^{(2)}(t)$. For practical reasons, due to the broadband laser pulses, we consider two incoming electromagnetic waves $E_j(t) = \frac{1}{2}(E_j e^{-\mathrm{i}\omega_j t} + E_j^* e^{\mathrm{i}\omega_j t})$. Scalar fields are assumed. Then, the polarization is:

$$P^2(t) = \frac{1}{4}\chi^{(2)}(E_1(t) + E_2(t))^2 \,.$$

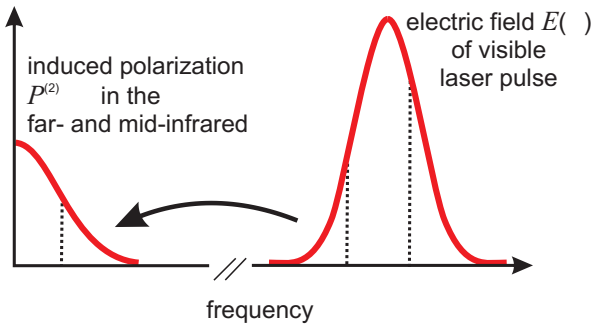

Figure 1.7: *Schematic of difference frequency generation (DFG). Two frequencies ω_1 and ω_2 in the visible light lead to a difference frequency $\Omega = \omega_1 - \omega_2$ in the far- or mid-IR.*

Applying $E_j(t)$ yields:

$$P^{(2)}(t) = \frac{1}{2}\chi^{(2)}[\underbrace{E_1^2 e^{-2i\omega_1 t}}_{SHG} + \underbrace{E_2^2 e^{-2i\omega_2 t}}_{SHG} + \underbrace{2E_1 E_2 e^{-i(\omega_1+\omega_2)t}}_{SFG} + \underbrace{2E_1 E_2^* e^{-i(\omega_1-\omega_2)t}}_{DFG} + \underbrace{E_1 E_1^* + E_2 E_2^*}_{OR}] \,.$$

Here, each term describes a special non-linear effect:

Second Harmonic Generation (SHG): the outgoing wave has twice the frequency of the incident wave but the same propagation direction.

Sum Frequency Generation (SFG): a sum frequency $\omega = \omega_1 + \omega_2$ is generated.

Difference Frequency Generation (DFG): a difference frequency $\Omega = \omega_1 - \omega_2$ is generated.

Optical Rectification (OR): a static electric field is generated.

Thus, in non-linear media and for high external fields it becomes possible to generate second harmonics, sum and difference frequencies. This is now applied to the generation of frequencies in the THz range. Here, the broad spectrum of the near-infrared femtosecond laser pulses allows THz generation via DFG as seen in Figure 1.7. The second order polarization then leads to the Fourier transformed wave equation:

$$\left(\boldsymbol{\Delta} - \frac{\omega^2}{c^2}\bar{\bar{\varepsilon}}\right)\boldsymbol{E} = -\frac{4\pi\omega^2}{c^2}\boldsymbol{P}^{(2)} \,. \tag{1.29}$$

Third Order Nonlinear Processes

In analogy to the second order, a term $\boldsymbol{P}^{(3)}$ occurs, describing the third harmonic generation. An additional contribution is important to the generation of fs laser pulses, the so-called Kerr effect. Here, the refractive index becomes dependent on the intensity of the incident laser pulse [Rul98]:

$$N = N_1 + N_2 I \,.$$

This may lead to a self-focussing effect called Kerr lense and is widely used for the generation of ultrashort laser pulses in Ti:Sapphire oscillators, a technique known as self phase modulation.

1.3.2 THz Generation

Low frequency generation in the THz range is possible via difference frequency mixing in non-linear media. The laser pulses used in the experimental setup (790 nm center wavelength, 110 nm bandwidth, 12 fs duration) in principle allow a spectral range of more than 50 THz. Here, the lasing medium is of importance: Application of ZnTe and GaP crystals result in THz radiation below 5 THz (< 20 meV), whereas GaSe crystals are used to obtain a spectrum of 10 to 40 THz ($40 - 160$ meV). The experimental values achieved are presented in Section 2.1.

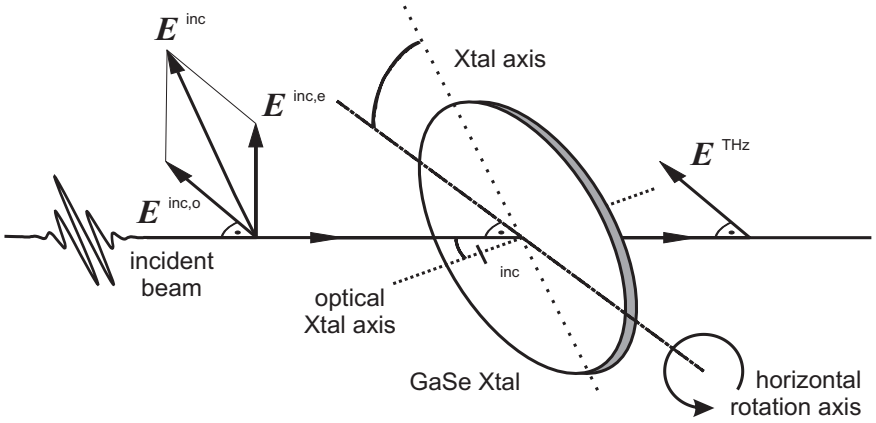

Figure 1.8: *Geometry for THz generation in GaSe. The incident laser pulse with electric field* $\boldsymbol{E}^{\mathrm{inc}}$ *shows two polarization components, an ordinary (o) and an extraordinary (e), respectively. The efficiency of the THz generation can be influenced by tilting the angle* ϑ^{inc} *between the optical axis of the GaSe crystal and propagation direction of the incoming laser pulse. In addition, the crystal can be tilted around its optical axis by the angle* ϕ*.*

The non-linear polarization of a material may be a source for electromagnetic radiation with new frequencies ω, propagating with a phase velocity $v_{\mathrm{ph}} = c/N(\omega)$ through the medium. No destructive interference occur lest we do not find a resulting macroscopic wave. Here, the so-called phase matching condition has to be fulfilled. Therefore, the dispersion has to vanish ($N(\omega) =$ const.), as should be the case in isotropic media. In real matter, this condition is never fulfilled, except for some birefringent crystals which show such a dispersion for special limited frequencies.

Birefringent crystals have two different refractive indices, ordinary N^o and extraordinary N^e, in different crystal directions. Here, phase-matching is achieved with respect to the angle ϑ^{inc} between the optical axis and the wavevector of the incoming wave $\boldsymbol{k}^{\mathrm{inc}}$ and by the difference of N^o and N^e. This will now be described in detail for GaSe [Sch05, KEWE99, HBTL00].

Gallium Selenide

A GaSe crystal is usually used to generate THz radiation in the range of 10 to 40 THz. Figure 1.8 shows the incident laser pulse with electric field $\boldsymbol{E}^{\mathrm{inc}}$ propagating through the GaSe crystal. GaSe is birefringent, showing different refractive indices for different polarization directions. For the two polarization directions $\boldsymbol{E}^{\mathrm{inc,o}}$, $\boldsymbol{E}^{\mathrm{inc,e}}$ one finds:

o - ordinary direction: an angle ϕ between crystal axis and $\boldsymbol{E}^{\mathrm{inc,o}}$ occurs with wavevector $k^o(\omega + \Omega)$ and frequency $\omega + \Omega$, and

e - extraordinary direction: $\boldsymbol{E}^{\mathrm{inc,e}}$ is perpendicular to the optical axis with wavevector $k^e(\omega)$ and frequency ω.

Via DFG a polarization with frequency Ω along (o) is generated, corresponding to type I phase matching (eoo), with high frequency $\Omega + \omega$ polarized in the extraordinary direction, the other frequency ω in the ordinary direction. The resulting THz wave is p-polarized with wavevector $k^o(\Omega)$, proportional to the phase matching via the so called phase matching factor $(e^{\mathrm{i}d\Delta k} - 1)/\Delta k$. Here, $\Delta k = k^o(\omega + \Omega) - k^e(\omega) - k^o(\Omega)$ is the phase mismatch and d the thickness of the crystal.

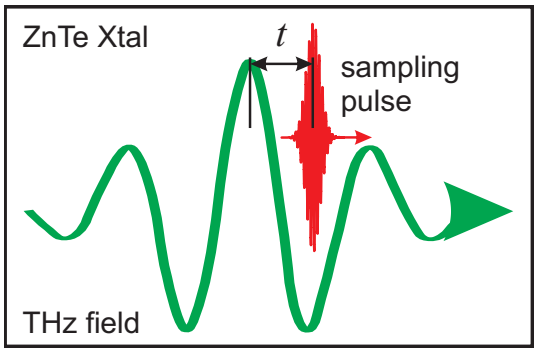

Figure 1.9: *Propagation of the THz pulse and the sampling pulse through the ZnTe detection crystal. The THz pulse induces a birefringence in ZnTe proportional to E^{THz} that leads to a change in polarization of the sampling pulse. By changing the delay t between ultrashort sampling and longer THz pulse the complete electric field of the THz pulse can be measured.*

The phase matching factor has a maximum with vanishing Δk. This is achieved by changing the angle ϑ^{inc} between optical axis and propagation direction. A selection of the center frequency of the THz radiation is possible within certain limits [HBTL00]. An additional degree of freedom is the azimutal angle ϕ, accessible by tilting the generation crystal around its optical axis. Because of the phase matching factor, an efficient THz generation has to fulfill $|d\Delta k \ll 1|$. This is achieved by using thin GaSe crystals with $d < 100\ \mu\mathrm{m}$. In principle, the same scheme can be given for ZnTe and GaP. Here, $N^o = N^e$, different to GaSe, leading to different angles ϑ^{inc} and ϕ. The experimental realization is presented in Section 2.1.2.

1.3.3 THz Detection

The electric field of the THz radiation E^{THz} can be detected by application of a non-linear process of second order, the so-called Pockels effect. Here, a birefringence in a crystal with non-vanishing second order susceptibility $\bar{\bar{\chi}}^{(2)}$ is induced by an external electric field, in this case, the THz field. The induced birefringence can be detected by applying a second weak ultrashort laser pulse propagating collinearly to the THz pulse in the visible range with electric field E^{vis} (see Figure 1.9). While the induced birefringence does not change the amplitude of E^{vis}, the second order correction to the electric field leads to a phase shift. Here, an ellipticity proportional to the induced birefringence occurs, that can be measured with high accuracy as will be presented in Section 2.1.2. Thus, phase and amplitude of E^{THz} are accessible. The advantage of this methodis the measurement of both the real and the imaginary part of the dielectric function $\varepsilon(\omega) = \varepsilon_1(\omega) + \mathrm{i}\varepsilon_2(\omega)$ of a sample. Kramers-Kronig relations are not necessary.

Again, the sensitivity is influenced by the duration of the sampling pulse and the phase matching. A maximum in the ellipticity occurs, where THz pulse and visible sampling pulse propagate through the detection crystal with the same velocity. The ellipticity becomes zero if the sampling pulse sees the complete THz field. Thus, the sampling pulse has to be as short as possible and thin crystals with $d \approx 10\ \mu\mathrm{m}$ have to be used. Thick crystals $d > 100\ \mu\mathrm{m}$ are also suitable due to random phase matching [KNW07].

Zinc Telluride

For the used ZnTe crystal a maximum in efficiency occurs if

- THz and sampling pulse propagate in $[110]$ direction,
- the polarization of the THz and visible electric field are parallel or perpendicular to each other, and
- the polarization of the THz field is parallel to $[001]$ or $[\bar{1}10]$.

Therefore, the sampling pulse is s-polarized in the $[001]$ direction, while the THz pulse is p-polarized in the $[\bar{1}10]$ direction.

Chapter 2

Experimental Details

In this thesis, the temperature dependence of low-energy excitations in the vicinity of the Fermi level in solids are studied for graphite and different superconductors. This is done by using THz radiation to investigate the equilibrium properties as well as the usage of NIR-pump THz-probe technique to study photoexcited states far from the equilibrium.

This chapter presents the experimental details, starting with the femtosecond laser that is used to generate THz pulses and the THz spectrometer in Section 2.1. The preparation of thin graphite, $Bi_2Sr_2CaCu_2O_{8-\delta}$ and MgB_2 samples and the used cryostat are presented in Section 2.2. The work sequence introducing challenges concerning temperature-dependent THz transmission is discussed in Section 2.3 followed by the formalism for the extraction of the dielectric function from the measured THz waveforms from equilibrium as well as pump-probe measurements.

2.1 Experimental Setup

2.1.1 Laser System

Femtosecond laser pulses have been used to generate THz radiation via DFG processes. These pulses originate from a Ti:Sapphire oscillator that is pumped by a 532-nm pump laser. The laser setup is presented in Figure 2.1 and will now be described in detail.

Pump Laser

The pump laser is an internal frequency doubled $\mathrm{Nd{:}YVO_4}$ solid state laser (Verdi V-10, *Coherent Inc.*). The output wavelength is $\lambda = 532$ nm. The continuous wave power (cw-power) is at maximum at $P^{\max} = 10$ W. For pumping the oscillator, $P = 6.75$ W has been applied.

Femtosecond-Ti:Sapphire Oscillator

Ultrashort laser pulses in the NIR have been used to generate THz pulses via DFG. They are provided by a Ti:Sapphire oscillator (FEMTOSOURCE COMPACT M1, *Femtolasers GmbH* [Fem]) with a Ti^{3+} crystal as lasing medium.

The cavity supports longitudinal modes with constant phase, coupled via the so-called mode-locking to get a pulse. Within a Ti:Sapphire oscillator, mode-locking is achieved by the nonlinearity of the Ti:Sapphire crystal. Passive coupling of the modes via the linear optical Kerr effect takes place as has been introduced in Section 1.3.1. Maxima in intensity are focused. The cavity is instable without the Kerr lense, so pulses are preferred to continuous waves. A short pertubation

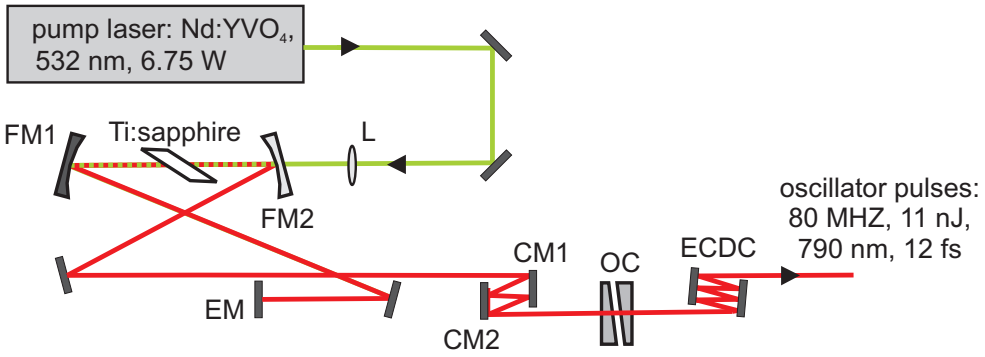

Figure 2.1: *Schematic of the used laser system, consisting of the Ti:Sapphire oscillator and the pump-laser. The components labeled are in the order of their appearance: L - lens; FM1 - concave dispersive mirror; FM2 - concave dichroic mirror; EM, CM1, CM2 - high-dispersive chirped mirrors; OC - output coupler; ECDC - high-dispersive chirped mirrors. The usage of each component is explained in detail in the text.*

starts the self-focusing, realized by a short change of the cavity length (moving of the end mirror EM). The result is a short peak in intensity, that now drives the pulsed mode.

The compensation of the velocity mismatch of the different longitudinal modes in the cavity is important. The group velocity dispersion (GVD) would lead to a temporal dispersion of the pulse. Dielectric mirrors with negative GVD, which reflect shorter wavelengths near their surface, so-called chirped mirrors (EM, CM1, CM2), are used to avoid this. In addition, positive dispersion is pre-compensated via the ECDC, leading to a negative chirp. Here, each double reflection on the two chirped mirrors compensates for the dispersion introduced by 1 mm of BK7 glass.

The applied pulses have an energy of 11 nJ and a duration of 12 fs (FWHM). The center wavelength is 790 nm, with a spectral bandwidth of about 110 nm. A measured sample spectrum is shown in Figure 2.2. A variation in the spectrum with time is observed, since the system is very sensitive to the external conditions.

2.1.2 THz-Spectrometer

The THz-spectrometer is shown in Figure 2.3. A guided description can be given by following the path of one single fs-pulse. The incident pulse is split up into three parts by two beam splitters:

1. generation pulse (30 % of the oscillator output power);
2. sampling pulse (20 %);
3. pump pulse (50 %).

In this order, the pathways through the spectrometer shall be followed below.

Generation Pulse and THz Radiation

The generation pulse passes a delay stage. Here, an access to the temporal delay t between generation and sampling pulse (see Section 1.3.3) is given by a change of the path length. Lock-in technique is applied in the detection. The frequency modulation is realized using a chopper ($\Omega = 8$ kHz) synchronized to a lock-in amplifier (LIA). To achieve the type I phase matching

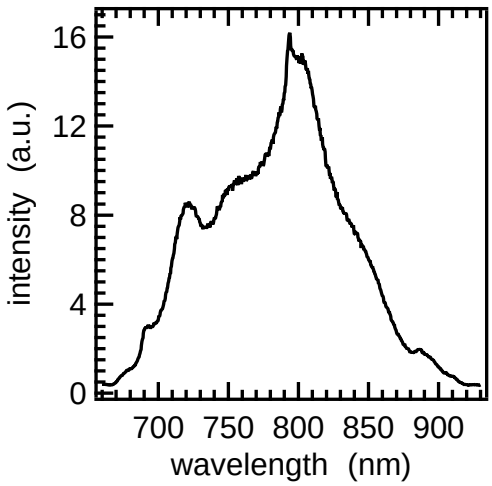

Figure 2.2: *Typical fluorescence spectrum of the fs-Ti:Sapphire oscillator, showing a center wavelength of 790 nm.*

condition for DFG, the polarization is adjusted by transmitting a $\lambda/2$-wave plate. The achieved polarization is 45° with respect to the parallel (p) direction in the case of GaSe and 0° in the case of ZnTe. ZnTe is used to find p-polarized THz pulses in the range from 1 to 3 THz, GaSe to find 12 to 35 THz. The crystal can be rotated around the horizontal axis, to change the center frequency of the resulting THz pulses by changing the phase matching angle ϑ, as shown in Figure 1.8. The resulting THz radiation is collimated by a gold-coated 90° off-axis parabolic mirror (PM1).

A silicon wafer (> 6000 Ωcm, *Crystec GmbH*) is used to block the remaining generation light. Silicon shows nearly no dispersion or absorption in the mid and far IR, except for an absorption line at 18 THz, resulting from a difference-phonon process, whereas NIR cannot transmit. To maximize the transmitted THz radiation, the silicon wafer is mounted at about 44°, the Brewster angle for THz radiation. Then, the THz pulse is focused into the sample by PM2. After sample transmittance, the pulse again is collimated by PM3 and focused into the detection crystal by PM4.

Sampling Pulse and Detection

A polarizer s-polarizes the sampling pulse, which is then focused into the detection crystal. Sampling and THz pulse must traverse the detection crystal collinearly. The s-polarized sampling pulse accumulates an ellipticity as described in Section 1.3.3, proportional to the electric field of the THz pulse. To have it surrounded homogeneously by the THz field, the THz focus is broader than the one of the sampling pulse. By changing the delay t, the THz waveform can be measured. THz and sampling pulse have different duration times, 100 fs and 12 fs respectively (see Figure 1.9). The generation crystal is ZnTe with a thickness of 10 μm, mounted on an optically inactive medium [KNW07].

The elliptically polarized visible sampling pulse now traverses a $\lambda/4$ wave plate, resulting in a pulse that is again linearly polarized, but tilted by an angle $\Delta\alpha$ against the former s-polarization. Finally, a Wollaston prism separates the horizontal and the vertical components of the polarized pulse spacially.

Now, two balanced photodiodes detect the intensities of the polarization components. Measured is the difference in intensity ΔI of the photo currents, which is proportional to $\Delta\alpha$, which is itself proportional to E^{THz}. The lock-in technique enables a measurement of very small differences in the photo currents with less noise.

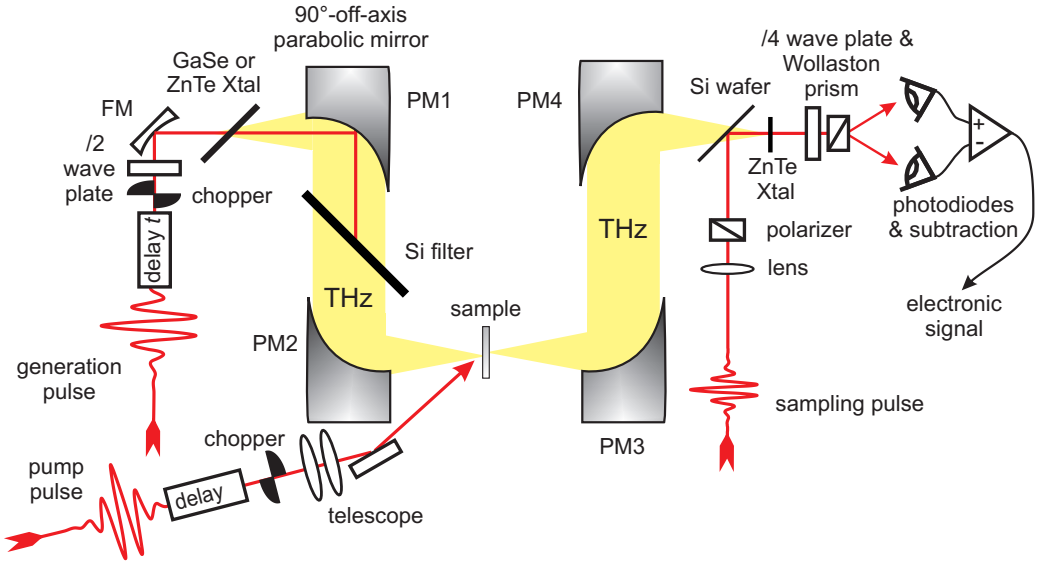

Figure 2.3: *Schematic of the THz spectrometer. A GaSe or ZnTe crystal is used to generate THz radiation that is collimated and then focused into the sample by gold-coated off-axis parabolic mirrors PM1 and PM2. After sample transmission, the THz pulse is collimated again by PM3 and then focused by PM4 into the ZnTe detection crystal collinearly with the sampling pulse. Additonally, a visible pump pulse can be applied, to excite the sample prior to the THz sampling. Further details are mentioned in the text.*

Even small changes in temperature or air fluctuations change the path length in the spectrometer, leading to differences in the delay t between THz and sampling pulse. Such perturbations within one measurement cycle lead to a systematic error in the phase of the THz waveform. To avoid these problems, the setup is thermally stabilized, damped against vibrations and housed in boxes that protect against air fluctuation. This has proved to be important especially for temperature dependent measurements as described in detail in Section 2.3.

The obtained peak's signal-to-noise ratio is 10^4 for long measurement times ($t \sim 100$ ms/delay). The lower limit is the quantum noise of the photo current. Further contributions arise from sample thickness and mounting the sample in the cryostat, introducing two additional diamond windows in the beam path.

Pump Pulse

An additional pump pulse can be applied to excite the sample prior to the THz probe. A variable delay τ with respect to the THz pulse is achieved by using a second delay stage. Pump-induced changes are measured using lock-in technique by applying a second chopper in combination with another LIA. After a lens telescope changes the fluence, the pump pulse is focused on the sample focus of the THz beam by an additional mirror and PM2. A good choice for the chopper frequency ($\Omega = 66$ Hz) guarantees the detection of the unperturbed THz transient $S(t)$ and the perturbed transient $\Delta S_\tau(t)$, or the difference signal $\Delta S(\tau)$.

2.2 Sample Preparation and Mounting

THz transmission experiments at low temperatures have been performed. For these, the sample properties have to fulfill several requirements:

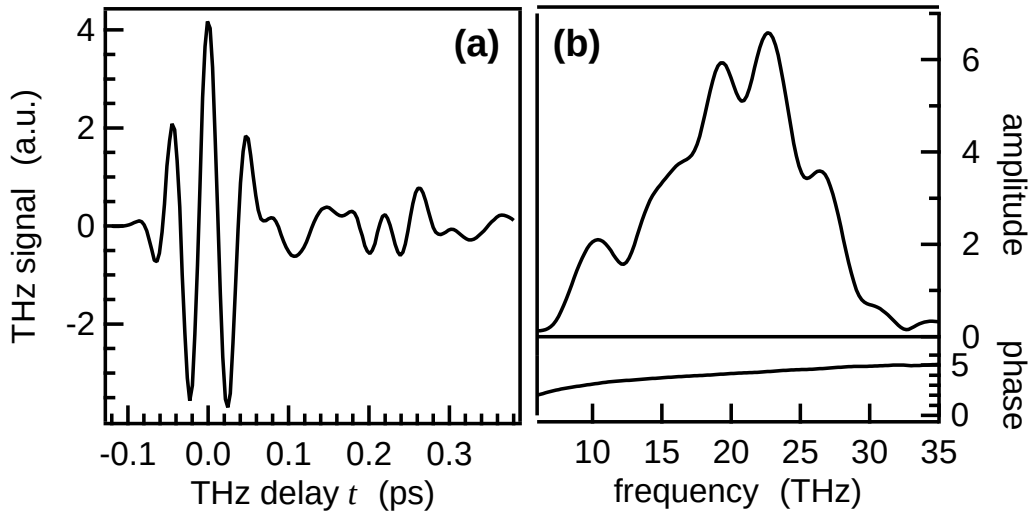

Figure 2.4: *(a) Raw data of a measured THz waveform, generated by a GaSe crystal. (b) A Fourier transform leads to amplitude and phase of the THz pulse.*

- thin sample of homogenous thickness d for THz transmission shows bulk properties;
- thickness must guarantee a homogenous excited probe volume in case of pump-probe experiments;
- lateral sample size is larger than $100\ \mu\mathrm{m}^2$;
- THz-transparent substrate has high thermal conductivity.

To satisfy all these conditions, two decisions have to be made:

1. A suitable substrate has to be chosen. The substrate of choice is diamond in the case of graphite and BSCCO due to good experience from previous work [Kam05, Sch08]. In the case of MgB_2, finally diamond was chosen as well, leading to other restrictions, as discussed in Section 2.2.1.
2. All samples are commercially unavailable and different in their preparation. This leads to the choice between cleaving from bulk crystals or growing from their constituents. Whereas HOPG is commercially available in large crystals and shows bulk properties starting from at least 30 layers (10 nm) [NDSvD09], BSCCO has to have a macroscopic size > 50 nm to ensure superconducting properties. In both cases, cleaving with sticky tape has been used to obtain samples. For MgB_2 even small crystals are unavailable. Here, the sample-preparation technique applied succesfully for graphite and BSCCO was changed to sputtering technique.

2.2.1 Samples

Graphite

Since the first preparation of graphene in 2004 [NGM+04] much progress has been made in preparing thin films of layered materials by cleaving with sticky tape. Here, THz transparent *TESA Kristallklar* provided by *Beiersdorf AG* has been used [Kam05, KPS+05] to prepare graphite samples on diamond substrates without TESA covering. This effort has been necessary because sticky tape is harmed by cryogenic temperatures.

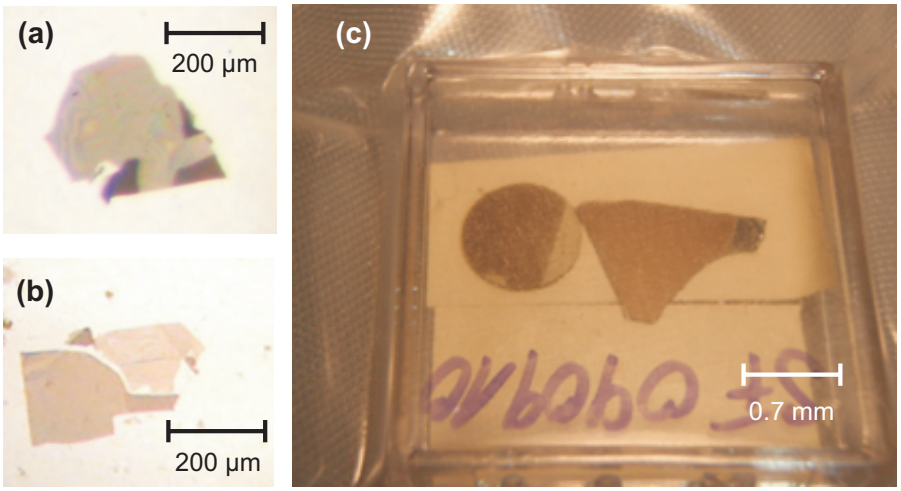

Figure 2.5: *Pictures of the samples used: (a) HOPG with different thicknesses, indicated by different levels of grey, (b) BSCCO with $T_c = 80$ K and (c) MgB_2 samples with silcon (left) and diamond (right) as substrate. For storage, MgB_2 samples are encapsulated.*

The preparation in detail is as follows: Graphite samples are made by cleaving a HOPG crystal (Highly Oriented Pyrolytic Graphite) ZYB grade provided by *GE Advanced Ceramics* with sticky tape and transferring a thin film to the diamond substrate. Acetone is used to solve the glue of the sticky tape and thus seperate sample from sticky tape. The substrates are provided by *Diamond Materials GmbH* and additionally polished at Humboldt Universität Berlin [Söl] to ensure a flat surface. This was found to be necessary for a good thermal contact between sample and substrate, important in pump-probe experiments. Here, diamond provides a high thermal conductivity covering the whole temperature range to guarantee the transport of heat out of the sample.

During the preparation process, the sample thickness has been roughly estimated using a microscope. The thickness was then measured by the transmission of 632.8 nm-light (see Appendix B). Sample properties are presented in table 2.1. A picture of graphite is shown in Figure 2.5(a).

As previously mentioned, acetone has been introduced in the preparation process. Thus, some unintentional doping or damage of the graphite has to be excluded. Reference data from [Kam05] measured at room temperature have been compared to data measured at the two-layer samples (see Section 3.2) and show no differences. So a damage of the sample can be ruled out.

Cuprates

The cuprate used is $Bi_2Sr_2CaCu_2O_{8-\delta}$. The samples have been prepared in analogy to the graphite samples, since cuprates are layered systems (see Section 4.2). Here, several crystals with different doping levels and T_c have been used, provided by two different sources:

1. Optimally doped, $T_c = 91$ K, $\delta = 0.16$, Japan [Eis];
2. Underdoped, $T_c = 85$ K, $\delta = 0.13$, Japan;
3. Underdoped, $T_c = 80$ K, $\delta = 0.12$, Japan;
4. Strongly underdoped, $T_c = 68$ K, $\delta = 0.105$, France [Pal];

The thicknesses are measured as in the case of graphite. Again, sample properties are presented in table 2.1, a picture for $T_c = 80$ K is shown in Figure 2.5(b).

sample	substrate	T_c (K)	d (nm)	size (μm)	d substrate (mm)
graphite	diamond	-	32	200×200	0.34
BSCCO	diamond	68	139 ± 4	150×100	0.31
		80	66 ± 4	200×200	0.33
		85	62 ± 4	150×150	1.22
		91	123 ± 2	600×300	0.33
MgB_2	silicon	20	30	5000×5000	0.375
	diamond	20	30	5000×5000	0.3

Table 2.1: *Properties of the measured samples.*

As in the case of graphite, preparation-induced damages of the sample would lead to changes for example in T_c and have to be excluded. Hence, the critical temperatures have been evaluated from the obtained data.

Magnesium Diboride

Magnesium diboride crystals with sufficient size are commercially unavailable. The preparation has been done at Universität Bielefeld using a sputtering technique [FTMT10]. To achieve a homogeneous thin film of superconducting MgB_2, the sample is grown on a heated substrate by deposition with rf-magnetron sputtering of boron and dc-magnetron sputtering of magnesium simultaneously. Finally, a MgO capping layer of 3 nm has been grown to reduce the roughness of MgB_2. Since samples have been grown on the THz intransparent substrate MgO to minimize the lattice mismatch, much had to be done to achieve in samples of sufficient size, thickness and T_c on THz transparent substrates. After several steps, trying different substrates, thicknesses of samples as well as coverage layers, it became possible to grow MgB_2 samples on diamond without a covering layer. Here, a T_c of 20 K has been achieved. Sample properties as well as a picture are presented in Table 2.1 and Figure 2.5(c), respectively.

While graphite and BSCCO do not show any aging, MgB_2 is strongly hygroscopic and its surface degrades rapidly [UTS$^+$03], so it has to be stored encapsulated in a dry atmosphere.

2.2.2 Cryostat

For low-temperature measurements a *KONTI-Kryostat für Mikroskop* (*CryoVac*, Troisdorf [Cry]), shown schematically in Figure 2.6, is used. Sample holder and cover are specially made for THz measurements, the entrance windows are changed to diamond. The cryostat is evacuated by using a turbomolecular pump with rotary vain pump, resulting in pressures better than 10^{-4} mbar, to thermally seperate sample and surrounding.

Cooling is possible with liquid nitrogen (LN) or liquid helium (LHe). The sample itself is mounted on a copper block. Thermal contact is provided via the copper-substrate interface at which the copper block is in contact with the cooling medium and additionally contacted to a Si diode for measuring the temperature. A PID heater enables temperature regulation. All is set in the controller TIC 304-M. The accuracy of the temperature measurement is better than 1 K [Sch08]. Further improvements in stability of LHe flow leads to changes smaller than 0.1 K for several hours. The thermal drift is less than 2 μm in accordance with manufacturer information, and hence much smaller than the THz focus.

The cryostat is placed between PM2 and PM3 at the sample position, in such a way that the THz transmission is at its maximum. Micrometer screws allow the adjustment of the sample position. As Figure 2.6 shows, the LHe comes from top. This configuration leads to cold air falling into

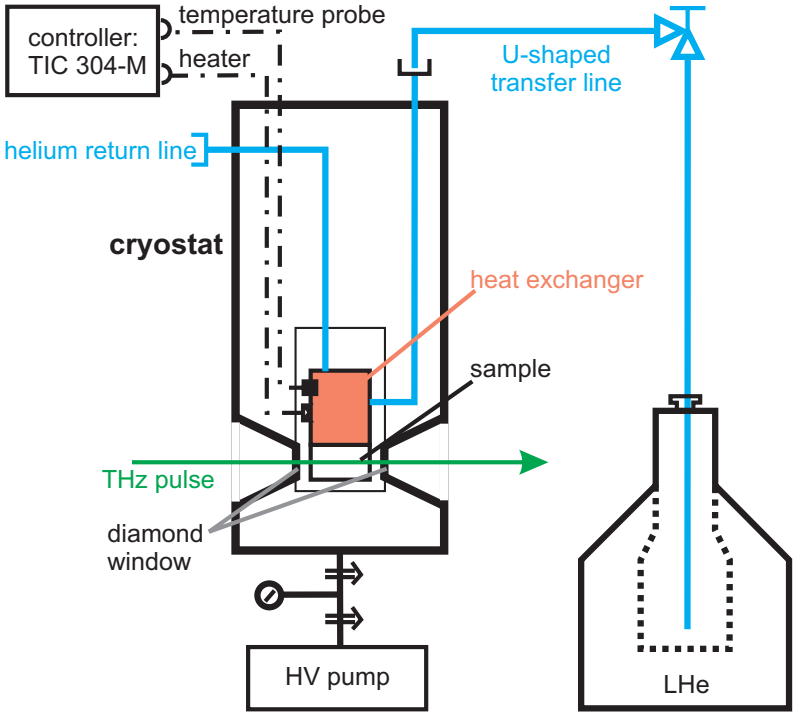

Figure 2.6: *Schematic of the cryostat. The volume is evacuated using a HV pump. The sample is contacted to the heat exchanger (copper). A PID heater (TIC 304-M) additionally contacted to the copper controls the sample temperature. In addition, the way of the LHe is drawn.*

the setup, due to ice formation at the LHe-outlet by vaporization cooling. The resulting air flow influences the measurements as mentioned in Section 2.1. The solution to that problem will be presented in Section 2.3.1.

2.3 Measurement Procedure and Data Acquisition

The setup presented in Section 2.1 allows both temperature-dependent measurements of just the THz transient and measurement of the changes in the THz transient after photoexcitation with a NIR pulse. It turns out that measurements at equilibrium conditions (also called *static* measurements) are much more sensitive to the surrounding than pump-probe measurements. Since static measurements are necessary to understand the non-equilibrium dynamics, much effort has been made to increase the stability of the measurement conditions and the data quality.

This section deals with the requirements of temperature-dependent THz transmission experiments as well as the evaluation of the dielectric function $\varepsilon(\omega, T)$ from the raw data.

2.3.1 Measurements at Equilibrium Conditions

Optical properties of some materials are obtained by comparing the sample response R to a reference response R_{ref}, i.e. the substrate. The data evaluation is discussed in detail in Section 2.3.3. The THz transmission of both systems, sample/substrate and substrate without sample, respectively, has to be measured. Therefore it is important to have:

- homogeneous sample and substrate,

- reliable and repeatable access to the position of sample and substrate.

The first condition applies to the sample preparation and the choice of the measured spots, the second one to the motion of the cryostat and the stability of the experimental setup as well as its surroundings. The spot position is changed via micrometer screws. Here, a computer-controlled motor is used, achieving a resolution of better than $0.1\ \mu$m. To guarantee the homogeneity of the substrate a position near the sample is chosen. Thus, both conditions are fulfilled: sample and reference positions are repeatable within a short period of time.

The sample position is chosen by the appearance of a pump-probe signal. This guarantees the sample to be at both THz and pump focus. For graphite and BSCCO samples, this procedure always applies. For MgB_2 it is not clear whether there is a pump-probe signal or the pump-pulse destroys the sample. Therefore, the intensity of the pump beam has been decreased and the MgB_2 sample was then brought into its focus after finding a pump-probe overlap on a graphite reference. The consecutive measurement of both sample and reference has turned out to be necessary to obtain high quality data. Summing up all steps of the work sequence, it takes about half an hour for each temperature to measure a static data set. Thus, to achieve a narrow temperature grid the experimental setup must be stable for a least one day. Especially the temporal and spacial overlap of THz and sampling pulse in the detection crystal (see Section 1.3.3) is of importance.

While measuring, the spectrometer is covered to avoid external influences. This has been necessary especially for the cryostat as mentioned in Section 2.2.2. Here, ice appears connected to cold air falling into the setup and finally increasing the noise. For measurements at low THz frequencies, the setup is additionally purged with N_2 to avoid absorption of THz radiation in humid air.

To summarize, static measurements need the whole setup isolated from the surroundings as well as possible, guaranteeing a high repeatability of sample and reference position as well as laser performance and overlap of THz and sampling pulse in the detection crystal. This has been achieved by automatization of the measurement procedure, shielding of the setup and accurate preparation of the measurements.

2.3.2 Pump-Probe Measurements

In contrast, pump-probe measurements do not need a motion of the sample leading to a better repeatability. Sample and reference are on the same position because changes between perturbed and unperturbed system are measured.

Nevertheless, measurements of this kind take more time due to the lower signal-to-noise ratio and the additional coordinate found in the pump-probe delay τ. To understand the relaxation dynamics, it is necessary to measure a sequence of delays τ. This takes several hours per temperature because of the longer average time. Therefore, only few temperatures have been measured to achieve $\varepsilon_\tau(\omega, T_a)$. Application of the cryostat leads to an additional disadvantage in fluence-dependent measurements. Here, the relation of applied and absorbed fluence is indetermined due to the additional diamond entrance window in the beam path.

To get limited information on the temperature-dependent decay constants, a compromise between signal-to-noise ratio and measurement time can be found. Here, just the maximum of the pump-induced signal $\Delta S(\tau, T_a)$ is measured (*PP-scan*). It includes information on the dynamics as has been shown previously [vV09]. To avoid drift effects, this requires an optimization of the pump-induced signal concerning the THz delay t for each temperature T_a. Measurements showing the required narrow temperature grid can be performed within one day.

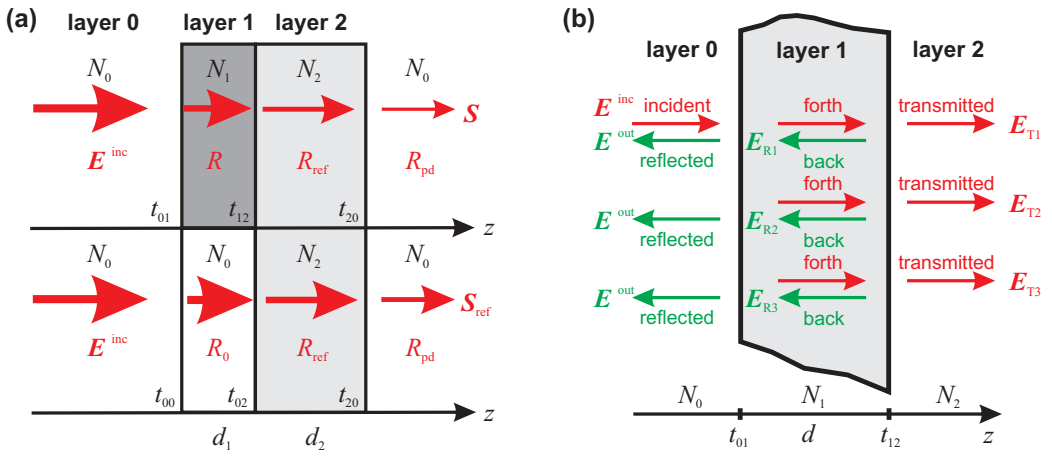

Figure 2.7: *(a) The two cases in equilibrium measurements. Upper part: the incoming laser pulse traverses layer 1 (sample) and layer 2 (substrate) with optical properties different from layer 0. Lower part: the incoming laser pulse traverses layer 1 with the same optical properties as layer 0 and substrate-layer 2. (b) Schematic of the sample layer 1. The incoming laser pulse undergoes multiple reflections in sample layer 1, each accounts for a part of the measured signals by* $E_{\mathrm{T}i}$.

To summarize, pump-probe measurements are of a higher reproducibility compared to static measurements but take longer time. PP-scans provide information on the dynamics in the temperature domain, accompanied with pump-probe measurements at few temperatures. An estimate of the time effort for preparation and measurement may conclude this section:

1. preparation of laser and setup, optimization: about 1 day,
2. static measurements: 1 day,
3. pump-probe measurements: 1 day for each temperature,
4. PP-scans: 1 day.

In conclusion, temperature-dependent THz-transmission measurements take much effort and are time-consuming. Thus, much attention has been paid to stable measurement conditions.

2.3.3 Extraction of the Dielectric Function from the THz Waveforms

Optical properties of a sample are represented by its dielectric function ε. This section deals with the evaluation of ε from the measured THz waveforms. Since two layer systems have been used, multiple reflections must be taken into account. In addition, changes in the extraction formalism for a three layer system [Kam05] will be adressed [Web09, TH90].

Due to the chosen transmission geometry, a light propagation in z-direction only is considered, resulting in a one-dimensional model. The incident electromagnetic waves are treated as plane waves. In Figure 2.7 the THz pulse $\boldsymbol{E}^{\mathrm{inc}}(r,t)$ enters from the left and traverses sample (layer 1) and substrate (layer 2). It is finally detected as $S_1(r,t)$. The same happens with the reference signal $S_0(r,t)$, except for the missing sample. So, the optical properties of layer 1 are identical to those of layer 0. A linear response of the sample is assumed. The system can be described by linear time invariant system theory [PWK07] and $S_i(r,t)$ is a convolution of $\boldsymbol{E}^{\mathrm{inc}}(r,t)$ with transfer function $h_i(r,t)$ and substrate transfer function $h_{\mathrm{ref}}(r,t)$:

$$S_i = h_i \cdot h_{\mathrm{ref}} \cdot h_{\mathrm{pd}} \cdot \boldsymbol{E}^{\mathrm{inc}} \,. \tag{2.1}$$

In addition, $h_{\mathrm{pd}} = h_{\mathrm{p}} h_{\mathrm{p}}$ accounts for the response of propagation and detector, respectively. Applying Parseval's theorem, for the frequency domain with (k, ω)-dependencies

$$S_i = R_i \cdot R_{\mathrm{ref}} \cdot R_{\mathrm{pd}} \cdot \boldsymbol{E}^{\mathrm{inc}} \tag{2.2}$$

holds. The transfer function for the sample material is given by:

$$Q = \frac{S_1}{S_0} = \frac{R_1}{R_0} \, .$$

Pump-probe measurements additionally include the delay τ between pump and sampling pulse to the THz delay t, resulting in a two dimensional grid of data (see Figure 2.8). The difference signal of excited and unexcited sample is defined as:

$$\Delta S_\tau(t) = S_\tau(t) - S_\infty(t) \, .$$

For the spectral information a Fourier transform of the raw data is necessary, with $t \rightarrow \omega$ and $\tau \rightarrow \Omega$, respectively. The change in the signal $\Delta S_\Omega(\omega)$ is connected to the change of the electric field $\Delta E_\Omega(\omega)$ after transmission of the sample by

$$\begin{aligned} \Delta S_\Omega(\omega) &= R_{pd}(\omega) \Delta E_\Omega(\omega) \\ &= R_{pd}(\omega) \Delta R_\Omega(\omega - \Omega) E^{\mathrm{inc}}(\omega - \Omega) \, , \end{aligned}$$

defining the pump-induced sample response ΔR_Ω. In analogy to Equation (2.1) the reference signal of the unexcited sample may be $S_\infty = R_{pd} R_\infty E^{\mathrm{inc}}$, so that

$$\Delta Q_\Omega(\omega) = \frac{\Delta R_\Omega(\omega - \Omega)}{R_\infty(\omega)} \frac{E^{\mathrm{inc}}(\omega - \Omega)}{E^{\mathrm{inc}}(\omega)} \tag{2.3}$$

follows. Due to the broad bandwidth of the THz pulses, E^{inc} shows a flat spectrum, so that the second term is well approximized by $E^{\mathrm{inc}}(\omega - \Omega)/E^{\mathrm{inc}}(\omega) \approx 1$.

Finally, the equations for the sample response for measurements on the unexcited and excited sample have been obtained:

$$Q(\omega) = \frac{S(\omega)}{S_{\mathrm{ref}}(\omega)} \, , \qquad \Delta Q_\tau(\omega) = \frac{\Delta S_\tau(\omega)}{S_\infty(\omega)} \, . \tag{2.4}$$

Equilibrium Conditions

Each medium may has a thickness d_i and a refractive index N_i. The incident pulse $\boldsymbol{E}^{\mathrm{inc}}$ is considered to be perpendicular to the layers. Fresnel coefficients [DBM01] for transmission t_{ij} and reflexion r_{ij} can be used:

$$t_{ij} = \frac{2N_i}{N_i + N_j} \qquad r_{ij} = \frac{N_i - N_j}{N_i + N_j} \, . \tag{2.5}$$

According to Figure 2.7, the incident wave, coming from layer 0, is partly transmitted through and reflected at the interface of layer 0 and layer 1 (01). Since only the transmitted part is detected, the reflected part at (01) is not mentioned further. It holds:

$$E_1 = t_{01} E^{\mathrm{inc}} \, .$$

The same occurs at the interface of layer 1 and layer 2 (12). Now the reflected part leads to multiple reflexions at (01) and (12) which have to be taken into account for thin samples. For the thick substrate, the first back-reflexion is on the picosecond time scale and thus is not considered. After the first transmission through (01) and reflexion at (12), we find:

$$E_{\mathrm{R1}} = t_{01} r_{12} e^{2\mathrm{i}k_1 d_1} E^{\mathrm{inc}} \, ,$$

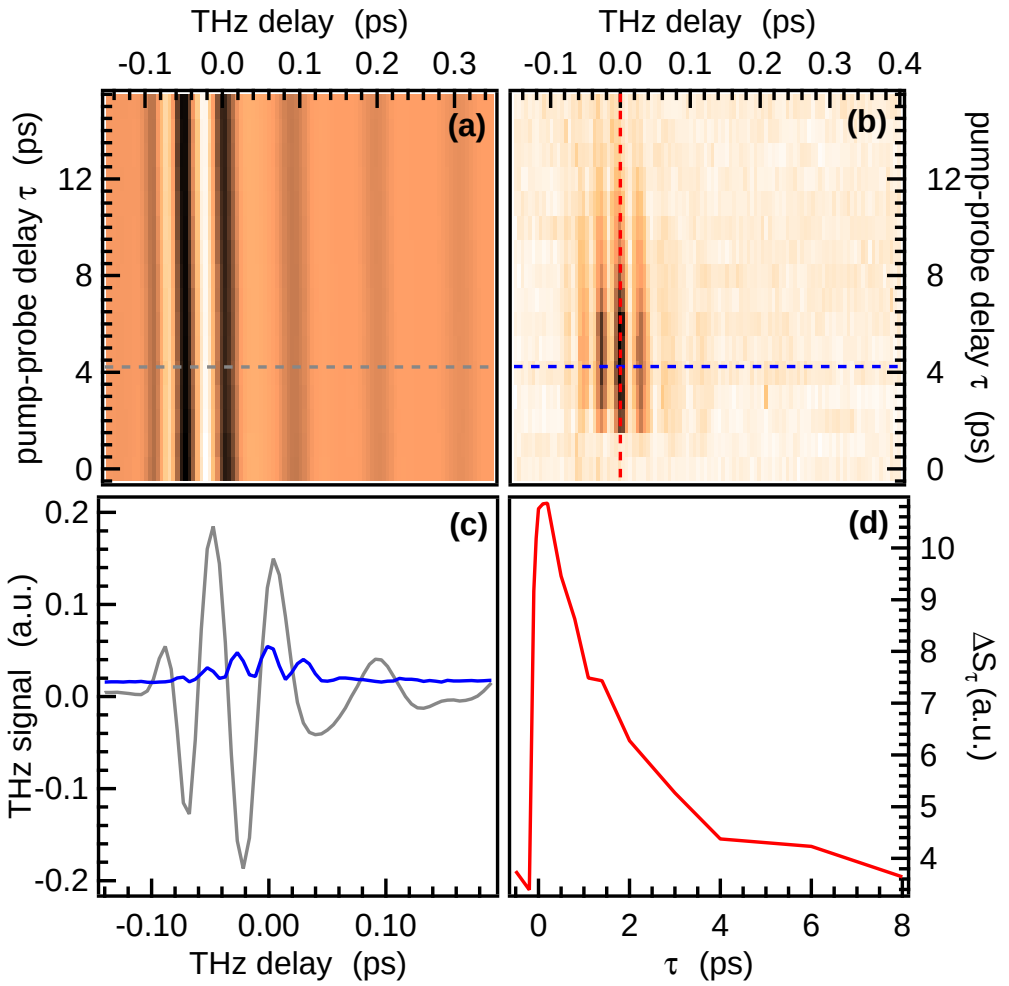

Figure 2.8: *(a) Grid of unperturbed pump-probe data. (b) Grid of pump-induced changes. (c) Cuts along the THz delay from panels (a) and (b) as marked by colored lines: Unperturbed THz waveform (grey) and pump-induced changes (blue). (d) Cut along the pump-probe delay (red) from panel (b), resulting in a PP-scan.*

whereas the directly transmitted part is:

$$E_{\mathrm{T}1} = t_{01}t_{12}e^{\mathrm{i}k_1 d_1}E^{\mathrm{inc}} \,.$$

Since the detected signal is the sum $S = E_{\mathrm{T}1} + E_{\mathrm{T}2} + E_{\mathrm{T}3} + \ldots$, it is convenient to introduce a factor M_i that accounts for multiple reflections:

$$M_i = 1 + r_{0i}r_{i2}e^{2\mathrm{i}k_i d_1} + \left(r_{0i}r_{i2}e^{2\mathrm{i}k_i d_1}\right)^2 + \ldots = \frac{1}{1 - r_{0i}r_{i2}e^{2\mathrm{i}k_i d_1}} \,. \tag{2.6}$$

In case of the reference, $M_0 = 1$. Thus the detected signals can be described as

$$S_i = t_{0i}e^{\mathrm{i}k_i d_1}M_i t_{i2}e^{\mathrm{i}k_2 d_2}t_{20}E^{\mathrm{inc}} \,.$$

By introducing the phase shift at the sample $\delta = k_1 d_1$, the measured signals S_i from Equation 2.4 lead to

$$Qe^{\mathrm{i}k_0 d_1}\frac{2N_0}{N_0 + N_2} = \frac{t_{01}t_{12}}{e^{-\mathrm{i}\delta} - r_{10}r_{12}e^{\mathrm{i}\delta}} \,. \tag{2.7}$$

Using $\varepsilon = N_1^2$ and assuming a thin sample layer 1, so that $\delta = k_1 d_1 = \omega N_1 d/c \ll 2\pi$, one can expand to the second order: $e^{i\delta} \approx 1 + i\delta - \delta^2/2$ and find an expression for the dielectric function:

$$\varepsilon = -\frac{c}{\omega d_1} \frac{\mathrm{i}\,(N_0 N_2)\,\omega d_1/c + (N_0 + N_2)\,e^{-\mathrm{i}k_0 d_1}/Q - N_0 - N_2}{\mathrm{i} + (N_0 + N_2)\,\omega d_1/2c} \tag{2.8}$$

This will be referred to as the *thin-film formula*. The thin-film formula can be applied with first order corrections to samples up to 10 nm, in second order up to 200 nm. Thicker samples have to be treated in a different way [Web09]. Since samples used here are in the range of $30 - 150$ nm, Equation (2.8) is sufficient.

Pump-probe measurements

Since the sample is much thinner as compared to the wavelength of the THz pulse, one sets $e^{\mathrm{i}k_1 d_1} = 1$. The pump-induced changes of the response function then yield [Kam05]:

$$\Delta R_\Omega(\omega - \Omega) = \frac{\Delta E_\tau(d_1 + 0^+, \omega)}{E^{\mathrm{inc}}(\omega - \Omega)} = \frac{\mathrm{i}d_1\omega}{2cN_0(\omega)} R_\infty(\omega) R_\infty(\omega - \Omega) \Delta\varepsilon_\Omega(\omega - \Omega)\ .$$

Here, a homogenously excited sample is assumed as well as

$$R_\infty = \frac{E^{(0)}(d_1 + 0^+, \omega)}{E^{\mathrm{inc}}} = \frac{t_{01} t_{12}}{1 + r_{01} r_{12}} = t_{02}$$

for the unexcited sample. Using Equation (2.3), one finds:

$$\Delta\varepsilon_\Omega(\omega) = \frac{2cN_0(\omega + \Omega)}{\mathrm{i}(\omega + \Omega) d_1 R_\infty(\omega)} \Delta Q_\Omega(\omega + \Omega)\ . \tag{2.9}$$

Now application of an inverse Fourier transform $\Omega \to \tau$ of $\Delta\varepsilon_\Omega(\omega)$ leads to the pump-induced changes of the dielectric function $\Delta\varepsilon_\tau(\omega)$ as a function of the pump-probe delay τ. For slow changes with $\omega + \Omega \approx \omega$ one obtains a quasi-static solution:

$$\Delta\varepsilon_\tau(\omega) = \frac{2cN_0(\omega)}{\mathrm{i}d_1\omega R_\infty(\omega)} \Delta Q_\tau(\omega)\ . \tag{2.10}$$

For delays $\tau > 0.1$ ps after excitation, this equation is in good agreement with Equation (2.9).

There are two possibilities to obtain pump-probe results, as mentioned in Section 2.3.2:

PP-scan: difference signal $\Delta S(\tau)$ between excited and unexcited sample is measured for a fixed THz delay t dependent on the pump-probe delay τ. An example is shown in Figure 2.8(d).

Line-scan: difference signal $\Delta S_\tau(t)$ of the THz waveform transmitted through the excited and unexcited sample at pump-probe delay τ is measured, resulting in a two-dimensional matrix of raw data as presented in Figure 2.8. Fourier transformation and Equation (2.10) lead to the changes in the dielectric function.

Chapter 3

Graphite

Graphite and its monolayer graphene [NGM+04] are promising materials for electronic applications due to their ability to sustain high current densities [MBB07, BLM+09, BHM+10]. Here, transport properties are of special interest. Applications in MIR photonics are also conceivable. Here, graphite may be useful in intensity and phase modulators.

This chapter deals with the temperature dependence of the MIR optical properties of graphite. First, electronic and phononic properties of graphite are introduced in Section 3.1. Thermal heating is found to make graphite more transparent for THz radiation. This behavior is understood by means of electronic transitions in Section 3.2. Photoexcitation leads to similar effects as thermal heating and paves the way to an understanding of different aspects of energy relaxation. On the one hand, the temperature dependence of the photoinduced changes shows the thermalization of electrons and subsequent heating of only few strongly-coupled optical phonon (SCOP) modes on a sub-picosecond scale in Section 3.3. On the other hand, energy relaxation on a picosecond timescale via phonon cooling is investigated in Section 3.4. Here, temperature-dependent measurements of the relaxation of the photoinduced changes show SCOP modes to decay via scattering with low energy phonons. Parts of Section 3.4 has been published in [SKW+11].

3.1 Properties of Graphite

3.1.1 General Properties

Graphite is a stacked material consisting of hexagonal layers of carbon atoms as shown in Figure 3.1. A single layer is called graphene and was first produced in 2004 [NGM+04], while its theoretical description has been developed more than half a century ago [Wal47]. Graphite is widely used for its physical properties as may be illustrated by two complementary examples:

- Its weakly coupled layers make it a favorite material for pencils.
- Its electrical conductivity leads to applications as electrodes, pointing towards microelectronics.

These examples reveal three basic features of graphite:

1. it is simply structured, easily available, cheap and consists only of carbon atoms;
2. because of its layered structure it is easy to process and shows unique physical properties;
3. due to its electronic properties it acts as a semimetal under equilibrium conditions [NGP+09].

In this work, a fourth property is investigated: graphite also shows unique optical properties that may be exploited in photonic applications.

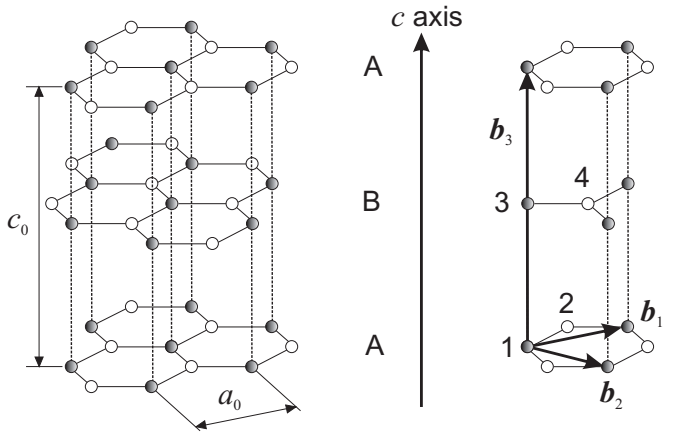

Figure 3.1: *Lattice structure of graphite. The AB-stacking of the hexagonal structure is shown. The color of the carbon atoms marks the coordination site. Right panel shows the characteristic length from Table 3.1.*

The layered structure, strong in-plane and weak out-of-plane bonding determine peculiar electronic and phononic properties, which will be used to understand especially the phonon-phonon interaction.

Synthesized Highly Oriented Pyrolytic Graphite (HOPG) is used here, produced by pyrolysis of hydrocarbons in the gasphase, growing layer by layer on a substrate. These carbon layers then are baked by more then 2500°C under high pressure. This then leads to highly oriented graphite, with crystallites of a size of some 10 μm parallel to the layers and some 10 nm perpendicular to the layers [OBM+97]. The orientation of the crystallites in HOPG is not perfect, since they are slightly tilted around the c-axis, but better than in the case of naturally grown graphite with randomly oriented crystals of some micrometers in size.

3.1.2 Electronic Structure

Graphite exhibits a hexagonal crystal structure with AB-stacking. Thus, only two lattice positions with different coordinations occur. As Figure 3.1 illustrates, half of the carbon atoms are located directly above each other in adjacent planes (dark atoms in Figure 3.1), while the other half are located above the center of the hexagon in the adjacent plane (light atoms in Figure 3.1). Carbon atoms in each layer are covalently bound, while the layers are bound to each other by Van-der-Waals forces. All atoms are sp^2 hybridized, leading to an angle of 120° as necessary for the hexagonal structure. At room temperature, the following lengths have been found [TR82]:

lattice constant a_0	0.2462 nm
bounding length l_0	0.1421 nm
distance of A- or B-layers c_0	0.6707 nm

Table 3.1: *Characteristic lengths of graphite used for data evaluation [TR82].*

A temperature dependence of the lattice constant will be neglected, since different values are suggested between $a_0 = 0.2459 \pm 0.0005$ nm and $a_0 = 0.2449$ nm at low temperatures [WR04] that will virtually not affect the calculation done here.

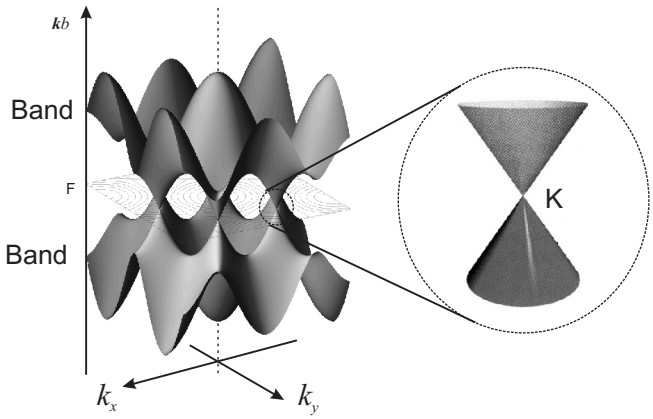

Figure 3.2: *Electronic structure of graphene. The three-dimensional model is taken from [Hag05]. Inset shows the conical band structure around the K point with zero bandgap at E_F, leading to the linear dispersion of graphene.*

Since valence and conduction bands have only small overlap, graphite is a semimetal under equilibrium conditions [NGP$^+$09]. After photoexcitation of electrons this turned out to be not quite as clear-cut. Here, also a semiconducting scenario was proposed [BRE09]. Since such behavior would have impact on the energy relaxion, low-energy probing in the THz range of photoexcited states may reveal an answer to that question.

A theoretical description is provided by using a tight-binding approach which neglects layer interaction: the graphene model [Wal47], as will be mostly adequate for a qualitative description of graphite. Later on, this simplification must be corrected by additional inclusion of layer-layer interaction leading to qualitative changes in the band structure around E_F. This so-called Slonczewski-Weiss-McClure (SWM) model provides a good approximation of the electronic band structure of graphite in the vicinity of the Fermi energy.

Graphene: Thight-Binding Model

Since graphene is a honeycomb monolayer, layer-layer interaction is neglected leading to no band overlap at the K and K' points, in contrast to graphite. Instead, valence and conduction bands touch each other forming a zero band gap.

In the monolayer, the orbitals 2s, 2p$_x$ and 2p$_y$ are hybridized and become three sp^2-orbitals, forming three bounding σ-bonds and three antibounding σ^*-bonds. The remaining 2p$_z$-orbitals form one π and one π^* band. The Fermi energy then is located in the middle of the band crossing. Since σ-bands are not in the low energy regime, π-bands are responsible for low-energy optical excitations and the electron dynamics around E_F [DDS$^+$88]. The resulting band structure is shown in Figure 3.2. The tight-binding approach includes a large periodic background potential, in contrast to the quasi-free electrons of the Bloch model [Czy04], and treats the π-bands as degenerate with respect to k_z.

Figure 3.3(b) shows the two-dimensional BZ of graphene in (k_x, k_y) direction, with symmetry points K and Γ. The linear dispersion near to K and K' (see inset from Figure 3.2) is given by:

$$\epsilon_{\boldsymbol{k}\pi^*} = +\frac{\sqrt{3}}{2} a_0 \gamma_0 \left|\boldsymbol{k}\right| \; ; \qquad \epsilon_{\boldsymbol{k}\pi} = -\frac{\sqrt{3}}{2} a_0 \gamma_0 \left|\boldsymbol{k}\right| \; .$$

Here, $\gamma_0 = 3.16$ eV defines the overlap integral of two neighboring atoms and is also used for graphite (see Table 3.2). According to [NGP$^+$09], the eDOS of graphene near to K and K' is approximated by:

$$D(E) = \frac{3\sqrt{3} a_0^2 \left|E\right|}{\pi v_F^2} \; , \tag{3.1}$$

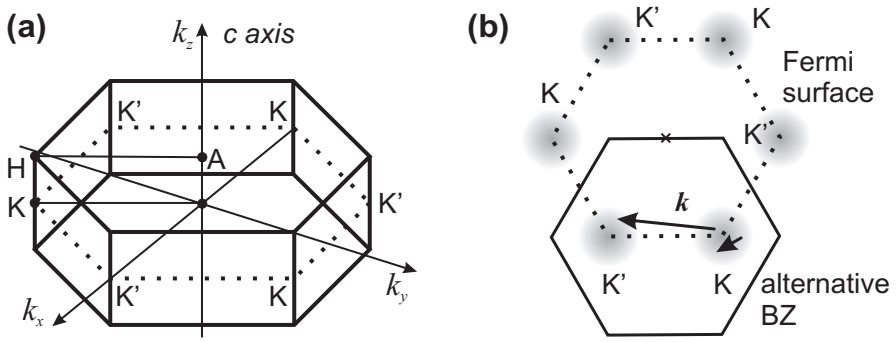

Figure 3.3: *(a) Conventional hexagonal Brillouin zone of graphite with points of high symmetry. (b) Two dimensional Brillouin zone and Fermi surface of graphene. Two possible transitions* $\Delta\boldsymbol{k} \approx \vec{KK} \approx 0$ *and* $\Delta\boldsymbol{k} \approx \vec{KK}'$ *are shown.*

with $v_F \approx 10^6$ ms^{-1}. This is included in Figure 3.4(b) and shows significant differences to the eDOS of graphite. Though the graphene model has been often applied to describe physical properties in an intuitive way, THz experiments will show the limits arising from interlayer effects.

Graphite: Slonczewski-Weiss-McClure Model

The tight-binding model for graphene treats the π-bands to be degenerate with respect to k_z. If one takes the layer-layer interaction into account, this two-fold degeneration splits up. The semi-phenomenological Slonczewski-Weiss-McClure model (SWM) [McC57, SW58] for the band structure of graphite is applied, resulting in a 4×4 hamiltonian that is compatible with the symmetries of the graphite lattice. It involves seven free parameters (Table 3.2) that are determined by fits to results of appropriate experiments as well as *ab-initio* calculations [TR82]. The SWM model exploits that the Fermi surface of graphite is in the proximity of the HKH and H'K'H' line in the BZ as suggested by the graphene model (Figures 3.2 and 3.3). It is convenient to choose the so-called alternative BZ (Figure 3.3(b)), setting the Fermi surface in the BZ center. Here, the electron wavevectors of interest are

$$\begin{aligned} \boldsymbol{k} &= \boldsymbol{k}_c + \boldsymbol{k}_\perp \\ &= \boldsymbol{k}_c + \vec{\Gamma\mathrm{X}} + \boldsymbol{\kappa} \text{ with } \mathrm{X} \in \{\mathrm{K}, \mathrm{K}'\} \ , \end{aligned}$$

defining $\boldsymbol{k}_c \parallel \boldsymbol{k}_z$ and $\boldsymbol{k}_\perp \perp \boldsymbol{k}_c$. The small translation $\boldsymbol{\kappa}$ is defined in cylindrical coordinates, introducing α, the angle between $\boldsymbol{\kappa}$ and $\vec{\Gamma\mathrm{K}}$:

$$\boldsymbol{\kappa} = \kappa \begin{pmatrix} \cos\alpha \\ \sin\alpha \\ 0 \end{pmatrix} \ .$$

The evaluation is preferably given by a two step process:

1. Bloch states $|k\rangle = |n\boldsymbol{k}\rangle$ for a given band n and all $\boldsymbol{k}_c + \vec{\Gamma\mathrm{X}}$ on the high-symmetry lines HKH and H'K'H' are determined by a tight-binding approach since the overlap of p_z orbitals of adjacent layers is small. This yields four states for each point, representing four electronic bands.

2. The $\boldsymbol{k}\cdot\hat{\boldsymbol{\pi}}$ method is applied to wavevectors slightly off the high symmetry lines by rewriting the stationary Schrödinger equation $\hat{H}\,|k\rangle = E_k\,|k\rangle$ for the Bloch factors u_k including the

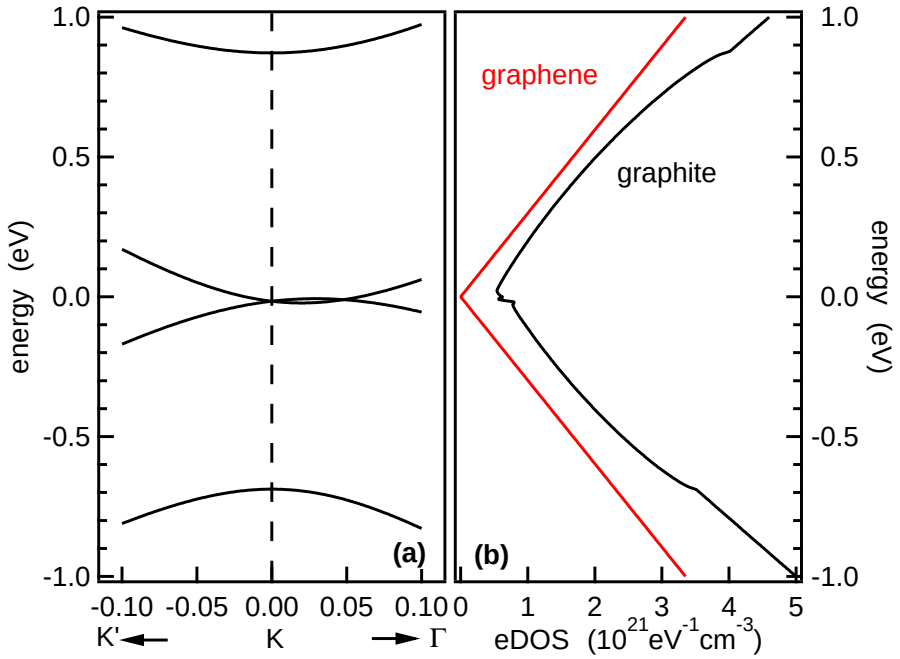

Figure 3.4: *(a) Calculated band structure of graphite by using the SWM model around the K point of the BZ. (b) Resulting eDOS together with the linear eDOS of graphene (red).*

single-electron potential V_e as [PL91]:

$$\left(\frac{(\hat{\boldsymbol{\pi}} + \hbar \boldsymbol{k})^2}{2m} + V_e \right) u_k = E_k u_k \ .$$

By neglecting quadratic effects in $\boldsymbol{\kappa}$ the hamiltonian becomes

$$\hat{H}_{\boldsymbol{k}} = \hat{H}_{\boldsymbol{k}_c + \Gamma\vec{\mathrm{X}}} + \frac{\hbar}{m} \boldsymbol{\kappa} \cdot \hat{\boldsymbol{\pi}} \ . \tag{3.2}$$

In the basis of tight-binding states $| \ \boldsymbol{k}_c + \Gamma\vec{\mathrm{X}}, 1 \ \rangle, \ldots, | \ \boldsymbol{k}_c + \Gamma\vec{\mathrm{X}}, 4 \ \rangle$ this results in the SMW hamiltonian

$$\hat{H}_{\boldsymbol{k}} = \begin{pmatrix} E_1 & & & \\ & E_2 & & \\ & & E_3 & \\ & & & E_4 \end{pmatrix} + \underbrace{\frac{\sqrt{3}}{2} a_0 \kappa}_{\sigma} \begin{pmatrix} 0 & & h_{13} & h_{13}^* \\ & 0 & h_{23} & -h_{23}^* \\ h_{13} & h_{23} & 0 & h_{33} \\ h_{13} & -h_{23} & h_{33}^* & 0 \end{pmatrix} \ . \tag{3.3}$$

Its diagonalization leads to four eigenstates and four eigenenergies for each $\boldsymbol{k}$ in the vicinity of the HKH and H'K'H' lines, resulting in four bands as shown in Figure 3.4(a). The eigenenergies for the points that are exactly located on such a line, i.e. $\sigma = 0$, are found to be:

$$\left. \begin{matrix} E_1 \\ E_2 \end{matrix} \right\} = \Delta \pm 2\gamma_1 \cos(\pi\xi) \ , \qquad E_3 = \frac{1}{2}\gamma_2 \left(2\cos(\pi\xi)\right)^2 \ ,$$

where the dimensionless parameter $\xi = (k_z c_0)/(2\pi)$ has been introduced. The off-diagonal elements of the hamiltonian are given by

$$\left. \begin{matrix} h_{13} \\ h_{23} \end{matrix} \right\} = (\mp\gamma_0 + 2\gamma_4 \cos(\pi\xi)) \frac{e^{\mathrm{i}\alpha}}{\sqrt{2}} \ , \qquad h_{33} = \gamma_3 e^{\mathrm{i}\alpha} \ ,$$

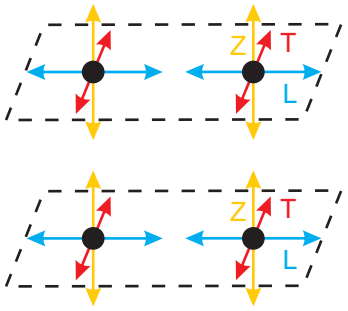

Figure 3.5: *Ionic motion of atoms in a layered material with strong intralayer but weak interlayer bonds. Here, one distinguishes out-of-plane (Z), in-plane transversal (T) and longitudinal (L) directions. According to [Por07].*

with seven phenomenological parameters $\gamma_0, \ldots, \gamma_5, \Delta$ that can be estimated from tight-binding calculations [TR82] which also elucidate their physical meanings. However, they have also been determined by fits to various experimental results [MMD80]. These values will be used here. The differences in *ab initio* calculations and experiments, presented in Table 3.2, have not yet been fully understood.

	ab initio	experiment
γ_0	2.92	3.16
γ_1	0.27	0.39
γ_2	-0.022	-0.019
γ_3	0.14	0.28
γ_4	0.10	0.044
γ_5	0.0063	0.038
Δ	-0.0079	-0.008
E_F	-0.025	-0.024

Table 3.2: *SWM parameters and Fermi energy in* eV *as results from ab initio calculations [TR82] and experiments [MMD80].*

Like in graphene, $\gamma_0 = 3.16$ eV is the interaction integral over adjacent carbon atoms from the same layer, whereas $\gamma_1 = 0.39$ eV is the interaction integral of two adjacent carbon atoms from different layers. Therefore, γ_1 is mainly responsible for the splitting of the bands that are originally degenerated in graphene. These parameters also fix the Fermi energy at $E_F = -24$ meV. Importantly, the momentum matrix elements projected on the $\boldsymbol{\kappa}$ direction, essential for the computation of the optical properties, can be obtained by comparing Equations (3.2) and (3.3). As an illustration of the SWM model, Figure 3.4 shows the band structure of graphite in the vicinity of K as well as the resulting eDOS whose smallness at the Fermi energy makes graphite a semimetal.

The SWM model is restricted to just a small region of the reciprocal space. It is accurate roughly 200 meV around E_F [TR82] near the H-K axis of the BZ and thus sufficient for application in the THz range. For IR spectroscopy, the Johnson-Dresselhaus (JD) model [JD73] is applied. It accounts for the full zone π-band and was shown to be equivalent to the SWM model along the H-K axis [TR82]. Unfortunately, the JD model is inaccurate in the region of E_F. Even though, the excitation energies in photoexcitated experiments are in the range of 1.6 eV, it turns out that electron cooling immediately leads to a chemical potential below 0.1 eV. Since THz spectroscopy is sensitive especially in the range of the Fermi level, all calculations including the band structure have been done by using the SWM model (see interDOT in Section 1.2.3).

In summary, the semi-phenomenological hamiltonian in Equation (3.3) was developed by SWM

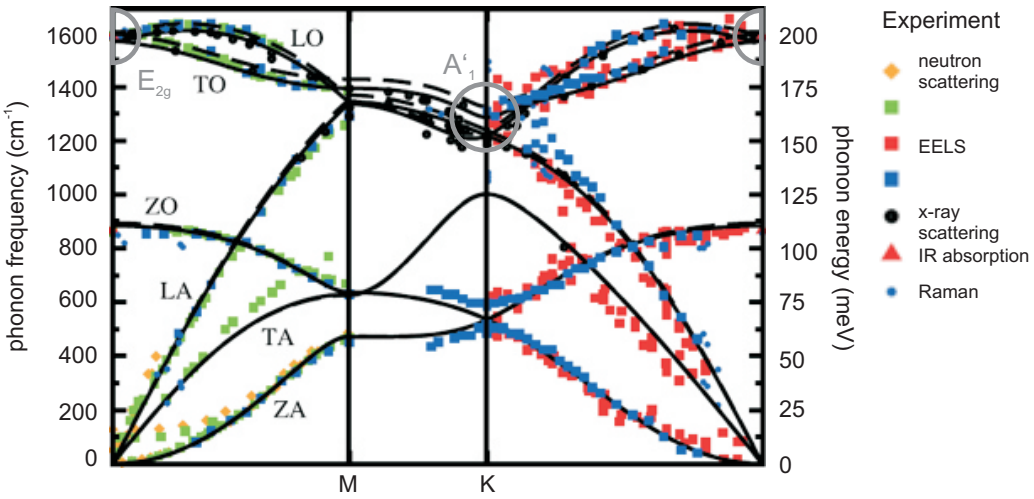

Figure 3.6: *DFT calculation of the phonon dispersion for graphite together with experimental data obtained by neutron scattering, electron energy loss spectroscopy (EELS), x-ray scattering and optical spectroscopy, taken from [WR04]. Phonon branches from low-energy ZA to highest energy LO are shown, ZA obtains the unusual q^2 dependence. Here, only acoustic branches show differences to graphene. The modes A_1' in K and E_{2g} in Γ exhibit Kohn anomalies.*

to obtain the band structure and the momentum matrix elements of graphite in the vicinity of the Fermi energy E_F including seven free parameters which have been determined by *ab initio* calculation and experimental data [DDS+88, TR82]. It will be used extensively in the following sections to model the measured dielectric function of graphite.

3.1.3 Phonon Dispersion

The layered structure of graphite also influences the ionic motion:

1. Low interlayer coupling leads to pronounced differences in the transversal phonons, i.e. in-plane and out-of-plane modes.

2. Strong sp^2-bonds lead to high energy longitudinal phonon modes.

Figure 3.5 schematically shows four atoms in two graphene layers. Here, the in-plane motion of the atoms shows high frequencies in longitudinal (L) and transversal (T) modes due to covalent bonds. The out-of-plane modes, so-called Z phonons, are softer than L and T modes, caused by the weak interlayer interaction. Additional, the ZA mode shows a q^2 dependence in the dispersion relation as a consequence of the point group symmetry of graphene [WR04]. Since the unit cell of graphite consists of four atoms, twelve phonon branches occur. For frequencies above 400 cm^{-1} (50 meV) the phonon branches are almost doubly degenerated due to the weak interlayer interaction, similar to the case of graphene. For example only a small difference of 5 cm^{-1} has been calculated for the IR-active E_{1u} mode and the Raman-active E_{2g} mode at the Γ point of the BZ. Therefore, a comparison with experimental data can be done for phonon calculations of the graphene sheet only [WR04]. Figure 3.6 shows the calculated phonon dispersion relation for graphite together with experimental data obtained by different techniques [WR04].

The E_{2g} mode and the IR-active A_1' mode at the K point of the BZ are of special interest due to their strong EPC as can be seen in Figure 3.6 from the Kohn anomalies. Since energy relaxation after photoexcitation includes electron-phonon and phonon-phonon scattering, these so-called

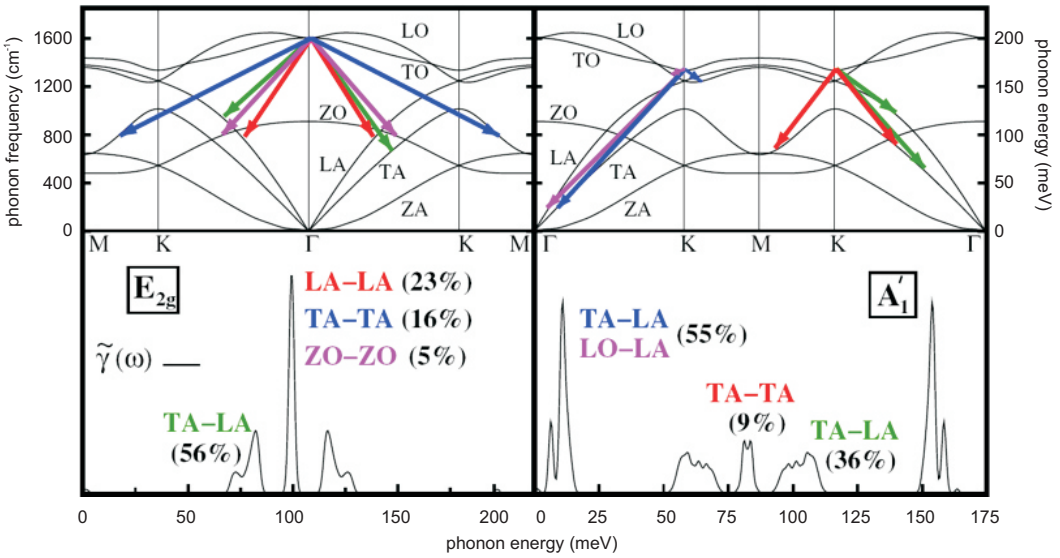

Figure 3.7: *Dispersion relation for graphene together with possible decay channels for E_{2g} phonons (left) and A_1' phonons (right). Taken from [BLMM07]. Lower panels show the probability per unit time $\tilde{\gamma}$ of these decays.*

Strongly-Coupled Optical Phonons (SCOPs) will play a crucial role in the description of the dynamics in graphite as presented in Section 3.4.

3.1.4 Electron-Phonon and Phonon-Phonon Coupling

Electrons partially screen the bare ion-ion interaction and so soften the lattice vibrations in a solid. This is usually seen by discontinuities in the phonon dispersion for phonon modes with strong EPC. Such screening only occurs for phonon wavevectors $\boldsymbol{q}$, if there are two electronic states with wavevectors $\boldsymbol{k}$ and $\boldsymbol{k}+\boldsymbol{q}$, both on the Fermi surface [Koh59, PLM+04]. In graphite, the Fermi surface restricts the in-plane component of the electronic wavevector $\Delta\boldsymbol{k}$ in the vicinity of the Γ and K points of the BZ:

$$\begin{aligned} \Delta\boldsymbol{k} &\approx \vec{\mathrm{K}}\vec{\mathrm{K}} = 0 \\ &\text{or} \\ \Delta\boldsymbol{k} &\approx \vec{\mathrm{K}}\vec{\mathrm{K}}' = \vec{\Gamma\mathrm{K}}\,. \end{aligned}$$

These electronic intrapocket and interpocket transitions are shown in Figure 3.3. Therefore, only phonon modes around the Γ and the K point and strong EPC can suffer softening. This situation is displayed in Figure 3.6, where the Γ and K phonons with the highest energy exhibit kinks in their dispersion curves. These so-called Kohn anomalies are absent for all other modes with lower phonon energy, since the matrix elements of the EPC vanish as shown by DFT calculations done for graphene [PLM+04, BLMM07]. Analytical derivation from experimental phonon slopes gives $\langle\, g_K^2 \,\rangle \approx 0.072$ eV^2 and $\langle\, g_\Gamma^2 \,\rangle \approx 0.029$ eV^2, finally stating [PLM+04]:

$$\frac{\langle\, g_K^2 \,\rangle\, \omega_K}{\langle\, g_\Gamma^2 \,\rangle\, \omega_\Gamma} = 2\,. \tag{3.4}$$

Thus, the A_1' mode in the K point show the highest EPC followed by the E_{2g} mode in the Γ point, with energies $\hbar\omega_K = 161$ meV and $\hbar\omega_\Gamma = 197$ meV, respectively.

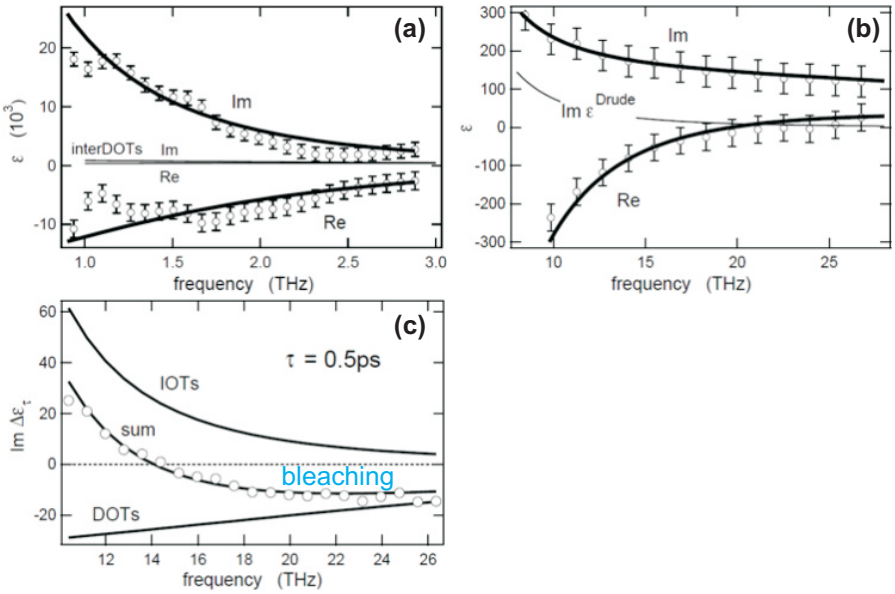

Figure 3.8: *Previously obtained results for graphite at room temperature [Kam05]. (a) Low THz range together with a Drude fit, showing the typical $1/\omega$ behavior in the imaginary part. (b) High THz range together with fit consisting of DOT and IOT contributions. Here, the Drude part alone is not sufficient to fit the data. (c) Pump-induced changes show an increase in absorption below 15 THz and a decrease above 15 THz.*

As has been mentioned previously, the dispersion relations of graphene and graphite do not show significant differences, especially at high phonon energies as found for the SCOPs. Thus, three-phonon processes are calculated using only results from graphene as has been done by [BLMM07]. Additionally, the probability of A_1'- and E_{2g}-decays with frequencies ω_0 into two other phonon modes with lower frequencies, ω and $\omega_0 - \omega$, as can be seen from Figure 3.7, has been estimated. The Γ mode decays mainly symmetrically into modes with almost the same energy, whereas the K mode decays mainly asymetrically into low-energy acoustic modes. This difference has an impact on the temperature dependence of the phonon decay because acoustic modes are in the energy range of thermal excitation. This temperature-dependence will be used in Section 3.4 to distinguish the population between different phonon modes.

3.1.5 Optical Properties

While the E_{1u} mode is IR-active, in graphite no other IR-active phonon modes have been observed in the far- and mid-IR [Pal91]. This behavior is explained by a very small static dipole moment of the nonpolar graphite lattice in contrast to ionic crystals. This situation corresponds to a Lorentz oscillator where the particles that interact with the light have a very small charge.

In graphite, the optical properties in the infrared and visible part of the light spectrum are dominated by electronic transitions. As has been shown in Section 1.2.3, a Bloch electron can either absorb a photon by a DOT or by an IOT. It has been found that

- IOTs dominate the optical absorption in the far-IR,
- both IOTs and DOTs are important in the MIR [Kam05], and
- DOTs dominate in the NIR and visible range of the light spectrum.

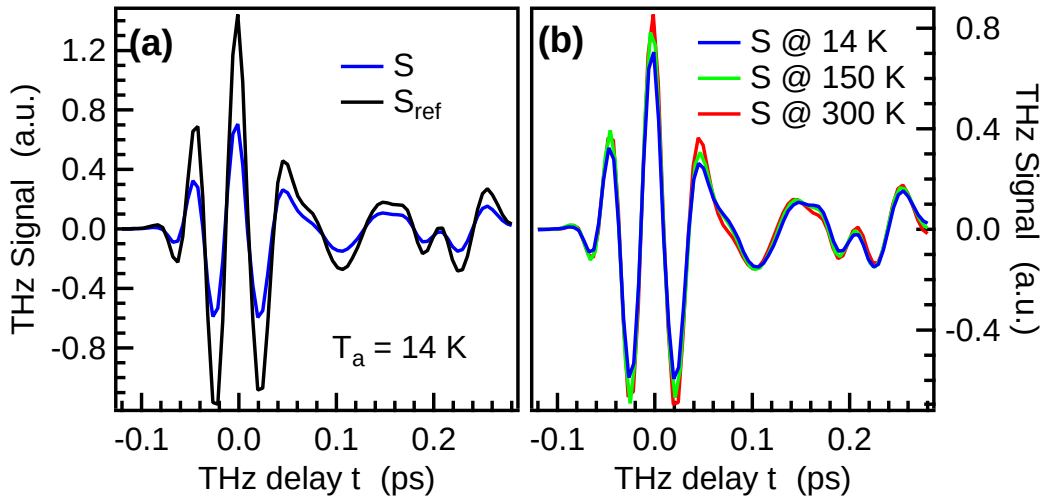

Figure 3.9: *THz waveforms taken from graphite at equilibrium conditions: (a) THz signal S measured after transmission of the graphite sample together with the reference signal S_{ref} from the diamond substrate. (b) THz signal for three different sample temperatures. Here, a decrease in absorption with temperature is observed.*

Low-energy excitations in graphite at room temperature have been studied in detail by [Kam05]. Information on the thermalization process including interaction of electrons and phonons is provided by investigation of the temperature domain. Thus, the previously used experimental setup has been extended to temperature dependent measurements. It will turn out that conclusions can be drawn for electron-electron, electron-phonon and also phonon-phonon scattering in graphite at equilibrium conditions and after photoexcitation in the temperature regime. Thus, the main results from [Kam05] shall be presented here briefly.

For $T_a = 300$ K the Drude response dominates in the low THz frequency range (1-3 THz)(Figure 3.8(a)) and the interDOT part is negligible. For 8-27 THz, the interDOT part must be included to reproduce the measured data, as presented in Figure 3.8(b).

In the case of photoexcited graphite, pump-induced changes in the dielectric function $\Delta\varepsilon_\tau$ show a bleaching effect for frequencies higher than 15 THz as can be seen from the negative absorption part as given by $\mathrm{Im}\,\Delta\varepsilon$ in Figure 3.8(c). The dynamics has been found as follows:

1. Pump pulses excite electrons from the valence to the conduction band via DOTs [SCK$^+$90].
2. Within 0.5 ps, the electronic system thermalizes and concurrently the electrons transfer most of their excess energy to the SCOP modes [KPS$^+$05, YSM$^+$09, BRE09, ITY$^+$11, MGF$^+$01, BMH$^+$07]. A quasi-equilibrium of electrons and SCOPs is established.
3. The hot SCOPs scatter with cold phonons on a picosecond timescale [IHK$^+$08, CYS$^+$11].

From these results, several questions arise, which should be answered by temperature dependent THz experiments:

- The slope of graphite's eDOS should lead to a temperature dependence of DOT and IOT contributions. How does this affect absorption and dispersion?
- What impact does temperature have on the bleaching found in photoexcited graphite?
- Does graphite act as a semiconductor after photoexcitation with a different distribution of electrons and holes or is it still found to be metallic?

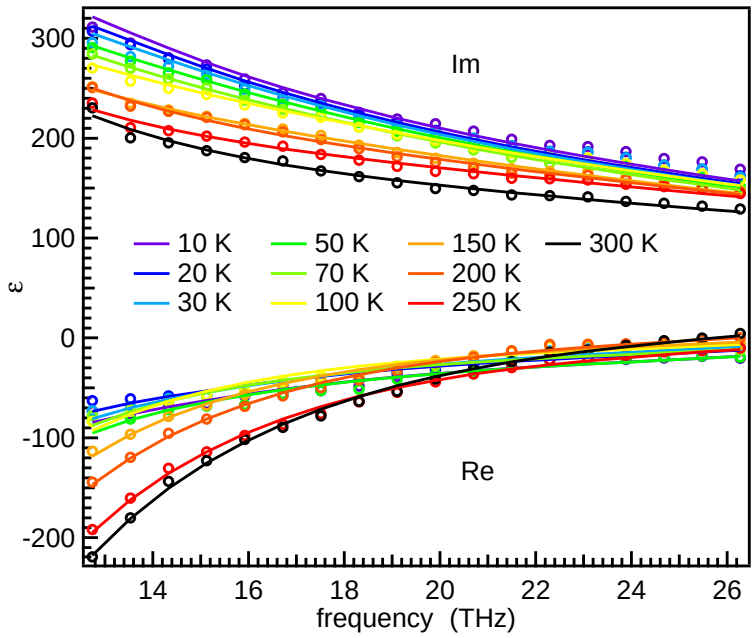

Figure 3.10: *Obtained real and imaginary part of the dielectric function $\varepsilon(\omega)$ for various sample temperatures T_a (circles) together with fits obtained by the model mentioned in the text (solid lines). The imaginary part, representing the absorption site, shows a decrease with temperature, while the real part, representing the phase information, shows a more sophisticated behavior.*

- Which phonons are invoked in phonon cooling after photoexcitation, K or Γ modes?

3.2 Graphite at Equilibrium Conditions

Because of its changing eDOS in the vicinity of E_F, there should be a significant temperature-dependence of the optical properties of graphite. The investigation of graphite under equilibrium conditions requires measurements of the sample response after THz transmission without photoexciation. Thus, the measured data from an unperturbed graphite sample shall be presented. Here, a significant change in transmission is observed, which will be understood in terms of low-energy optical transition by applying the model from Section 1.2.3. Then, the focus will be on the plasma frequency and its connection to the electronic properties of graphite.

3.2.1 Experimental Data

Raw Data

THz-transmission experiments on graphite have been performed varying the sample temperature and measuring each time sample and reference as described in detail in Section 2.3.1. Figure 3.9(a) shows the transmitted THz electric field for sample and reference. The graphite sample absorbs more than 50 % of the incident THz field E^{inc} with respect to the substrate. Here, the sample thickness has been chosen appropriately and measured as presented in Appendix B.

Figure 3.9(b) shows the transmission through unexcited graphite for three different temperatures T_a in the range from 14 K up to 300 K. A large increase in amplitude of about 20 % with temperature is seen from the data. This decrease in absorption with increasing temperature should also

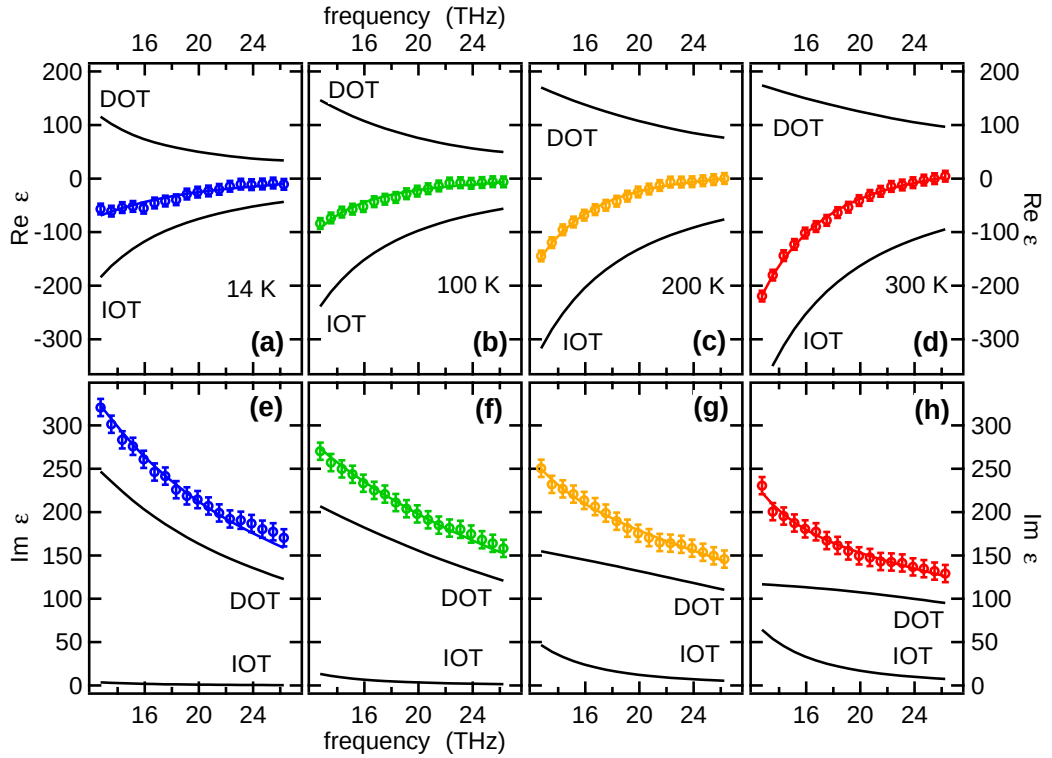

Figure 3.11: *(a) - (d) Real and (e) - (h) imaginary part of the dielectric function (circles) for four different sample temperatures T_a between 14 K and 300 K together with fits (colored solid lines) obtained by the model mentioned in the text. Contributions of DOTs and IOTs to the absorption (black solid lines) show opposite temperature dependences: while DOTs decrease with temperature, an increase of IOTs is observed.*

affect the imaginary part of the dielectric function.

Temperature dependent measurements have been performed in a frequency range between 12 and 27 THz, hence it is not necessary to perform additional measurements at low THz frequencies for the following reasons:

- data evaluation has shown that data measured at higher frequencies are also sufficient to extract all fit parameter values including ω_{pl} and Γ;
- the focus is on the interDOT contribution ($1/\omega^2$ scaling), so the Drude contribution ($1/\omega^3$ scaling) should be as small as possible.

Dielectric Function

Applying the formalism introduced in Section 2.3.3 to extract the dielectric function results in $\varepsilon(\omega, T_a)$ as shown in Figure 3.10 for different temperatures T_a. Here, the imaginary part Im $\varepsilon(\omega, T_a)$ shows a strong decrease with T_a, representing the higher transmission through the sample that has been found in the raw data. Additionally, the real part exhibits a strong temperature dependence: the absolute value increases with T_a.

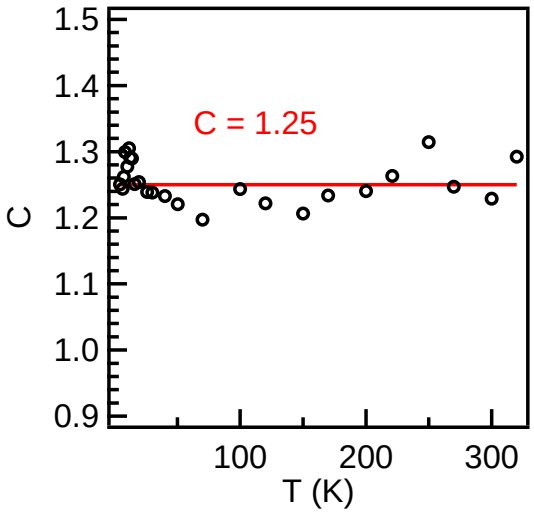

Figure 3.12: *Measured values for the temperature dependence of the scaling factor C. Circles represent measured values. The solid line represents the constant value $C = 1.25$ as has been used in the data evaluation process.*

3.2.2 Modeling of the Dielectric Function

Fits to the dielectric function

Here, the measured $\varepsilon(\omega, T_a)$ is fitted by using a model including direct and indirect optical transitions. The different contributions to the used model have been presented in Section 1.2.3, combining Drude free carrier response and linear response formalism as given by the Kubo formula (1.23) to account for the electronic interband transitions. Information on the transition matrix elements is provided by the SWM model, introduced in Section 3.1.2. Altogether, the applied model to fit the measured dielectric function is given by:

$$\varepsilon^{\mathrm{fit}}(\omega, T_a) = C \cdot \left[\varepsilon^{\mathrm{Drude}}(\omega_{\mathrm{pl}}, \Gamma) + \varepsilon^{\mathrm{interDOT}}(T_e) + \varepsilon_\infty\right] \ . \tag{3.5}$$

Here, three additional fit parameters appear beside ω_{pl} Γ: the electronic temperature T_e as originated in the Fermi distribution function in the interDOT part, a scaling factor C and a real offset ε_∞, including optical transitions with resonances outside the frequency window. This is the same approach in principle as presented by [Kam05], in this case applied for various sample temperatures T_a between 10 K and 320 K. An important change concerning the scaling factor C has been introduced: here, C accounts for uncertainties in the sample thickness due to the refractive index (see appendix B) and slight changes in the sample or reference position during the measurement process, possibly leading to slight changes in sample or reference thicknesses. It is found to be constant as seen from Figure 3.12, indicating that the sample thickness is larger than estimated from the optical transmission. Thus, it is set to be $C = 1.25$ in the following.

Besides the measured temperature-dependent dielectric function, Figure 3.11 presents the resulting fits to the data together with DOT and IOT contributions. The imaginary part in the considered frequency window cannot be described by the Drude part alone. At room temperature, DOT and IOT contributions are in the same order of magnitude, whereas at low temperatures DOT contributions dominate. Both show a strong but directly opposed temperature dependence. By this, the observed bleaching is explained by means of the temperature broadening of the Fermi distribution within the Kubo formalism, as schematically displayed in Figure 3.13. A higher temperature leads to more populated states above E_F and less states to scatter in. In other words, it is less likely for an electron to absorb a THz photon at higher temperatures, since there is a lower probability for DOTs. In contrast, the IOT contribution increases with temperature due to a higher population of phonon modes. This should affect the scattering rate Γ, leading to more scattering events. In addition, thermally excited electrons account for the plasma frequency ω_{pl} and should here result in an increase of ω_{pl} with temperature.

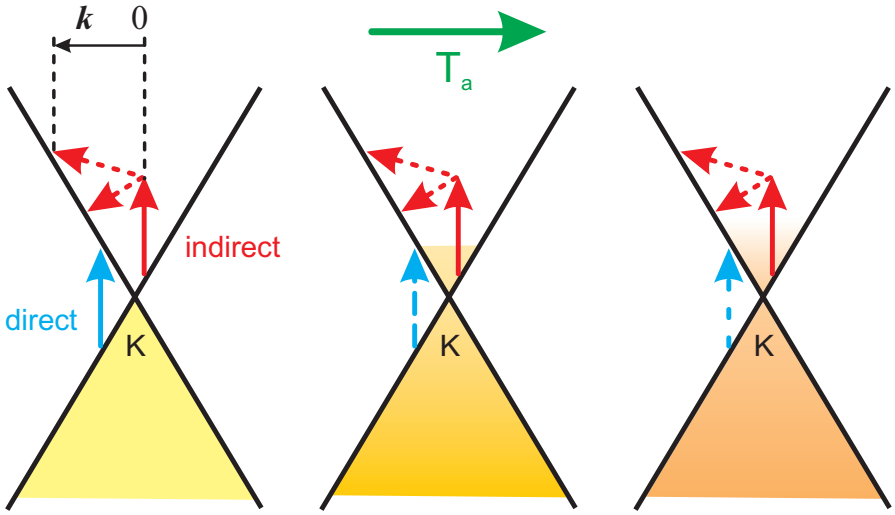

Figure 3.13: *Schematic of the thermal excitation around the K point. With increasing temperature states above the Fermi energy are populated resulting in blocked DOTs but also more scattering partners and thus more IOTs.*

Finally, the temperature dependence of the real part is considered. While the absolute value of Im ε decreases with increasing T_a, the opposite behavior is the case for Re ε. Here, absolute values of DOT and IOT contributions increase with temperature, whereupon the IOT parts are negative. Since both parts contribute to the applied model, the additional measurement of Re ε is of importance.

Temperature-dependence of the fit parameters

Besides the constant scaling factor C, fits to the dielectric function include four fit parameters with physical meaning. They are displayed in Figure 3.14 and will be discussed below. Table 3.3 presents the values for sample temperatures T_a also measured for photoexcited graphite:

T_a (K)	T_e (K)	$\hbar\omega_{\mathrm{pl}}$ (eV)	Γ (THz)	ε_∞
14	14.3	0.64	2.0	21
50	50.7	0.69	3.3	22
100	100.5	0.73	5.6	23
150	150.4	0.79	5.7	23
200	200.5	0.85	14.2	27
250	249.5	0.90	15.1	20
300	300.5	0.94	15.3	33

Table 3.3: *Obtained values of the parameters for chosen sample temperatures and* $C = 1.25$.

The real offset is found to be a constant $\varepsilon_\infty = 22\pm8$, as can be seen from Figure 3.14(b). Differences between the values previously presented [Kam05, vV09] and the actual ones, have their origin in a different meaning of the scaling factor C. For all measured sample temperatures $T_e = T_a$ holds, as shown in Figure 3.14(a). This result seems to be reasonable, since THz pulses only have small excitation energies and should not lead to significant changes in the electronic distribution.

Figures 3.14(c) and (d) present the temperature dependence of the plasma frequency ω_{pl} and

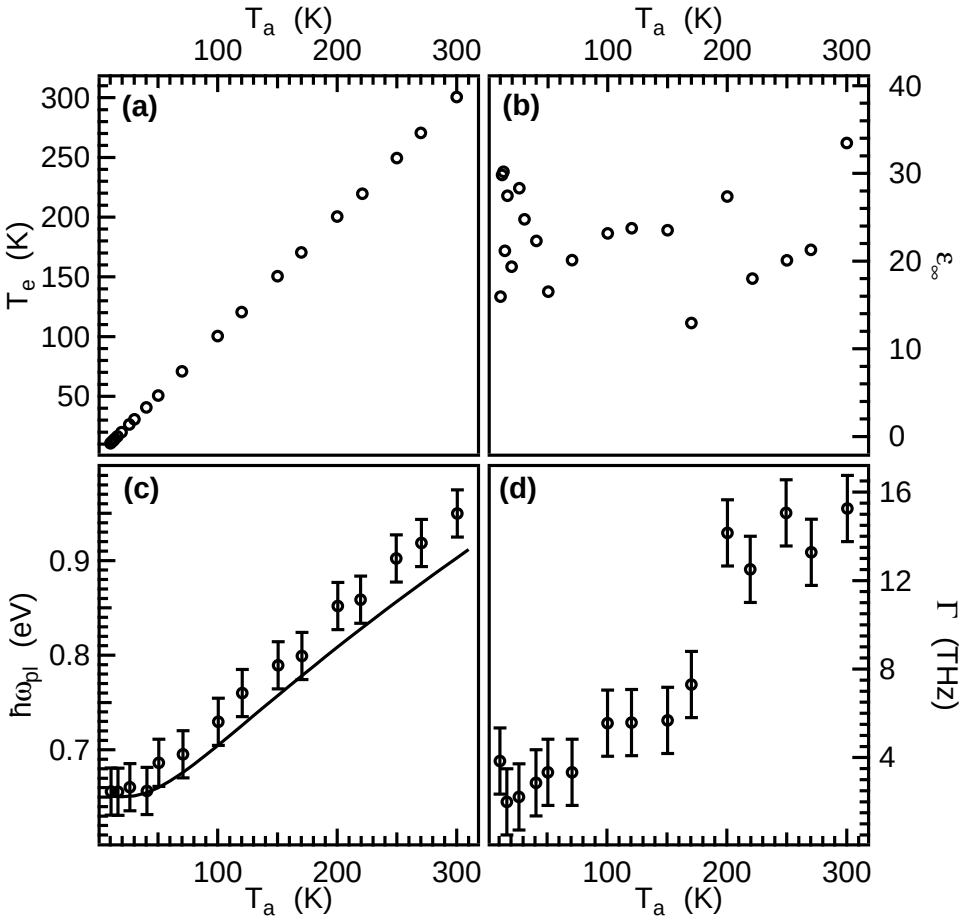

Figure 3.14: *Temperature dependence of the parameters obtained by fitting the measured data to the model. (a) electronic temperature T_e, (b) real offset ε_∞, (c) plasma frequency in terms of energy $\hbar\omega_{\mathrm{pl}}$ together with the model based on the eDOS from Equation (3.6), (d) Drude scattering rate Γ.*

the Drude scattering rate Γ. An increase with temperature is observed that accounts for the temperature dependence of the IOT contribution to the imaginary part of the dielectric function.

The curve of $\hbar\omega_{\mathrm{pl}}(T)$ can be modeled by using the free-carrier plasma frequency from Equation (1.20) and the velocity-weighted eDOS:

$$\omega_{\mathrm{pl}}^2 = -\frac{8\pi e^2}{V}\int \mathrm{d}\epsilon \frac{\partial f}{\partial \epsilon} v^2 D(\epsilon)\,. \tag{3.6}$$

It should be emphazied that the measured ω_{pl} mainly results from fits of the Drude part $\varepsilon^{\mathrm{Drude}}$ to the dielectric function, whereas the model given by Equation (3.6) originates in the band structure provided by the SWM model that was previously used to fit the interDOT contribution $\varepsilon^{\mathrm{interDOT}}$. Thus, the temperature dependence can be understood considering the electronic bands in graphite and its consequences for the eDOS. The linear increase is due to the quasi-linear eDOS around E_F while the plateau below 50 K can be ascribed to the nonvanishing eDOS at E_F as displayed in Figure 3.4. Here, measurements for graphene should reveal a significant difference because of its zero eDOS at E_F.

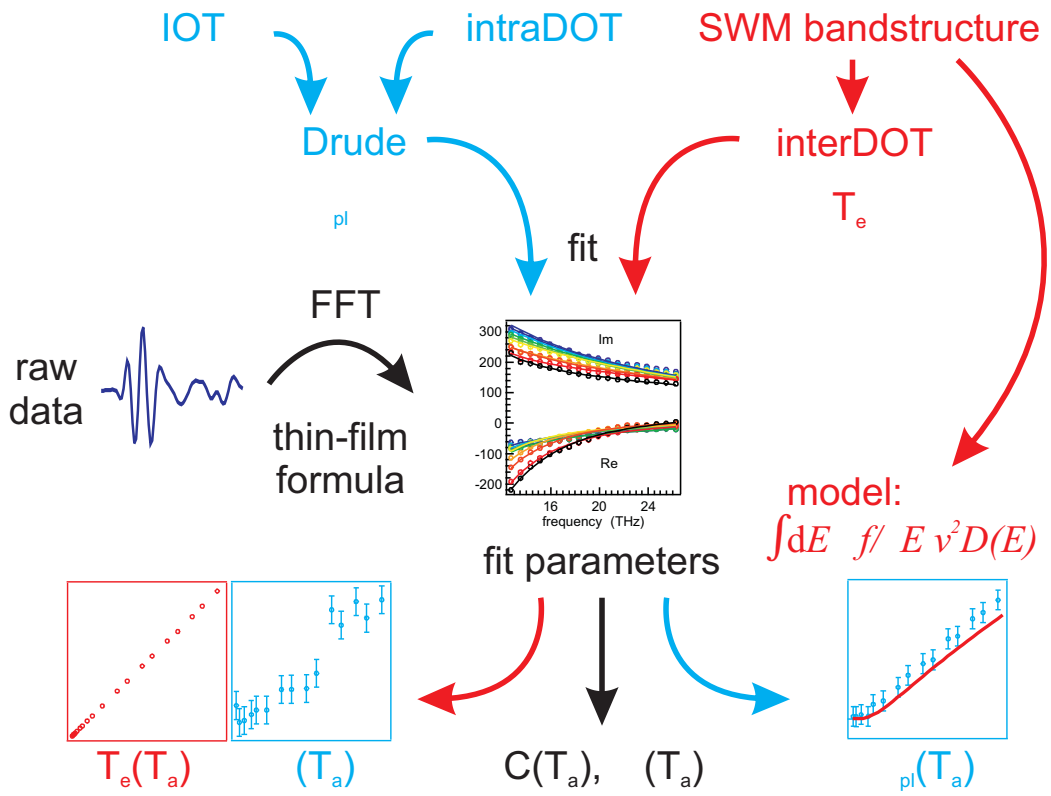

Figure 3.15: *Schematic of the data evaluation for graphite under equilibrium conditions. Starting from the raw data, the dielectric function is evaluated and fitted including IOTs, intraDOTs and interDOTs. Five fit parameters are involved. While C and ε_∞ are found to be constant, T_e, Γ and ω_{pl} show a temperature dependence. A model including SWM band structure information is in agreement with the fitted ω_{pl}.*

In the case of the Drude scattering rate Γ, in principle a theoretical solution according to Equation (1.25) could be obtained. Here, matrix elements for electron-impurity and electron-phonon scattering in combination with excitations by photons in the THz range have to be included. *Ab initio* calculations would be necessary to handle this in a quantitative way. However, this has been done in the case of photoexcited graphite. Here, a qualitative understanding should be emphasized: at higher temperatures more phonon modes and more electronic states above E_F are populated. Thus, electron-phonon scattering should occur more often, leading to an increase in the scattering rate. Since impurities are not temperature dependent, they should have minor influence on the temperature dependence of Γ.

3.2.3 Summary of Equilibrium Properties

An increase in the MIR transmission of thin graphite films at higher temperatures is observed, which can be explained by means of an interplay between indirect and direct optical transitions. At higher temperatures more DOTs are blocked, which results in a bleaching for radiation at THz frequencies. A temperature dependence observed for the IOTs results from the temperature dependence of plasma frequency and Drude scattering rate. A consequence of the interplay of DOTs and IOTs is the opposite temperature dependence of real and imaginary parts of $\varepsilon(\omega, T_a)$. While the absolute value of Re ε increases with temperature, Im ε decreases. Additionally, an intuitive description of the plasma frequency is provided by means of the eDOS of graphite.

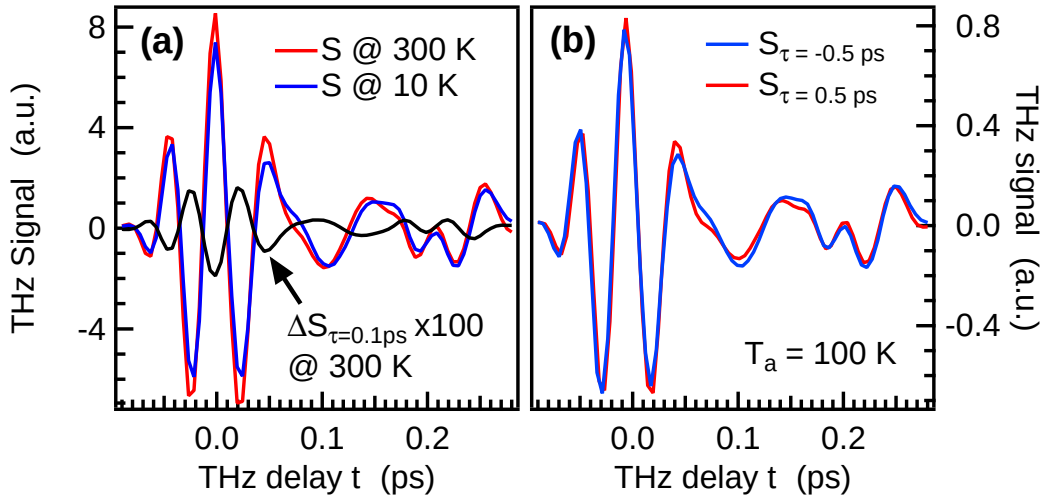

Figure 3.16: *Raw data of pump-probe experiments. (a) Pump-induced changes to the THz signal* $100 \times \Delta S_\tau$ *for* $\tau = 0.1$ *ps after excitation at room temperature together with unperturbed data* S *for two different sample temperatures showing absorption changes. (b) THz transient* S_τ *prior and after photoexcitation with pump-probe delays* $\tau = \pm 0.5$ *ps at a sample temperature of 100 K also showing changes in absorption.*

The data evaluation scheme is provided by Figure 3.15. From the THz transient, the dielectric function has been extracted and then fitted with respect to IOT and DOT contributions. The obtained fit parameters show a temperature dependence that can be modeled in the case of the plasma frequency using the calculated band structure. Attention has also been paid to uncertainties in the sample thickness by introducing a scaling factor C.

3.3 Photoexcited Graphite

In this section, this view is extended to photoexcited graphite. For this, the dependence on the sample temperature for various delays τ is investigated. Previous measurements focused only on $T_a = 300$ K [Kam05]. The structure of this section is as follows: as in the case of graphite under equilibrium conditions, raw data are presented before the pump-induced changes in the dielectric function are modeled in terms of optical transitions. In addition, the dependence on different distribution functions for electrons and holes to the interDOT contribution is discussed. Special interest is paid on the dynamics of the fit parameters, since it allows an interpretation in terms of electron-phonon and phonon-phonon interaction. Finally, a reasonable scenario for the charge-carrier dynamics after photoexcitation of graphite is proposed.

3.3.1 Experimental Data

Raw Data

Figure 3.16(a) shows the unperturbed THz signal $S(T_a)$ at two different sample temperatures T_a together with the pump-induced changes in the signal $\Delta S_{\tau=0.1\text{ ps}}(300\text{ K})$ at room temperature immediately after photoexcitation. Since photoinduced changes are small compared to the transmitted signal (note the factor $\times 100$), lock-in technique has necessarily been used. Figure 3.16(b) shows transmitted THz waveforms for two pump-probe delays τ before and after photoexcitation at a sample temperature $T_a = 100$ K. Again, the smallness of the changes can be seen. Here, a change in amplitude is observed which is similar to the equilibrium case. So, by

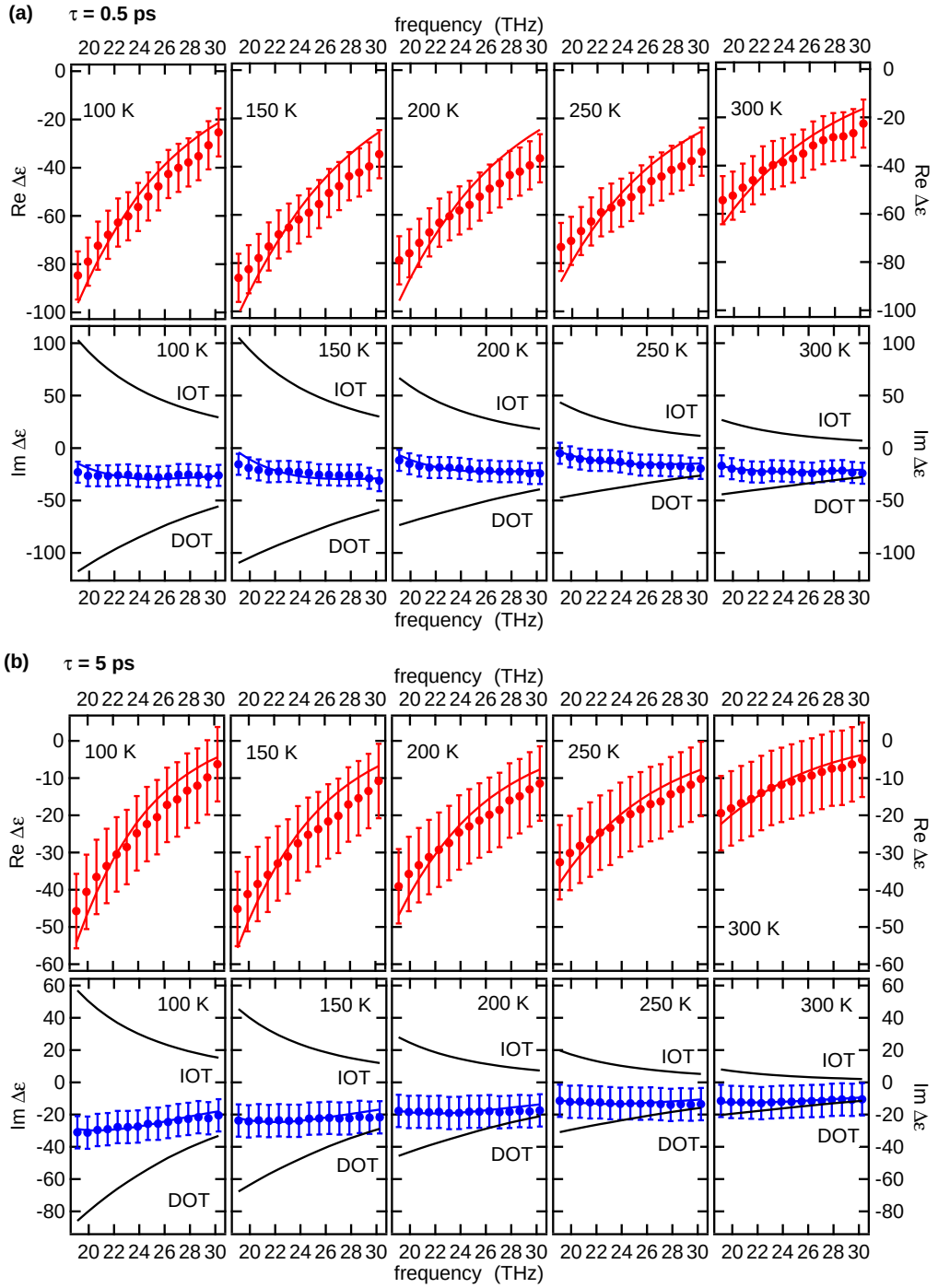

Figure 3.17: *Pump-induced changes of the dielectric function $\Delta\varepsilon_\tau(\omega)$ for various sample temperatures between $T_a = 100$ K and $T_a = 300$ K for two different pump-probe delays (a) $\tau = 0.5$ ps and (b) $\tau = 5$ ps, respectively. Circles represent data, solid lines fits to the model mentioned in the text. Black solid lines represent DOT and IOT contributions. Subpanels distinguish real (red) and imaginary parts (blue) of $\Delta\varepsilon_\tau(\omega)$. (a) Immediately after photoexcitation, Re $\Delta\varepsilon$ shows a temperature dependence, while Im $\Delta\varepsilon$ is virtually unchanged. (b) At later delays also Im $\Delta\varepsilon$ shows a temperature dependence. Here, the interplay of DOT and IOT contributions is important.*

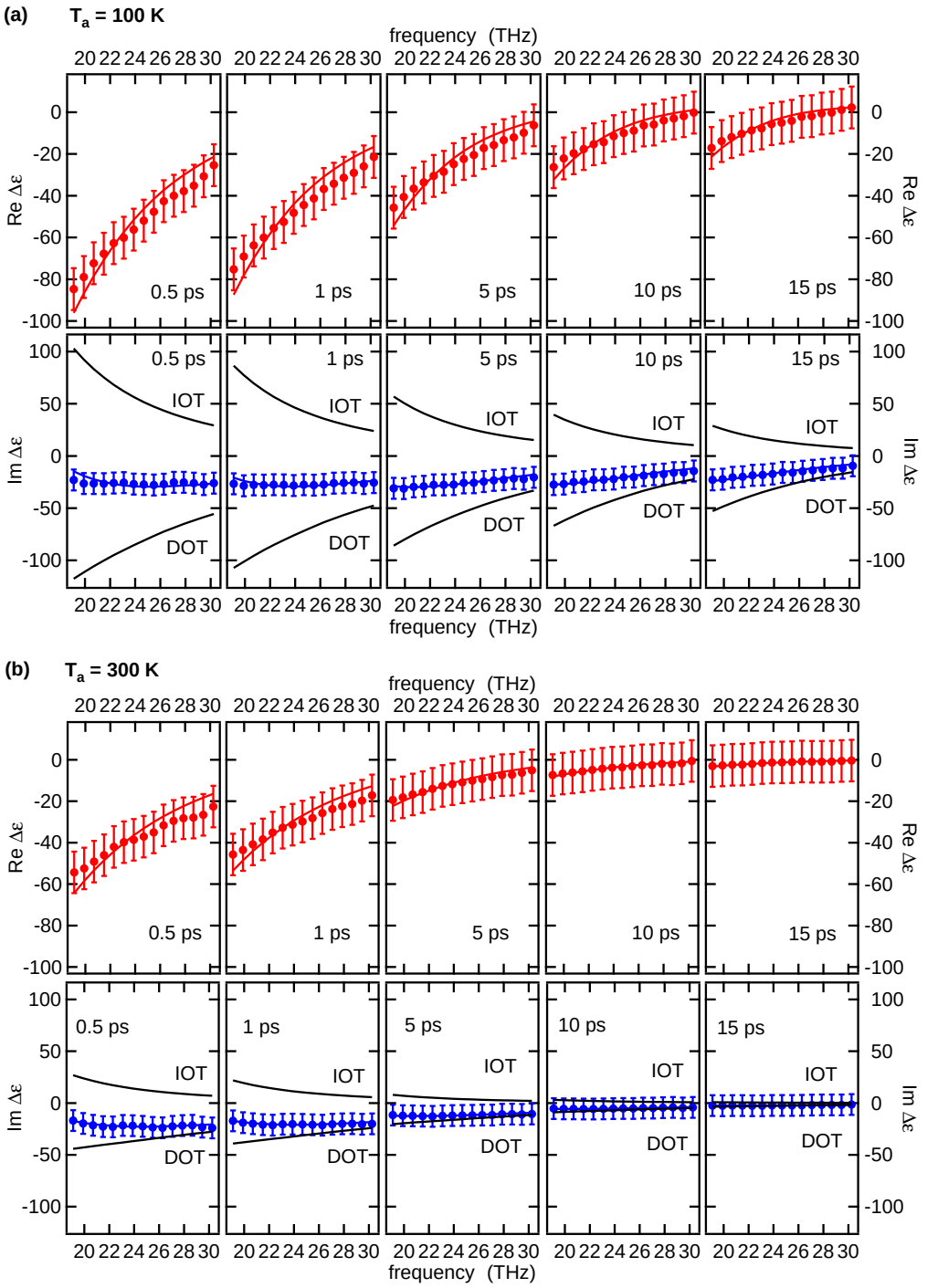

Figure 3.18: *Pump-induced changes of the dielectric function $\Delta\varepsilon_\tau(\omega)$ for different pump-probe delays between $\tau = 0.5$ ps and $\tau = 15$ ps at sample temperatures (a) $T_a = 100$ K and (b) $T_a = 300$ K, respectively. Circles represent data, solid lines fits obtained by the model mentioned in the text. Additionally, DOT and IOT contributions to Im $\Delta\varepsilon$ are shown (black solid lines). Here, measurements for both temperatures show a relaxation of the system. A faster decay is observed at higher temperatures T_a.*

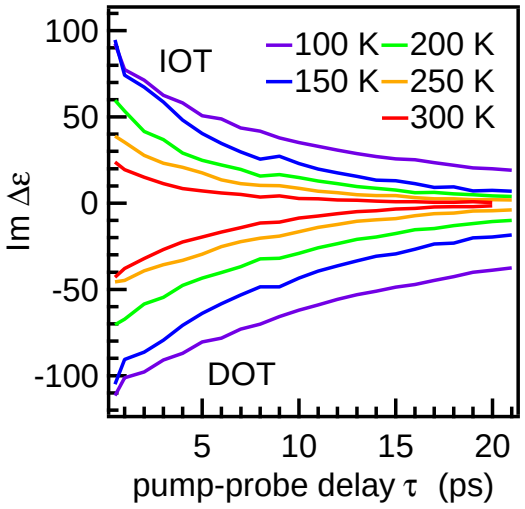

Figure 3.19: *Summary of the DOT and IOT contributions to the fitted Im $\Delta\varepsilon_\tau(T_a)$ from Figures 3.17 and 3.18. The dependence on the sample temperature T_a as a function of pump-probe delay is shown: at lower temperatures, pump-induced changes are significantly larger while at higher temperatures there is a shorter decay time.*

comparison of panels (a) and (b) of Figure 3.16 it can be seen that heating and photoexcitation lead to a bleaching of the graphite sample at THz frequencies. Thus, a negative absorption part Im $\Delta\varepsilon_\tau(\omega)$ is expected. Though changes in phase are quite small and similar to the equilibrium case, no conclusion concerning Re $\Delta\varepsilon_\tau(\omega)$ can be drawn from raw data.

Extracted Dielectric Function

Figure 3.17 shows the photo-induced changes in the dielectric function $\Delta\varepsilon_\tau(\omega)$ for different sample temperatures T_a between 100 K and 300 K and two different pump-probe delays τ, 0.5 ps and 5 ps after excitation in panels (a) and (b), respectively. These graphs are obtained by applying Equation (2.10) to the raw data in combination with equilibrium data from Section 3.2. To distinguish real and imaginary parts, they are shown separately in subpanels. Here, the error bars are a result of a statistical error from repeated measurements.

Lower subpanels present data for Im $\Delta\varepsilon_\tau(\omega)$. Since the imaginary part of the photoinduced changes of the dielectric function is negative for frequencies above 15 THz, a decreased absorption in agreement with [KPS$^+$05] is observed, as was found in the raw data. An increase of absorption below 15 THz leading to a positive Im $\Delta\varepsilon$ has been found previously. This has been explained by electronic transitions in graphite [Phi77,KPS$^+$05]. Consequences of the modeling in the frequency range above 15 THz will be discussed in detail in Section 3.3.2 by using DOT and IOT contributions.

Upper subpanels show the importance of the phase information as accessible by electro-optic sampling: Im $\Delta\varepsilon_\tau(\omega)$ remains virtually constant, whereas Re $\Delta\varepsilon_\tau(\omega)$ undergoes significant changes. Here, in contrast to the equilbrium case, the changes in Re ε are negative after photoexcitation. This will also affect the fit parameters.

Figure 3.17 also shows the dependence of $\Delta\varepsilon_\tau$ on the sample temperature T_a for each pump-probe delay. Take for example $\tau = 0.5$ ps: with increasing sample temperature T_a, the pump-induced changes in Re $\Delta\varepsilon_{0.5\text{ ps}}(\omega)$ decrease by a factor of 2, whereas Im $\Delta\varepsilon_{0.5\text{ ps}}(\omega)$ undergoes virtually no changes. For pump-probe delay $\tau = 5$ ps after photoexcitation, the imaginary part additionally shows significant changes with sample temperature as can be seen from the lower subpanels in Figure 3.17(b). This different dynamics for different T_a will be explained in terms of DOTs and IOTs.

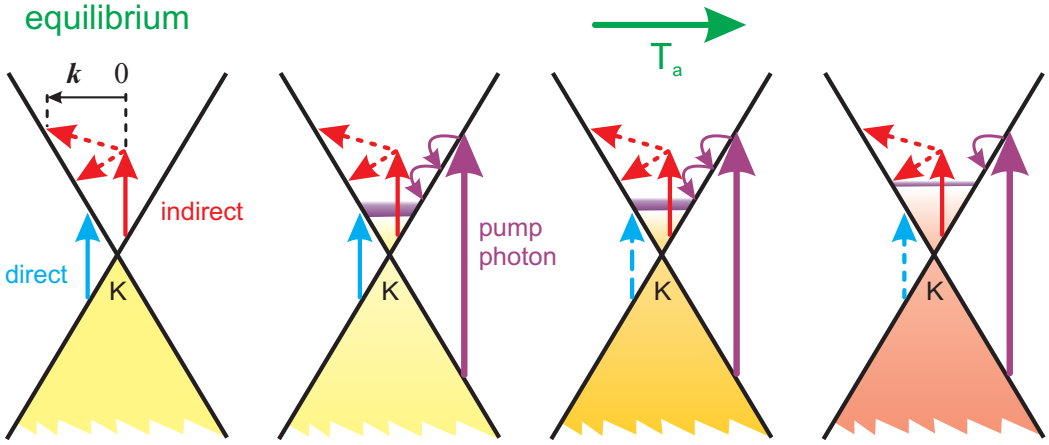

Figure 3.20: *Schematic of thermal and photoinduced excitations around the K point. With increasing temperature T_a states above the Fermi energy are populated. A pump pulse excites additional electrons from the valence into the conduction band. DOTs are blocked by thermally and photoexcited electrons. At high T_a, thermally excited electrons dominate the DOT blocking.*

In addition to the dependence of T_a, dynamics can be seen from the dependence of the pump-probe delay τ to each T_a. This is shown in Figure 3.18 for two different sample temperatures, $T_a = 100$ K and $T_a = 300$ K, respectively, in panels (a) and (b). In principle, the same behavior occurs at both temperatures, leading to smaller changes in both parts of $\Delta\varepsilon_\tau(\omega)$ at later delays τ. This can be understood in terms of energy relaxation in the system and will be discussed in Section 3.3.3.

3.3.2 Modeling of the Changes in the Dielectric Function

Fit Model

The dielectric function including DOT and IOT contributions has been modeled with an interpretation in analogy to the equilibrium case: an electron absorbs a photon via a DOT which conserves the electronic wave vector $\boldsymbol{k}$ or via an IOT which requires a change in the wavevector $\boldsymbol{\Delta k}$. Such a change is provided by scattering with phonons or other electrons. Excited electrons, transferred from the valence to the conduction band, then thermalize. The resulting electron-hole pairs block further DOTs in the range of $k_B T_e$ around E_F, leading to a decreased absorption [SCK+90,KPS+05]. As a counterpart, the higher electronic temperature T_e enables additional IOTs, resulting in an increased absorption [Phi77]. Thus, the changes in the dielectric function are fitted using:

$$\Delta\varepsilon_\tau = \varepsilon_\tau\left(T_e, \omega_{\mathrm{pl}}, \Gamma\right) - \varepsilon\left(T_a, \omega_{\mathrm{pl}}(T_a), \Gamma(T_a)\right) \ , \tag{3.7}$$

by including values from Table 3.3. Here, the difference between the pump-induced dielectric function $\varepsilon_\tau(T_a)$ and ε for the equilibrium case (Figures 3.16(b) and 3.11) for the corresponding sample temperature $\varepsilon(T_a)$ leads to the fit function of $\Delta\varepsilon_\tau$. The values C and ε_∞ are fixed as results from equilibrium measurements.

The interDOT part is highly sensitive to the charge-carrier dynamics due to the included T_e. As previously mentioned, DOT and IOT contributions are of comparable strength in the frequency range from 10-30 THz, whereas at frequencies below 5 THz the Drude part dominates and T_e has nearly no influence. Thus, fits are applied to frequencies in the range from 19 to 30 THz.

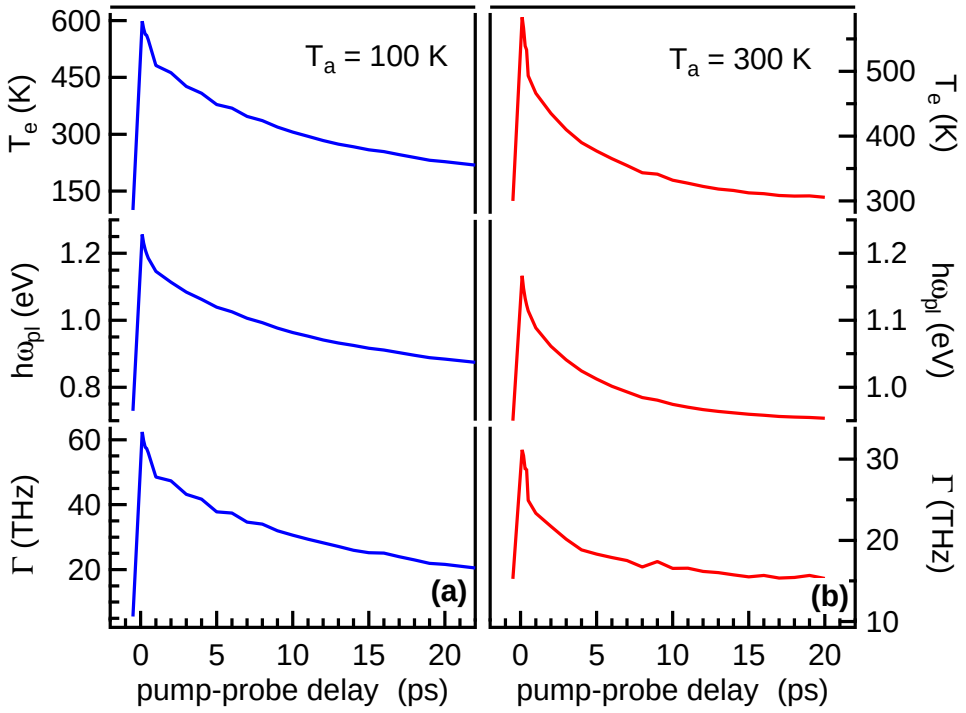

Figure 3.21: *Dynamics of the fit parameters T_e, ω_{pl} and Γ for two sample temperatures T_a. Qualitatively two components are distinguishable from the curves: a fast one immediately after photoexcitation and a slower one on a picosecond timescale. For higher temperatures, the slower component shows a faster decay.*

Fit Results

Figures 3.17 and 3.18 present fits to the measured $\Delta\varepsilon_\tau$ together with DOT and IOT contributions as obtained by using Equation (3.7). The obtained contributions to Im $\Delta\varepsilon$ of DOTs and IOTs are displayed in Figure 3.19 in its dependences on different sample temperatures T_a as well as different pump-probe delays τ.

In the frequency range above 15 THz photoexcitation results in a bleaching. This can now be traced back to the DOT contribution, as shown in Figure 3.19. Immediately after photoexcitation, thermalized electrons block states above E_F as is schematically shown in Figure 3.20. Therefore, the possibility for further DOTs is decreased, leading to a decreased absorption. This decrease of DOTs is not compensated by the increased IOT contribution resulting from more excited carriers.

This interpretation additionally explains the T_a-dependence, as found in Figure 3.20. The pump-induced changes in the DOT and IOT contributions decrease with increasing sample temperature T_a. As previously seen for the equilibrium case in Figures 3.11 and 3.14, DOTs are blocked with increasing T_a due to more thermally excited electrons, leading directly to a decreased absorption. In contrast, the IOTs increase due to more scattering partners. Since at higher temperatures electrons are already excited and states to scatter in blocked, the pump-induced changes should be smaller. The same accounts for the IOTs. Scattering partners are still excited. Further excitation results in smaller changes only. Therefore, the totally pump-induced changes $\Delta\varepsilon_\tau(\omega)$ decrease with increasing sample temperature. A temporal evolution is found in the dependence from the pump-probe delay τ and will be discussed below.

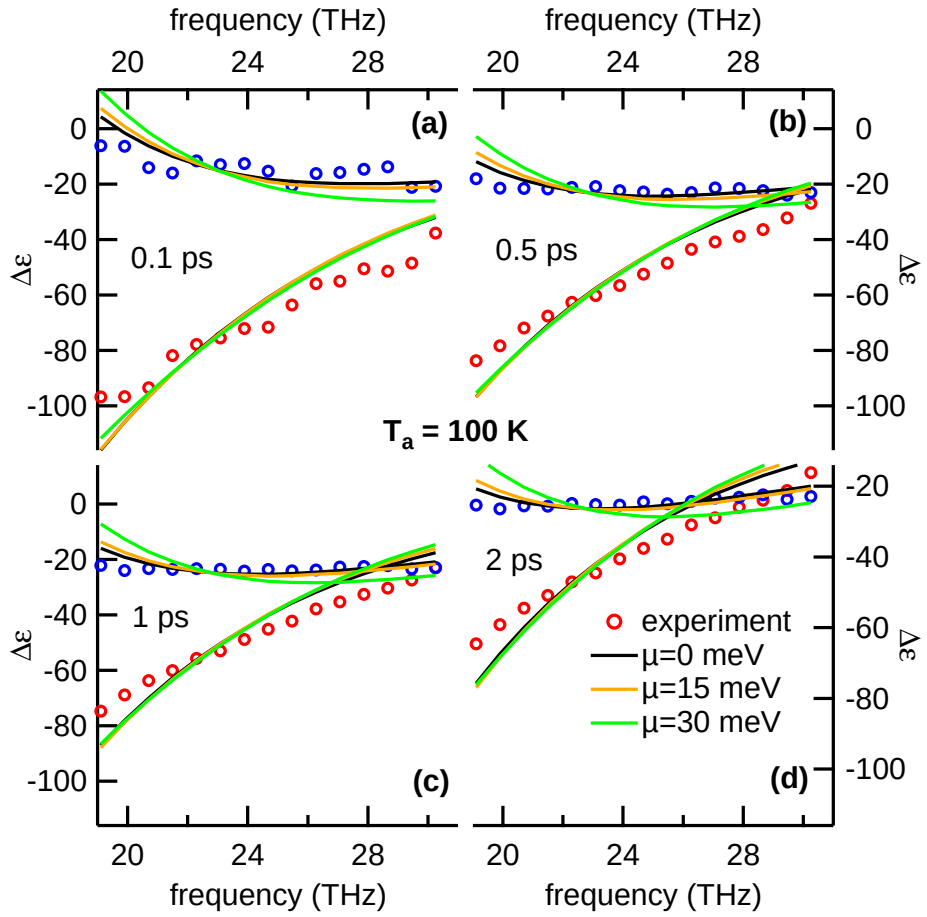

Figure 3.22: *Pump-induced changes of the dielectric function $\Delta\varepsilon_\tau(\omega)$ at a sample temperature $T_a = 100$ K for different pump-probe delays: (a) $\tau = 0.1$ ps, (b) $\tau = 0.5$ ps, (c) $\tau = 1$ ps and (d) $\tau = 5$ ps, respectively, together with models using different distribution functions and chemical potentials μ. Circles represent data for Re $\Delta\varepsilon$ (red) and Im $\Delta\varepsilon$ (blue), solid lines are fits to the data. Black: fit using one distribution function corresponding to a free fit with two distinct distributions leading to $\mu_{c,v} = 0$. Colored: fit using two different distribution functions with fixed chemical potentials $\mu_c = -\mu_v$.*

Fit Parameters vs. τ and T_a

From the IOT and DOT contributions, the three fit parameters T_e, ω_{pl} and Γ are inferred. This time, these fit parameters depend on pump-probe delay τ and sample temperature T_a. Figure 3.21 presents the resulting curves for two sample temperatures T_a. The parameters show similar behavior: an initial rise after photoexcitation for all three parameters at $\tau = 0$ ps reflects the deposition of energy into the system. Within 0.5 ps a fast decrease is observed, in agreement with calculation for electron-electron scattering and subsequent heating of SCOPs, as is also seen in [CYS+11,HM00,WKM10,MWBK11]. This is followed up by a slower relaxation due to phonon-phonon scattering [CYS+11,SKW+11], which will be discussed in Section 3.4.

Qualitatively similar two-component dynamics have also been observed with other time-resolved techniques [ITY+11,BRE09,NDSvD09,MGF+01,WSG+10,IHK+08,KACS10,SLZ11,CYS+11]. Further analysis as previously done, as well as References [KPS+05,BRE09,YSM+09,ITY+11] and simulations based on Boltzmann Peierls rate equations [BMH+07], have shown that the faster

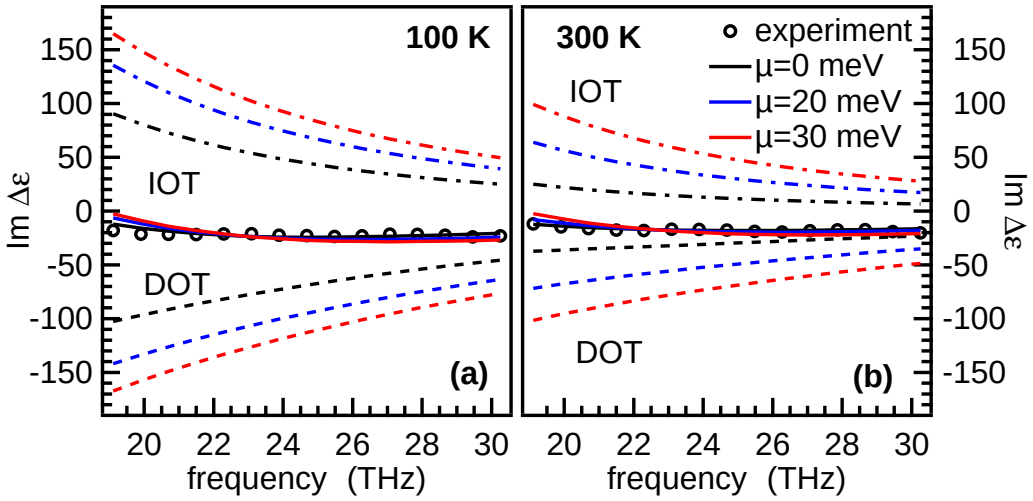

Figure 3.23: *DOT and IOT contributions to Im $\Delta\varepsilon$ for different chemical potentials as well as two different temperatures presented in panels (a) and (b). Circles represent data, solid lines fits to the data. Dotted lines represent IOT and DOT contributions.*

signal component reflects the thermalization of the electronic subsystem via electron-electron and electron-phonon scattering accompanied by energy transfer to the SCOPs.

Possibility of Non-Single Fermi-Dirac Carrier Distribution

In the applied model from Equation (3.7), a thermal electron distribution is assumed just like in equilibrium (*metallic* scenario). However, models have been proposed invoking separate distributions for electrons and holes and different chemical potentials μ_v and μ_c [BRE09]. This would lead to a band gap after photoexcitation as found in *semiconductors*. Both models can be applied to the measured data, as is discussed below.

To account for different chemical potentials, the chosen model is extended. Here, impact on the Drude response is captured by the fit paramater ω_{pl}, while the DOT contribution needs a modification. The interDOT term from Equation (1.23) includes the distribution function $f(\mu, T_e)$. Thus, band selective different μ_c and μ_v are included:

$$\varepsilon_{ii}^{\mathrm{interDOT}} = \frac{4\pi e^2\hbar^2}{Vm^2} \sum_{nn'\boldsymbol{k}} \frac{|\langle\, n\boldsymbol{k}\,|p_i|\,n'\boldsymbol{k}\,\rangle|^2}{(E_{n'\boldsymbol{k}} - E_{n\boldsymbol{k}})^2(E_{n'\boldsymbol{k}} - E_{n\boldsymbol{k}} - \hbar\omega - \mathrm{i}0^+)} \left[f(\mu_{n'\boldsymbol{k}}) - f(\mu_{n\boldsymbol{k}})\right] \ .$$

This extension allows two different ways to treat the problem:

1. take $\mu_{c,v}$ as an additional free fit parameter; or
2. choose two fixed $\mu_{c,v}$ and investigate the consequences concerning fits and fit parameters.

Figure 3.22 shows fits to $\Delta\varepsilon_\tau$, Figure 3.23 the resulting DOT and IOT contributions for both scenarios. For the semiconductor scenario $\mu_{c,v} = \pm 15$ meV, $\mu_{c,v} = \pm 20$ meV and $\mu_{c,v} = \pm 30$ meV have been chosen. The free fit leads to $\mu_{c,v} = (0 \pm 0.1)$ meV for all pump-probe delays and thus is identical with the metallic scenario. In contrast, two distinct $\mu_{c,v} = \pm 15$ meV lead to fits that agree less well with experimental data, as can be seen from Figure 3.22. According to Figure 3.23 the DOT contributions become more and more negative, while the IOT contributions increase.

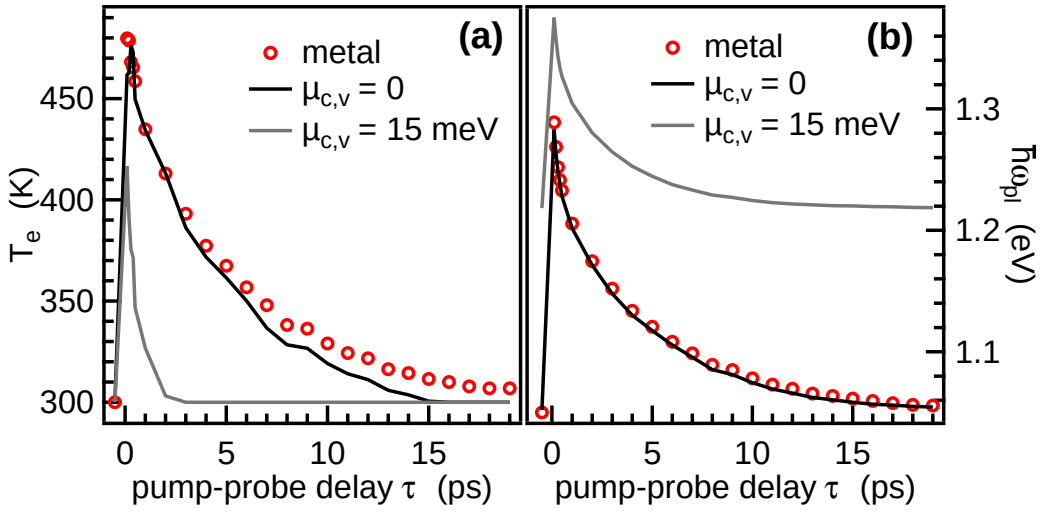

Figure 3.24: *Dependence on the pump-probe delay τ of (a) electronic temperature T_e and (b) plasma frequency $\hbar\omega_{\mathrm{pl}}$ as resulting fit parameters for different models: i) metal (circles), ii) fit with $\mu_{c,v}$ as additional fit parameters (black), iii) semiconductor with $\mu_c = 15$ meV and $\mu_v = -15$ meV (grey). Models i) and ii) lead to similar results with the same decays for both parameters while iii) differs notably.*

Using the applied fluence and electronic density of states for graphite (see Figure 3.4(b)), an estimation of the density of excited electrons and holes is given by $N = (2.5 \pm 1) \times 10^{25}$ m^{-3} which would imply a chemical potential of $\mu_i = (25 \pm 10)$ meV. Here, the error results from the unknown relation between applied and absorbed fluence in the experiment. The different scenarios are compared to the lowest possible μ.

The resulting fit parameters $T_e(\tau)$ and ω_{pl} are presented in Figure 3.24. The semiconductor scenario would lead to significant changes in the dynamics, introducing different behaviours for different parameters. This makes the semiconductor scenario unlikely.

In conclusion, the metallic scenario featuring only one distribution function for electrons provides better agreement with the experiment and more reasonable dynamics of the three fit parameters compared to the semiconductor scenario. These findings also agree with [WKM10, MWBK11].

3.3.3 Comparison of Equilibrium and Photoexcited Graphite

Photoexcited states of graphite are ruled by:

1. The distribution function of the electrons. Here, a Fermi-Dirac distribution is assumed after thermalization of the electronic system within 0.5 ps [ITY$^+$11, WOP$^+$11, IHK$^+$08, YSM$^+$09, MGF$^+$01, WSG$^+$10, SCK$^+$90]. Thus, the electronic temperature T_e can be used to describe the electrons.

2. The distribution function of the phonons. In graphite, only the small subset of SCOP modes can scatter with the electrons [PLM$^+$04, MRT$^+$04]. After at most 0.5 ps electrons and SCOPs are in equilibrium and can be described by just one temperature T_e, while all remaining phonon modes are still cold. Thus, a non-thermal distribution of phonons is found in photoexcited graphite.

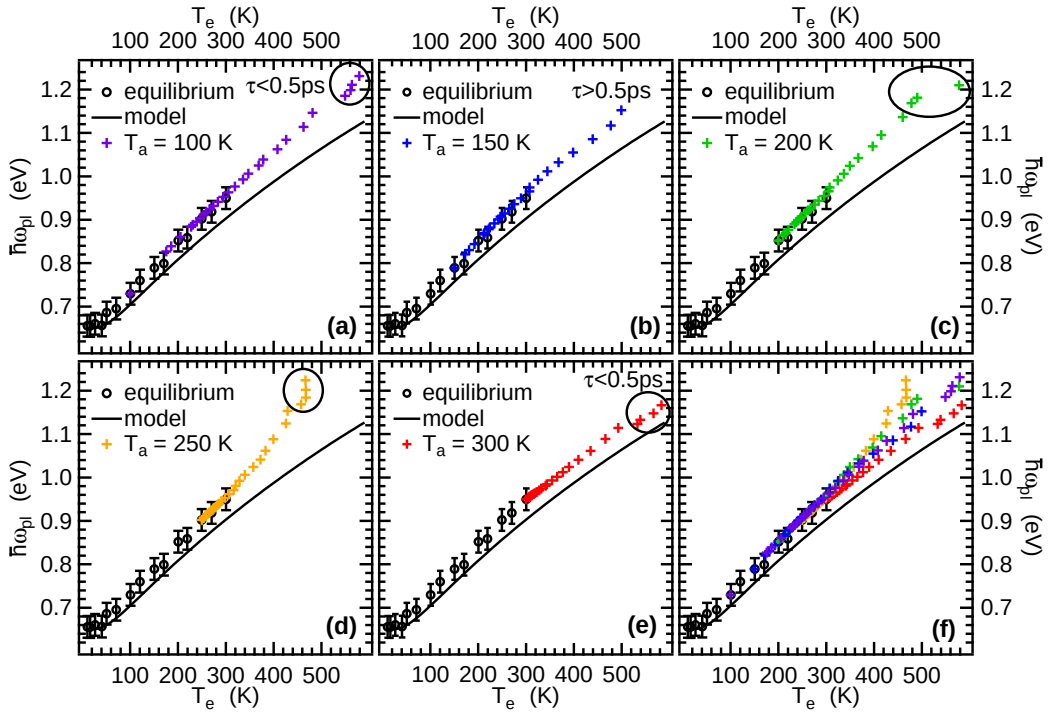

Figure 3.25: *Dependence on the electronic temperature of the plasma frequency $\hbar\omega_{\mathrm{pl}}(T_e)$ for different ambient temperatures T_a shown in panels (a)-(e) together with data obtained at equilibrium conditions and the model including the SWM band structure information. (f) Composition of $\hbar\omega_{\mathrm{pl}}(T_e)$ for all measured T_a. Pump-probe data show a thermal behavior, except $\tau < 0.5$ ps as marked by black circles.*

As has been shown, the dielectric function of graphite is well-described by three fit parameters: T_e, ω_{pl} and Γ.

The plasma frequency accounts for the electronic distribution. It can be used to do a consistency check of the applied model. If the electrons are described by a Fermi-Dirac distribution, $\omega_{\mathrm{pl}}(T_e)$ should match the equilibrium data $\omega_{\mathrm{pl}}(T_a)$. This temperature dependence of $\hbar\omega_{\mathrm{pl}}(T_e)$ is demonstrated in Figure 3.25(a) for different sample temperatures T_a. Here, pump-probe delays $\tau < 0.5$ ps account for the thermalization of the electrons.

The Drude scattering rate Γ accounts for the electronic and the phononic distribution (see Section 1.2.3). While electrons are well-described by T_e independently of T_a, phonons show a non-thermal distribution and thus a dependence on T_a should occur. Figure 3.26(a) displays Γ as a function of T_e for different ambient temperatures T_a. As expected, the gradient changes with T_a, indicating the sensitivity to the cold lattice. Additional calculations based on a many-particle density matrix framework [WKM10, MWBK11] show the electrons to reach higher temperatures T_e after photoexcitation for lower sample temperatures T_a. Here it turns out that the energy per electron is much larger at lower temperatures T_a, since the excitation energy is distributed among less charge-carriers (see Figure 3.26(b)). As a consequence, more SCOP modes are populated at lower temperatures T_a, leading to a more pronounced non-equilibrium and so to a higher scattering rate Γ. This is seen from Figure 3.26(a), where lower sample temperatures lead to higher absolute values of Γ. Therefore, the gradient in $\Gamma(T_e)$ is a fingerprint of the lattice temperature.

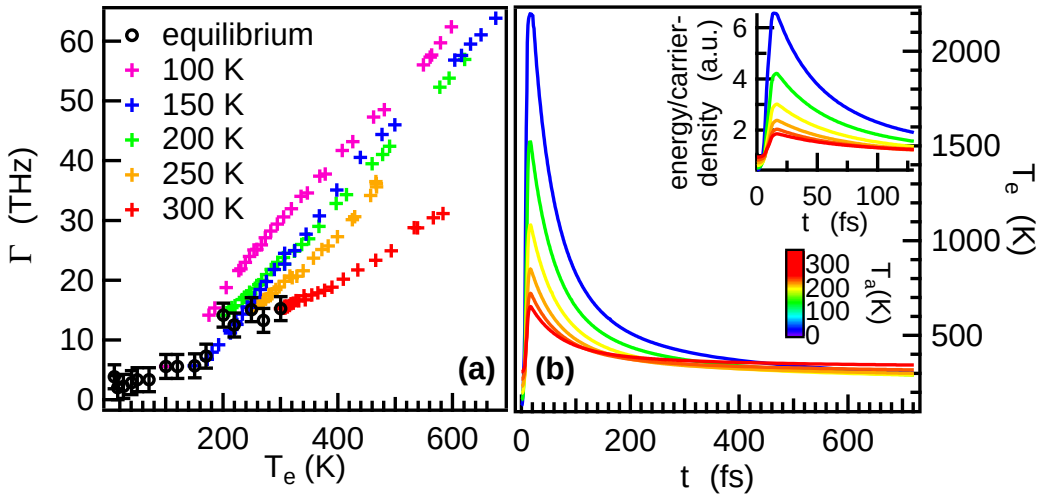

Figure 3.26: *(a) Dependence of the Drude scattering rate* Γ *on the sample temperature* T_a *as obtained from pump-probe measurements together with data taken at equilibrium conditions (black circles). Pump-probe data show differences with varied sample temperature. (b) Calculations based on a many-particle density matrix framework show an initial higher* T_e *at lower temperatures* T_a *after photoexcitation with applied fluences as used in the experiment. Inset shows the energy per charge carrier at different* T_a*.*

3.3.4 Summary for Photoexcited Graphite

At first sight, photoexcitation leads to similar effects as thermal heating. Above 15 THz, a bleaching is observed, due to blocked DOTs at higher electronic temperatures T_e. The MIR phase information shows an opposite trend to the equilibrium data. With increasing temperature both effects become smaller, since electrons are already thermally excited. Additionally, the used model allows an inclusion of different chemical potentials to distinguish between different charge-carrier distributions in the conduction and the valence band. The measured data are in favor of the assumption of just one distribution as can be found in metals. The opening of a band gap immediately after photoexcitation as would be expected from a semiconductor is rather unlikely.

The thermalization after photoexcitation has been studied in detail: within 0.5 ps, the electrons thermalize. This is shown by a thermal behavior of the plasma frequency after photoexcitation. In contrast, the Drude scattering rate shows a strong dependence on the sample temperature. This can be understood by means of a cold phonon bath. Initially only few SCOP modes are heated due to strong electron-phonon coupling only in the vicinity of the K and Γ points of the BZ. Also, few electrons are thermally excited at low temperatures, thus only few scattering partners exist. Here, theoretical calculations show the excitation energy per electron to be much higher at low temperatures, leading to a higher T_e immediately after photoexcitation. The larger non-equilibrium leads to different dynamics on the sub-picosecond timescale.

3.4 Phonon Cooling

So far, the optical properties of photoexcited graphite have been considered. Now, the dynamics after photoexcitation is investigated. The measurements show a two-component dynamics as can be seen from the τ-dependence (Figure 3.21). The fast component with a sub-picosecond timescale has been investigated so far, whereas the slow component, showing a picosecond timescale, will be discussed below. Here, the cooling of the SCOPs via scattering with low energy

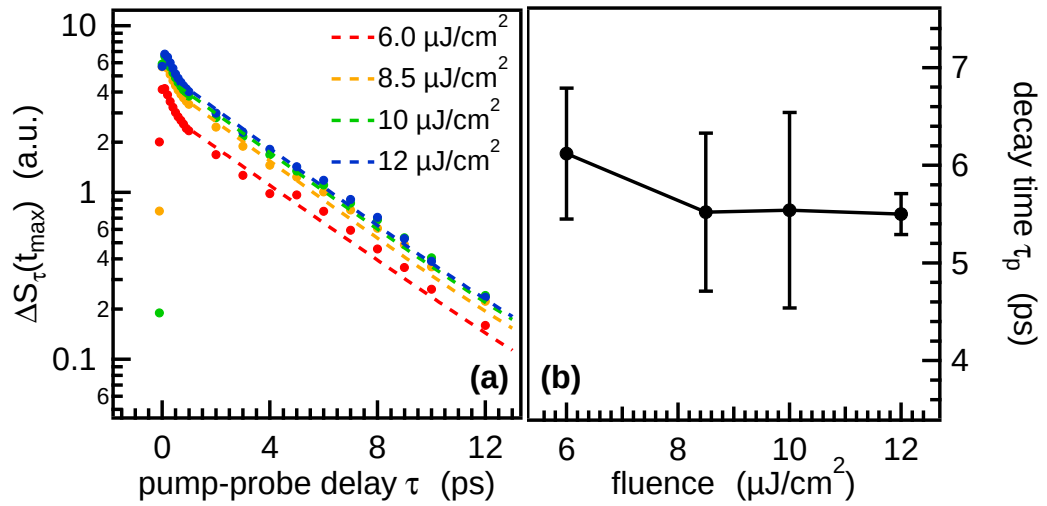

Figure 3.27: *(a) $\Delta S_\tau(t_{\max})$ as a function of pump-probe delay at 300 K at various pump fluences. Solid lines: biexponential fit. Note the fluence-independent slope of the slower relaxation component. (b) Time constants τ_p for the slower decay component resulting from the biexponential fits show no dependence on the applied fluence.*

phonon modes will turn out to be the dominant process.

Despite the small fraction of available phonon states, the fast electron cooling is brought about by the strong EPC in graphite [MRT+04, PLM+04], as has been discussed in Section 3.1.4. After less than 0.5 ps, the SCOPs have absorbed more than 90 % of the electronic excess energy, and a quasi-equilibrium of electrons and SCOPs is established [KPS+05, BRE09, YSM+09, ITY+11]. Then, the slower component of the pump-probe signal is associated with the cooling of the combined subsystem electrons plus hot SCOPs [KPS+05, YSM+09]. Since most of the pump energy is contained in the hot phonons, the slow decay directly reflects the SCOPs' lifetime [YSM+09, BMH+07].

3.4.1 Measurement of Pump-Probe Signals

The temperature is varied to obtain more information which finally leads to an understanding of the energy relaxation process after photoexcitation in graphite. Here, the most important quantity measured is the relaxation constant of the pump-induced changes in the electronic temperature $\Delta T_e(\tau)$. In the case of graphite, this is equivalent to the difference signal $\Delta S(\tau)$ of the excited and unexcited sample as can be measured in a PP-scan (see Section 2.3.3). The argumentation may be briefly introduced:

1. Figures 3.14(c) and 3.25 show the linearity $\omega_{\mathrm{pl}} \propto T_e$.
2. In combination with the model for ω_{pl} from Equation (3.6) and graphite's quasi-linear eDOS $D(\epsilon)$ for the pump-fluences applied here, the system should give a linear response.
3. The assumption of linearity is further verified by fluence dependent measurements as presented in Figure 3.27(b). Though a higher fluence should lead to a higher initial electronic temperature, the decay time remains constant.

Figure 3.16(a) shows the pump-induced changes $\Delta S_\tau(t)$ in the transmitted THz field. In order to monitor the relaxation of the excited sample, $t = t_{\max}$ is considered, at which time the maximum of the pump-induced THz transient is located. The resulting trace of $\Delta S_\tau(t_{\max})$ vs. pump-probe

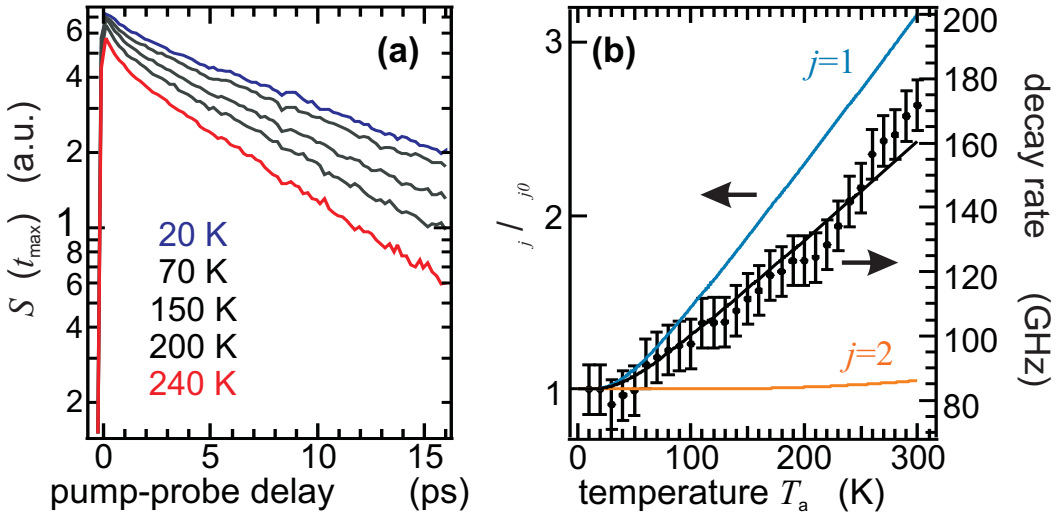

Figure 3.28: *(a) Temporal decay of the pump-induced signal maximum $\Delta S_\tau(t_{\max})$ at several ambient temperatures T_a. (b) Temperature dependence of the resulting scattering rates γ (right axis). Solid lines: normalized contributions (left axis) of phonon decay channels j=1 and 2 shown in Figure 3.29(b) as well as a fit of a linear combination of the two curves to the experimental data. Figure is taken from [SKW+11].*

delay τ is shown in Figure 3.27(a) for different pump fluences. In the used experimental setup, the applied fluences are in the range of 6 to 12 μJ/cm^2 leading only to small changes in the chemical potential as has been discussed in Section 3.3.2.

In Figure 3.27(a) all traces exhibit a biexponential decay with a fast and slow component featuring time constants of 0.8 ps and 5.5 ps at 300 K, respectively. As already indicated by the identical slopes of the curves in Figure 3.27(a), the slow time constants presented in Figure 3.27(b) are found to be independent of the applied laser fluence demonstrating that they represent sample-intrinsic quantities.

In order to obtain insights into the energy decay of the SCOPs, pump-probe traces $\Delta S_\tau(t_{\max})$ at various ambient temperatures T_a have been taken. As shown in Figure 3.28(a), the decay of the slower component of the pump-probe signal becomes considerably faster with rising T_a. The hot SCOP lifetimes are obtained as the time constant $1/\gamma$ of the slower relaxation component of the signal. Figure 3.28(b) shows the resulting decay rate γ vs. temperature. Here, γ increases by more than 100 % when the ambient temperature increases from 5 to 300 K.

It should be mentioned that the measured fast decay indicates a temperaure dependence similar to the slower component. Due to the experiment's temporal resolution the fits obtain large errors, thus further discussion may be inappropriate.

3.4.2 Decay in Terms of Three-Phonon Processes

The cooling of the thermalized electron-SCOP system proceeds via

1. annihilation of an electron-hole pair [All87] or
2. decay of a SCOP [BLMM07].

Both result in the emission of phonons into cold lattice modes. The first scenario is not expected to occur on picosecond time scales as it involves emitted phonons with energies more than one

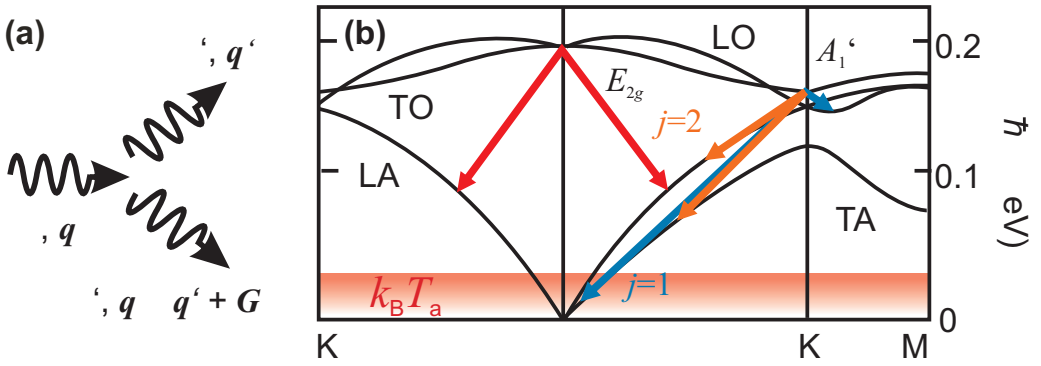

Figure 3.29: *(a) Schematic of the decay of a phonon with momentum* $\boldsymbol{q}$ *and energy* $\hbar\omega$ *into two phonons with lower energy. Momentum and energy conservation restrict the set of allowed decay channels.* $\boldsymbol{G}$ *is a reciprocal lattice vector. (b) Black: schematic of the phonon dispersion of graphite. Arrows: examples of allowed decay channels of SCOPS according to Ref. [PLM+04]. The orange area indicates the thermal energy* $k_B T_a$ *with* T_a *ranging from 5 to 300 K. Adapted from [SKW+11].*

order of magnitude smaller than those of the SCOPs [YSM+09]. In addition, the coupling of these phonons to the electrons is negligible as compared to the SCOPs as has been discussed in Section 3.1.4. Finally, according to a two-temperature model [All87], the first mechanism should result in a slower decay with increasing temperature T_a, in contrast to the observations from Figure 3.28(b). Thus, it is reasonable to assume the combined cooling of electrons and hot SCOPs to be mediated by anharmonic phonon-phonon coupling of SCOPs with two phonons with lower energy [BLMM07, YSM+09, CYS+11] as previously discussed in Section 3.1.4. Such scattering is schematically shown in Figure 3.29(a).

Such decay can be modeled in terms of the distribution of participating phonon modes as introduced by Equation (1.5). Each decay channel j makes a contribution

$$\gamma_j = \gamma_{j0} \left[1 + b(\omega'_j, T_a) + b(\omega_j - \omega'_j, T_a)\right] \tag{3.8}$$

to the total energy decay rate $\gamma = \sum \gamma_j$ of the hot-phonon system [LvdLK71]. Here, γ_{j0} is the rate at vanishing sample temperature, ω_j the SCOP frequency, and ω'_j and $\omega_j - \omega'_j$ are the frequencies of the emitted phonons. Each of these three-phonon processes has to conserve phonon energy and wavevector, thus greatly reducing the set of allowed final modes. Possible decay channels have been figured out by [BLMM07] and are presented in Section 3.1.4. It has been found that the lower phonon energy $\hbar\omega'_j$ can only derive from a few narrow intervals between 0 and $\hbar\omega_j/2$. Prominent examples of such decay channels are shown in the schematic of the phonon dispersion relation of graphite in Figure 3.29(b).

The interval with the lowest phonon energies is centered around $\hbar\omega'_1 = 10.5$ meV and associated with acoustic phonons emitted in the decay of the A'_1-K mode indicated by blue arrows in Figure 3.29(b). Using Equation (3.8), the normalized rate γ_1/γ_{10} of this decay channel as a function of T_a has been calculated. As seen from Figure 3.28(b), γ_1 increases by more than a factor of 2 when the temperature increases from 5 to 300 K. This strong temperature sensitivity arises because the phonon energy $\hbar\omega'_1$ is comparable to the thermal energy $k_B T_a$ as highlighted by the light red area in Figure 3.29(b).

In contrast, considering an allowed decay channel with the next-higher energy $\hbar\omega'_2 = 60$ meV of the emitted low-energy phonon indicated by orange arrows in Figure 3.29(b), one obtains

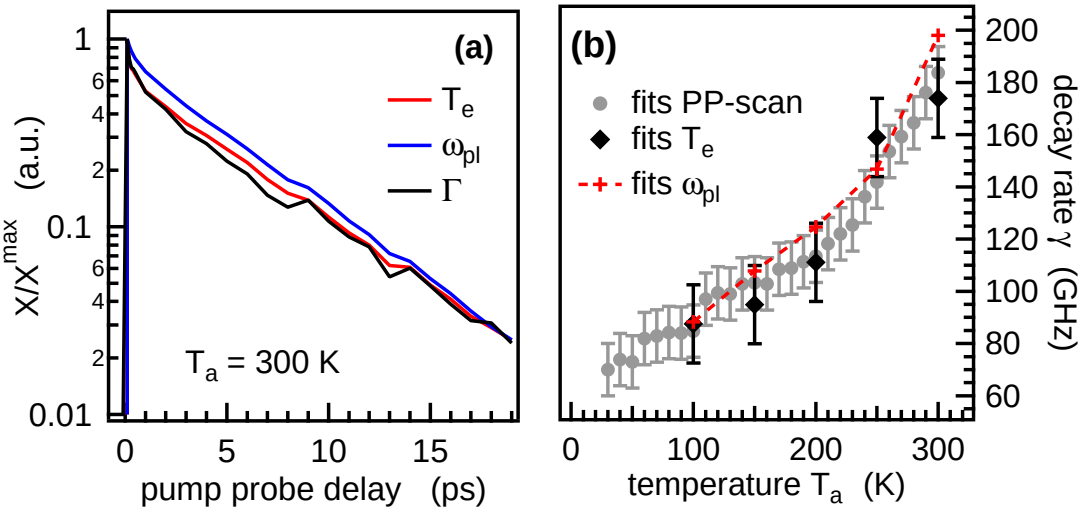

Figure 3.30: *(a) Pump-probe data for all fit parameters ($X = T_e, \omega_{\mathrm{pl}}, \Gamma$), normalized on the maximum $X^{\max}$ of the pump-induced changes taken at $T_a = 300$ K. (b) T_a-dependence of the resulting decay rates γ from Figure 3.28(b) (grey), exponential fit to T_e (black) and fit to E_{pl} (red). The Drude scattering rate Γ shows the same slope but is not shown here.*

a curve with nearly negligible temperature dependence shown by the $j = 2$ curve in Figure 3.28(b). Similar curves are obtained for all remaining decay channels j as they involve even higher energies $\hbar\omega'_j$. These differences in the temperature dependence have also been evaluated by [BLMM07]. An example is the symmetric decay of the E_{2g}-Γ mode indicated by red arrows in Figure 3.29(b). Therefore, it is sufficient to fit a linear combination of γ_1 and γ_2 to the measured decay curve of γ vs. T_a, with γ_{10} and γ_{20} as fit parameters. Whereas γ_2 merely contributes a constant offset, γ_1 sets the slope of the curve. Best fit results are obtained for $1/\gamma_{10} = 22.1$ ps and $1/\gamma_{20} = 30.5$ ps, providing good agreement with experimental data given by the black solid line in Figure 3.28(b). Thus, the results are compatible with the notion that at 300 K the energy relaxation of the hot SCOPs is dominated by the decay of A'_1 phonons at the K point into acoustic phonons with quantum energies of about 10 meV.

As a consistency check, the relaxation rates γ of the SCOPs as obtained here should be compared with the previously presented temperature dependence of the changes in the dielectric function. Figure 3.30(a) presents a logarithmic plot of the decay of the three fit parameters T_e, ω_{pl} and Γ with pump-probe delay τ. Furthermore, Figure 3.30(b) presents the exponentially fitted decay rates measured at five different temperatures between 100 K and 300 K together with the data evaluated from $\Delta S_\tau(t_{\max})$. The previously obtained decay rates match the rates resulting from the parameters. As a consequence, the modeling of pump-probe data using Drude theory and linear response together with band structure calculation leads to physical quantities that show the same temperature dependence of the dynamic as the pump-probe signal itself [KAK$^+$09, PKG$^+$09].

3.4.3 Discussion and Conclusion

These findings for the energy relaxation can be compared to previous temperature-dependent measurements of the SCOP decay of photoexcited graphite. Those works made use of time-resolved incoherent Raman scattering and report decay times of 2.2 ps [CYS$^+$11] and 2.4 ps [KACS10] at 300 K, noticeably shorter than the 5.5 ps observed here. It should be noted that studies based on other time-resolved techniques such as transient reflectance or transmittance

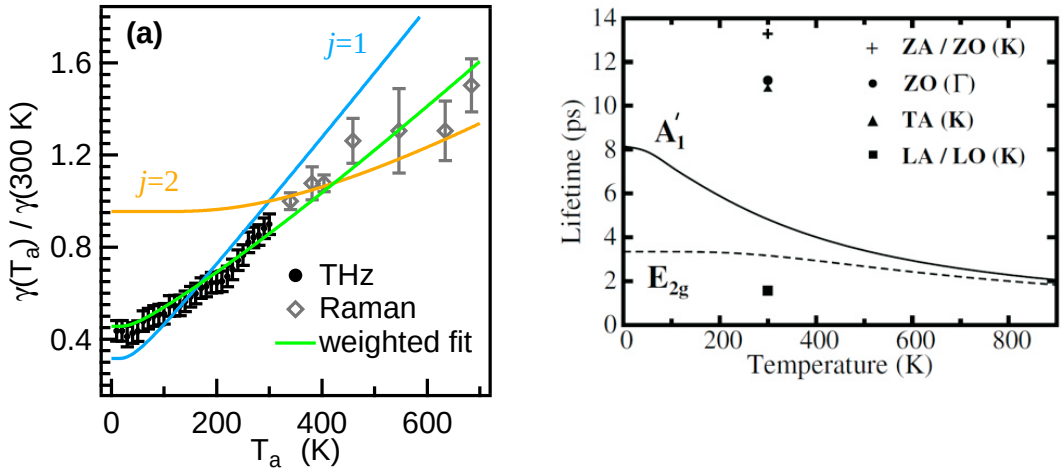

Figure 3.31: *(a) Comparison of decay rates from THz experiments from Figure 3.28(b) (black) and Raman measurements (grey) from Ref. [CYS+11], both normalized to the value at $T_a = 300$ K. Solid lines: normalized contributions of phonon decay channels j=1 and 2 shown in Figure 3.29(b) as well as a fit of a linear combination of the two curves to the experimental data. Here, Raman data are in agreement with the linear combination fitting the THz data. (b) Calculated temperature dependence of the decay times for A_1' and E_{2g}, taken from [BLMM07]. Here, E_{2g} shows virtually no dependence on the temperature in contrast to A_1'.*

[WSG+10, NDSvD09], photoelectron spectroscopy [ITY+11] and electron diffraction [SLZ11] also report a broad variety of time constants of the slow signal component. This variety may be related to the use of different probing techniques and samples of different thickness [NDSvD09, HHM+11]. In particular, since both THz and Raman signal reflect the temperature of the hot phonons, the different time constants observed in these experiments most likely arise from the particular sample used. Whereas the graphite thin film investigated here is homogeneously excited as has been stated in Section 2.2, transport effects into the depth of the inhomogeneously excited bulk crystal used by [CYS+11] may accelerate the dynamics inside the probed volume. Here, unpublished first results from transport measurements on graphite by using time-resolved SHG technique [MPB08] indicate a significant contribution from electronic transport.

However, despite the differences in time constants, the relative changes as a function of temperature are comparable for the Raman- and THz-based work: an increase of the phonon decay rate by about 70 % was observed by increasing T_a from 300 to 700 K as reported by [KACS10, CYS+11] while a 100 % increase from 5 to 300 K is found in THz experiments. It should be noted that the fit to the decay rate $\gamma(T)/\gamma(300\,\mathrm{K})$ vs. T_a presented here would also give a reasonable description of the normalized time-resolved Raman data as can be seen from Figure 3.31. Here, the color code is in accordance to Figures 3.28(b) and 3.29(b). Conversely, the model chosen in [CYS+11] would not yield a good description of THz transmission data as it involves too high phonon energies $\hbar\omega_j'$. In other words, low-temperature experiments allow a better identification of the phonon decay processes involving small phonon energies of the order of 10 meV.

Finally, these findings should be compared to DFT calculations by [BLMM07, BRR+08] of the anharmonicity-related lifetime of various phonon modes at the Γ and K points. The experimental results agree well with the predicted temperature dependence of the A_1'-K mode [BLMM07] as presented in Figure 3.31(b) as well as the branching ratio of the different decay processes j: here

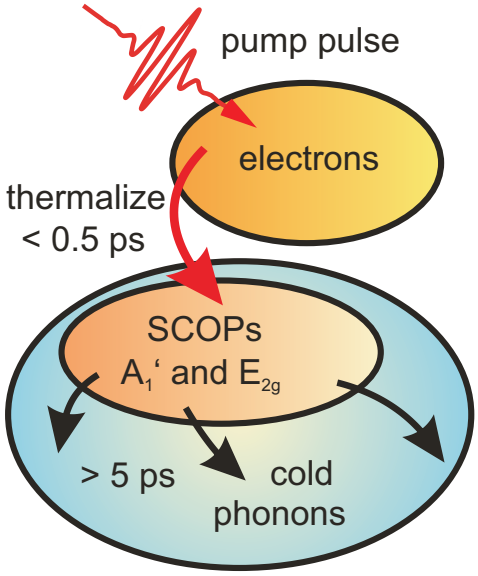

Figure 3.32: *Schematic of the relaxation processes in graphite after photoexcitation. Electrons are excited via DOTs and thermalize within 0.5 ps and concurrently heat the SCOP modes. On a picosecond timescale, the SCOPs cool via anharmonic phonon-phonon scattering.*

the experiment states

$$\frac{\gamma_{01}}{\sum \gamma_{0j}} = 0.58 \,,$$

while theory predicts 0.56. Absolute numbers agree roughly:

$$\frac{1}{\gamma_{10}} = 22.1 \text{ ps} \,,$$

as derived from experiment, which is larger than

$$\frac{1}{\gamma_{10}} = \frac{8.2 \text{ ps}}{0.56} = 14.6 \text{ ps} \tag{3.9}$$

predicted by theory. However, theory [BLMM07] also suggests a strong contribution from the decay of the E_{2g}-Γ mode, with a much shorter lifetime of about 3.3 ps at vanishing temperature. Such short phonon lifetimes are not observed in THz-transmission experiments. The reason for this discrepancy is not yet understood.

3.5 Summary and Outlook

The combination of temperature-dependent THz transmission measurements on graphite under equilibrium conditions and after photoexcitation reveals information on electronic transitions, electron-phonon coupling and anharmonic phonon decay.

It has been shown that thermal heating makes graphite more transparent for THz radiation. Modeling including direct and indirect optical transitions provide information on the microscopic reasons for such behavior. At higher sample temperatures T_a, more electrons are excited. Therefore possible DOTs are blocked. The opposite trend occurs for IOTs since more scattering takes place due to more scattering partners. This affects the plasma frequency ω_{pl} as well as the Drude scattering rate Γ. Both increase with temperature. In addition, ω_{pl} can be modeled by using band structure information, showing the consistency between fits to the dielectric function and the applied model.

Photoexcitation leads to similar effects. Above 15 THz, a bleaching due to blocked DOTs is found. With increasing temperature the relative effect becomes smaller, since electrons are already thermally excited. Considering different chemical potentials indicates that just one Fermi-Dirac distribution occurs as can be expected in metals.

Within 0.5 ps, the electrons thermalize. This is shown by a thermal behavior of ω_{pl} only 0.5 ps after photoexcitation. In contrast, the Drude scattering rate shows a strong dependence on the sample temperature. This can be understood by means of cold phonons and only few thermally excited electrons at low temperatures. Therefore, only few scattering partners exist at low temperatures. Additonal theoretical calculations show that the excitation energy per electron is much higher at low temperatures, leading to higher T_e immediately after photoexcitation as well as different dynamics on the subpicosecond timescale.

Figure 3.32 summarizes the energy relaxation in graphite: an initially fast decay that can be adressed to the electronic thermalization and subsequent heating of the SCOPs, and a slower decay showing a picosecond time constant. The temperature dependence of the slower relaxation shows a faster decay with increasing temperature. This effect can be explained by anharmonic phonon-phonon scattering with low energy phonon modes. The found temperature dependence then favors a more pronounced heating of the A_1'-K mode, for which a higher value has been found in the EPC.

All findings show that graphite may have interesting applications in MIR photonics. Its optical properties at MIR frequencies can be modulated with considerable depth, suggesting its use in ultrafast intensity and phase modulators.

Chapter 4

Cuprate Superconductors

Superconductivity has been discovered 100 years ago. This state of matter allows currents to flow without resistance and enables unique magnetic properties, leading to Josephson effects in tunnel contact. In terms of theoretical framework, the BCS theory for superconductivity from 1957 led to two key insights: pairing of electrons and condensation of these pairs into a coherent state describes all classical superconductors and sets the frame even for an understanding of novel superconductors. On the experimental side, the discovery of cuprate superconductors with transition temperatures above the boiling point of liquid nitrogen in 1986 led to still unsolved questions: neither the pairing mechanism nor the novel pseudogap state are sufficiently understood.

This chapter deals with the physics of cuprate superconductors and temperature-dependent THz-transmission measurements on the compound $Bi_2Sr_2CaCu_2O_{8-\delta}$. It is based on the more general concept of Cooper pairing as was presented in Section 1.1.5 and pursues this framework to the BCS theory. Below, high-T_c superconductors will be introduced with special emphasis on the cuprates. Here, differences between BCS superconductors and cuprates are demonstrated and an overview of the controversy about the phase diagram is given. Temperature-dependent experiments were performed in equilibrium and after photoexcitation in the frequency domain. Here, the superconducting phase transition as well as an indication of the pseudogap are found. Photoexcitation can be used to study quasi-equilibrium conditions and thus introduces a second complementary method to study the phase diagram of superconducting materials by THz spectroscopy.

4.1 General Remarks on Superconductivity

In 1908, Heike Kamerlingh-Onnes succeeded in liquifying helium at a temperature of 4.2 K [KO08]. He performed first experiments in the then accessible low temperature regime on a scientific problem of his days: the electrical resistance of metals near to the absolute zero. Several possibilities had been proposed [Blu09], but when a mercury sample was cooled below the boiling point of LHe, surprisingly the resistance disappeared suddenly [KO11a, KO11b]. This characteristic behavior for superconductivity is seen in data from Kamerlingh-Onnes' experiments provided by Figure 4.1. Kamerlingh-Onnes was soon able to demonstrate the ability of an electrical current to pass round a superconducting circuit without observable reduction. Only one year later, in 1912, tin and lead have also been found to be superconducting. A hundred years have passed since and superconductivity still is a hot topic. While the classical superconductivity has been understood in terms of Cooper pairing (see Section 1.1.5) mediated by lattice vibrations about half a century ago, phonon mediation seems not to be the case for novel high-T_c superconductors such as cuprates.

In the following section, first the general properties of superconductors are introduced, includ-

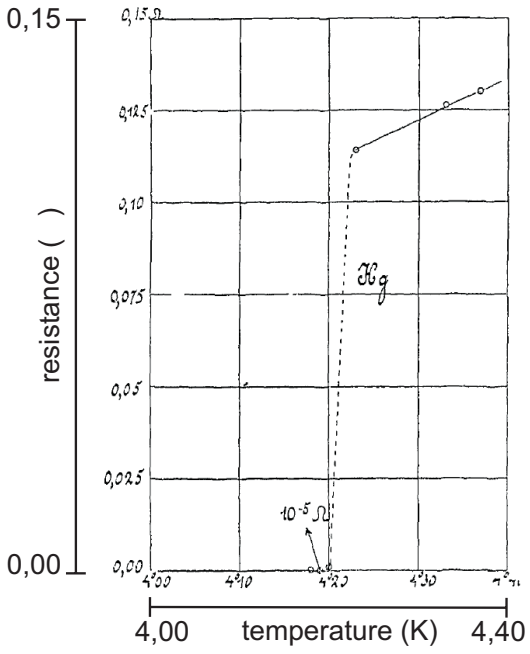

Figure 4.1: *Diagram of the vanishing resistivity at low temperatures in the case of mercury taken from Ref. [KO12].*

ing the BCS theory, before the differences between classical superconductors and cuprates are discussed. Here, special interest is paid to the phase diagram. Then, the physical properties of the cuprate $Bi_2Sr_2CaCu_2O_{8-\delta}$ are introduced, before the experimental results for that material are discussed.

4.1.1 Macroscopic Properties of Superconductors

At first sight, the resistance decreases to zero when superconductors are cooled down below a critical temperature T_c. Additionally, the zero resistance at low temperatures could be destroyed if the material was subjected to a magnetic field $\boldsymbol{B}$.

First experiments pointed towards a simple description of superconductors as perfect conductors. However, this notion would have severe consequences arising from classical electrodynamics: a changing applied magnetic field induces a voltage in a conductor. A superconducting wire could not support such voltage because, by Ohm's law, an infinite current would have to flow. Therefore, the magnetic field inside a superconductor would never be able to change. This then implies that a superconductor would trap any magnetic field present when you cooled it down and keep that trapped magnetic field until you warmed it up again [Blu09]. In 1933 Meissner and Ochsenfeld showed, contrary to that expectation, that any magnetic field is not trapped in a superconductor but appeared to be expelled from it. Thus, superconductors are perfect diamagnets. A schematic of the so-called Meissner-Ochsenfeld effect is provided in Figure 4.2. It makes no difference whether the magnetic field is applied to the superconductor below (panel (a)) or above (panel (b)) T_c: each time it is expelled from the interior, due to electrical screening currents which flow across its surface and act to screen the interior of the superconductor from the externally applied magnetic field. The observation that superconductors are perfect diamagnets leads to the insight that superconductivity is a well-defined thermodynamic state and does not depend on the sample's history. The phase transition between normally conducting and superconducting phase is of second order because no transition heat occurs. The resulting discrepancy between the electrodynamical and thermodynamical description had not been solved until the BCS theory in 1957.

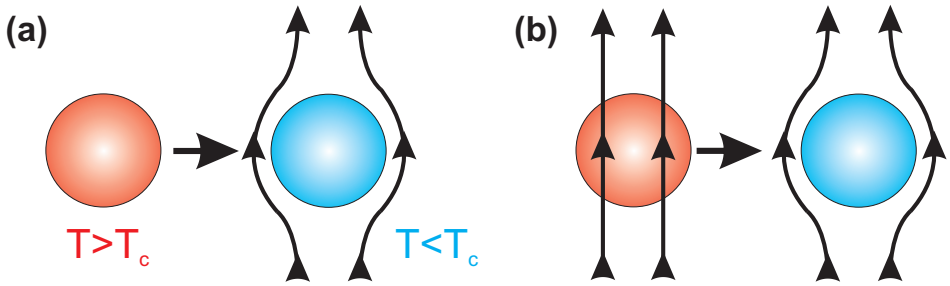

Figure 4.2: *Schematic of the Meissner-Ochsenfeld effect showing a superconductor to be perfectly diamagnetic: (a) the magnetic field is switched on below T_c. The superconductor repels the field completely. (b) The magnetic field is switched on above T_c. Again, the superconductor repels the field.*

A first ansatz for the electrodynamics introduced a 'two-fluid' model for superconductors adding a so-called supercurrent $\boldsymbol{j_s}$ to the normal current $\boldsymbol{j_o}$ [Buc94, vL49]. Since both should be independent of each other, an additional differential equation appears, describing the supercurrent [vL49]:

$$\frac{\partial(\lambda \boldsymbol{j}_s)}{\partial t} = \boldsymbol{E} \qquad \mathrm{rot}(\lambda \boldsymbol{j}_s) = -\boldsymbol{B}\,. \tag{4.1}$$

Here, the current of the superconductor is connected with the magnetic field instead of the applied voltage [Blu09]. This led to the insight that Maxwell's theory of electromagnetism does not include the physics of superconductivity. Now it was possible to describe the exclusion of magnetic fields from the interior of superconductors. Notably, in a very short distance inside the surface, the so-called London penetration depth λ, the magnetic fields are able to penetrate, as was additionally found in experiments. An ansatz for cubic crystals with N_{sl} superconducting electrons was given by [vL49]:

$$\lambda = \frac{m}{e^2 N_{\mathrm{sl}}}\,. \tag{4.2}$$

4.1.2 Microscopic Properties of Superconductors

In 1950, the dependence of the superconducting state on the isotopic mass in the case of mercury was discovered [RSWN50, Max50], pointing towards a phonon-mediated mechanism for superconductivity. The combination with the concurrently established Fröhlich model of Section 1.1.4 led to the description of superconductivity via Cooper pairs consisting of two bound electrons with opposite spin and momentum (see Section 1.1.5). To describe the superconductivity in classical superconductors, a second condition besides the pairing must be fulfilled: the condensation of Cooper pairs into a coherent state. The so-called BCS theory (according to Bardeen, Cooper and Schrieffer) from 1957 [BCS57] is summarized here, since it provides access to the energy gap Δ which has been found to be the main characteristic feature for all superconductors.

First, a product state of N Cooper pairs is considered:

$$\tilde{\Phi}^{(N)}_{\mathrm{BCS}}(\boldsymbol{r}_1 \ldots \boldsymbol{r}_N) = \hat{A} \cdot \psi(\boldsymbol{r}_1 - \boldsymbol{r}_2) \cdot \psi(\boldsymbol{r}_3 - \boldsymbol{r}_4) \cdot \ldots \cdot \psi(\boldsymbol{r}_{N-1} - \boldsymbol{r}_N)\ ,$$

with antisymmetry operator $\hat{A}$ and wavefunctions for one single Cooper pair including probability amplitudes $g_{\boldsymbol{k}}$ to find an electron pair with wavevectors $\boldsymbol{k}$ and $-\boldsymbol{k}$, as has been discussed in Section 1.1.5:

$$\psi(\boldsymbol{r}_{i-1} - \boldsymbol{r}_i) = \sum_{\boldsymbol{k}} g_{\boldsymbol{k}} e^{\mathrm{i}\boldsymbol{k}\cdot(\boldsymbol{r}_{i-1}-\boldsymbol{r}_i)} \chi^{(i-1)}_{\uparrow} \chi^{(i)}_{\downarrow}\,.$$

The product state then yields:

$$\left|\tilde{\Phi}_{\mathrm{BCS}}^{(N)}\right\rangle = \sum_{\boldsymbol{k}_1}\sum_{\boldsymbol{k}_2}\cdots\sum_{\boldsymbol{k}_{\frac{N}{2}}} g_{\boldsymbol{k}_1} g_{\boldsymbol{k}_2}\cdots g_{\boldsymbol{k}_{\frac{N}{2}}}\hat{a}^\dagger_{\boldsymbol{k}_1\uparrow}\hat{a}^\dagger_{-\boldsymbol{k}_1\downarrow}\hat{a}^\dagger_{\boldsymbol{k}_2\uparrow}\hat{a}^\dagger_{-\boldsymbol{k}_2\downarrow}\cdots\hat{a}^\dagger_{\boldsymbol{k}_{\frac{N}{2}}\uparrow}\hat{a}^\dagger_{-\boldsymbol{k}_{\frac{N}{2}}\downarrow}|\mathrm{vac}\rangle \ , \tag{4.3}$$

being an eigenstate of the particle number operator $\hat{N}$; thus follows for the BCS ground state:

$$|\Phi_{\mathrm{BCS}}\rangle = C\prod_{\boldsymbol{k}}\left(1+g_{\boldsymbol{k}}\hat{a}^\dagger_{\boldsymbol{k}\uparrow}\hat{a}^\dagger_{-\boldsymbol{k}\downarrow}\right)|\mathrm{vac}\rangle = C\left(1+\lambda_2\tilde{\Phi}^{(2)}_{\mathrm{BCS}}+\lambda_4\tilde{\Phi}^{(4)}_{\mathrm{BCS}}+\ldots\right) \ . \tag{4.4}$$

Here, the second term presents an alternative formulation of the first one as a linear combination of eigenstates $\tilde{\Phi}^{(N)}_{\mathrm{BCS}}$ of $\hat{N}$ [Gro06]. It should be emphasized that the BCS ground state itself is not an eigenstate of $\hat{N}$, i.e. the number of Cooper pairs and electrons is not conserved. Instead, the total phase is fixed. Now, the coefficents $g_{\boldsymbol{k}}$ (or likewise λ_n) have to be chosen to minimize the total energy. Since the particle number is not conserved, the free energy

$$F = \langle H\rangle - \mu\langle N\rangle = \langle\Phi_{\mathrm{BCS}}|\,\hat{H}_{\mathrm{red}} - \mu\hat{N}\,|\Phi_{\mathrm{BCS}}\rangle$$

has to be minimized, usually using the so-called reduced hamiltonian, describing the interaction $w(k,k')$ of only two Cooper pairs:

$$\hat{H}_{\mathrm{red}} := \sum_{\boldsymbol{k}\sigma}\epsilon_{\boldsymbol{k}}\hat{a}^\dagger_{\boldsymbol{k}\sigma}\hat{a}_{\boldsymbol{k}\sigma} + \sum_{k,k'} w(k,k')\underbrace{\left(\,\hat{a}^\dagger_{\boldsymbol{k}\uparrow}\hat{a}^\dagger_{-\boldsymbol{k}\downarrow}\,\right)}_{1^{\mathrm{st}}\text{Cooper pair}}\underbrace{\left(\,\hat{a}_{-\boldsymbol{k}'\uparrow}\hat{a}_{\boldsymbol{k}'\downarrow}\,\right)}_{2^{\mathrm{nd}}\text{Cooper pair}} \ . \tag{4.5}$$

Defining the order parameter as

$$\Delta_q := -\sum_k w(q,k)\,\langle\Phi_{\mathrm{BCS}}\,|\hat{a}_{-\boldsymbol{k}\uparrow}\hat{a}_{\boldsymbol{k}\downarrow}|\,\Phi_{\mathrm{BCS}}\rangle \ ,$$

leads to the BCS gap equation:

$$\Delta_q = -\frac{1}{2}\sum_k w(q,k)\frac{\Delta_k}{\sqrt{(\epsilon_k-\mu)^2+|\Delta_k|^2}} \ . \tag{4.6}$$

This equation defines the size of the band gap of a classical superconductor. Superconductivity can be found if $\Delta_k \neq 0$, otherwise the material is normal-conducting. The size of the bandgap thus is $2\Delta_k$, two times the pairing energy of a Cooper pair (Equation 1.10) and dependent on temperature. The idea of Cooper pairs offers a way of understanding the occurance of a band gap usually ascribed to insulators: it takes at least the energy $2\Delta_k$ to break pairs up. In a normal metal, electrons can absorb an arbitrarily small amount of energy. In a superconductor nothing happens until the energy supplied matches $2\Delta_k$. Once the gap has bridged, energy can be absorbed. This effect can be measured by looking at the way in which superconductors absorb electromagnetic waves in the MIR spectral range. If the waves have a photon energy smaller than the gap energy, the waves are not absorbed. As soon as their energy is large enough, Cooper pairs can be broken apart and energy is absorbed [Blu09]. Since gap sizes are found to be in the meV range, THz radiation is well suited to study the superconducting state.

It should be mentioned that Cooper pairs do not exhibit excited states. Excitations of the superconducting state leads to broken Cooper pairs, which become two fermionic *quasi particles*. Since the BCS wavefunction shows s-symmetry, an isotropic medium has been considered.

To summarize, two main features cause superconductivity:

1. Cooper pairs as introduced in Section 1.1.5 have to be formed,

2. these Cooper pairs have to condensate into a coherent state with fixed phase, e.g. the BCS ground state (Equation (4.4)).

In BCS theory, scattering does not affect conduction. A Cooper pair propagates as a whole through the material when a current flows, although it consists of two electrons with equal but opposite momentum. All pairs are locked together and glide at the same speed. The scattering of a pair with a phonon changes the individual momenta of the electrons but the gliding of the pair remains unaffected. Thus a pair state scatters into another pair state. This occurs because there is a very great energy saving for keeping all pairs moving with identical speed [Blu09].

4.2 High-T_c Superconductors

Several classes of superconducting materials have been found. Most prominent are BCS superconductors, obtaining critical temperatures below 40 K, and so-called high-T_c superconductors with $T_c > 40$ K as found in the cuprates and the pnictides. Other non-BCS type superconductors are found in heavy-fermion superconductors, organic superconductors and some special materials as the ruthenates and the alkali-doped fullerenes [Leg07]. An overview of characteristic properties is given in Table 4.1.

	T_c	PG	Symmetry	BCS-type
BCS SC	< 25 K	x	s	✓
MgB_2	39 K	x	s	✓
heavy ions	< 2 K	?	?	x
organic SC	< 12 K	?	?	x
Sr_2RuO_4	$1,5$ K	x	d	x
fullerenes	< 40 K	x	s	✓
cuprates	< 140 K	✓	d	x
pnictides	< 55 K	x	?	x

Table 4.1: *Classes of superconductors and their physical properties [Leg07, HK08, KLK+08].*

4.2.1 General Properties of Cuprates

In 1986, Bednorz and Müller found the cuprate $(LaBa)_2CuO_4$ to be superconducting with a T_c of 30 K [BM86, HHDS08, Lev07]. Shortly after that, the compound $YBa_2Cu_3O_{6+\delta}$ (YBCO) has been found to access the superconducting phase at up to 93 K [WAT+87]. Today, $HgBa_2Ca_2Cu_3O_8$ shows the highest T_c value with 135 K, and even 160 K under high pressure.

Although superconductivity has been expected to occur in cuprates, T_c was suprisingly high. The usage of ytterbium instead of lanthanum leads to higher chemical pressure, which was found to be important for the occurance of superconductivity [Pic89]. All cuprates are ceramics, where a high-temperature annealing in a rich oxygen atmosphere is applied [Pic89]. Pellets, consisting of the initial elements, are thus calcinated in air at high temperatures above 800°C and subsequently homogenized. The resulting material then is quenched [CBG+88].

So far, cuprates are the only materials showing a T_c above the temperature of liquid nitrogen. Unfortunately, the pairing mechanism is still unknown. Due to that lack of theoretical understanding, a method to grow crystals in a size useful for commercial applications is lacking.

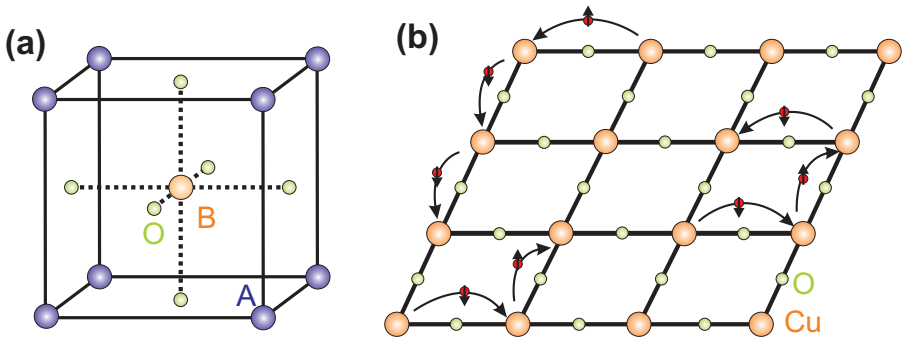

Figure 4.3: *(a) Perovskite structure ABO_3. Atoms of metal A form a cube with metal B in the center, surrounded by oxygen O. (b) The Coulomb interaction blocks electron hopping in a CuO_2 layer. Here, doping with electrons or holes leads to possible charge-carrier hopping.*

Mother Compounds

The mother compounds of the cuprates belong to a class of antiferromagnetic insulating perovskites. These are oxides with ABO_3-structure, A and B denoting metals. Here, A atoms form a cube with a B atom in the center surrounded by an octahedron of oxygen atoms [Blu09] as shown in Figure 4.3(a). These compounds are electrically insulating, due to strong electron-electron interaction. By changing the concentration of the electrons, the cuprate layers become superconducting below a doping-dependent T_c. With stronger doping, the cuprates show metallic behavior and can be described by the Fermi liquid theory (overdoped cuprates) [Leg07].

In general, cuprates exhibit a perovskite structure obtaining CuO_2-layers, with different spacings between these layers. Compounds with different numbers of these layers in each unit cell are known. The electronic structure of these CuO_2 layers leads to a splitting into two small energy bands (upper and lower Hubbard band) with an energy gap of size the U, and E_F in between [Hub63,Czy04]. Due to the $3d^9$ configuration of the copper ions the lower band is filled completely while the upper one remains empty, leading to an insulating phase (Mott insulator) [Mot49,NPK]. Here, each copper atom is in the ground state with d^9 configuration. Hopping of an electron would lead to two neighboring atoms in d^8 and d^{10} configuration, respectively. If the Coulomb repulsion is larger than the hopping energy, the electrons are localized as indicated in Figure 4.3. The spin of the electrons forms a Néel lattice (antiferromagnetic Hubbard insulator) [Hub63].

The complete situation is like a chessboard consisting of antiparallel spins with copper ions located at the corners and oxygen ions along the chains, as presented in Figure 4.3. Between single boards different elements act as spacers.

Superconductivity via Doping

For superconductivity in cuprates, doping via holes is important. Therefore, 3^+ cations are changed to 2^+ cations in the spacing layers. The charge exchange removes electrons from the CuO_2 layers. The remaining holes can move along the chessboards and thus destroy the Néel lattice as shown in Figure 4.3. With a hole-doping of 5%, superconductivity arises and the antiferromagnetic state is destroyed. Thus the superconductivity is a sort of short-circuit in theses materials, because the spacing layers are still normal-conducting. T_c rises with doping concentration δ and reaches a maximum at 16%, to become zero again at about 25%. Higher doping lead to a metallic compound as already mentioned. In terms of the Hubbard model, the doping leads

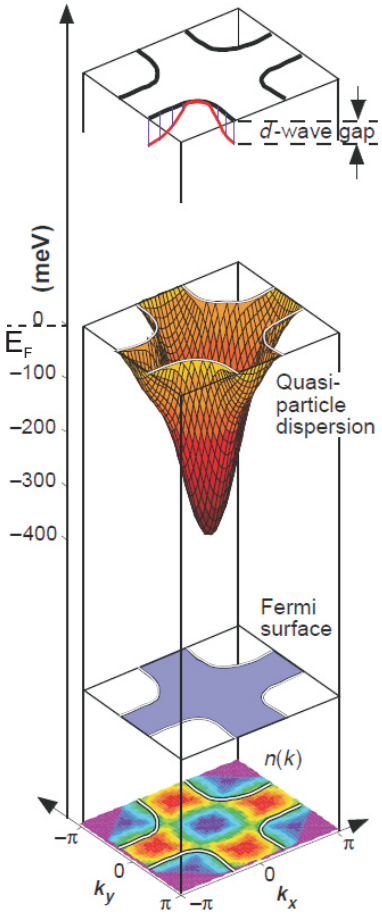

Figure 4.4: *Fermi surface of overdoped BSCCO measured with angle-resolved photoemission (ARPES): bottom panels show the measured relative occupation probability $n(k)$ from which the Fermi surface has been determined. Middle panel shows the obtained quasi-particle dispersion. Top panel displays the mapped Fermi surface together with the d-wave gap in the superconducting state below T_c. Here, the anisotropy in the gap reveals the d-wave character of the gap. Figure taken from [RKF+98].*

to a decrease of E_F into the lower Hubbard band. The doping level δ then is given by a parabolic relation to the critical temperature T_c [TBS+95]:

$$\delta = 0.16 \pm 0.11\sqrt{1 - \frac{T_c}{T_c^{\max}}} \,. \tag{4.7}$$

This also has implications for the preparation process: usually samples are made and subsequently the doping level is calculated from the measured T_c of the sample. Thus, many samples have to be produced to find the maximum value of T_c and a certain δ.

Figure 4.5 shows different possible phase diagrams for cuprates. There are several common features: all phase diagrams exhibit an antiferromagnetic phase at low δ as well as a superconducting dome due to the parabolic relation from Equation (4.7). Another phase is known: the so-called pseudogap phase below a pseudogap temperature T^*. The occurance of such a state is not yet fully understood.

The Fermi surface shows a fourfold d-symmetry located in the CuO_2 layers. Therefore, a phonon-based mechanism should play a minor role, since BCS theory requires s-symmetry (Section 4.1.2) and the pairing electrons are sited on different copper ions [Ohk07]. The d-symmetry also leads a size of Δ_{sc} that is not well-defined.

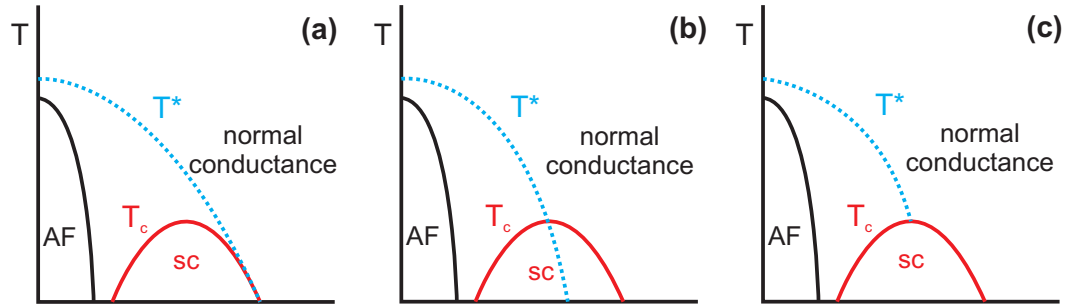

Figure 4.5: *Different possible phase diagrams for cuprates, displaying various phase transition temperatures vs. doping δ. (a) Pseudogap and superconducting gap merge in the overdoped regime. In the so-called one-gap scenario, the pseudogap phase is described in terms of preformed Cooper pairs, that condensate into the coherent state at T_c. (b) Pseudogap and superconducting gap cross each other. In this so-called two-gap scenario, both gaps are of different nature. (c) Pseudogap and superconducting gap meet at T_c and merge, indicating a competing pseudogap phase.*

Non-Controversial Facts

There is still a lack of understanding of the superconducting mechanism in the case of cuprates. Nevertheless, no controversy arises on the following facts proven by experimental evidence:

1. Measurements of the flux quantum and Josephson effects show superconductivity due to Cooper pairs that are spin singlets.
2. Superconductivity occurs in the CuO_2 layers. The pairing is independent of the number of the layers and no pairing between different layers has been observed.
3. The Cu ions are in a spin $1/2$ $3d^9$ configuration with the symmetry of the layers lifting the degeneracy of the d orbitals down to a single $d_{x^2-y^2}$ [HH10].
4. No significant isotropic effect has been found. Thus electron-phonon interaction should be excluded as glue for the Cooper pairs.
5. The coherence length ξ within layers is 1-3 nm and therefore much smaller than in BCS superconductors.
6. A pseudogap phase has been found.

Controversy - the Phase Diagram

In recent years, much effort has been made to combine the description of the superconducting phase, the pseudogap phase and the normal and insulating phase by means of doping properties. Here, improvements in experiment and theory point towards models with two complementary statements [Cho06, HH10]:

1. Hubbard type models that start out at high energies of order U in the eV range, including the pairing mechanism as low-energy antiferromagnetic spin fluctuations and thus as retarded interaction [LNW06, AAHH07, CCG$^+$08].
2. The $t-J$ model [Czy04] at intermediate energies, including pairing as anisotropic momentum space mechanism with the core of the Coulomb interaction orthogonal to the pair wave function enforcing a d-wave gap solution [And07] and thus as instantaneous interaction.

This supports a picture where electron pairing is predominantly magnetic or electronic in nature and phonon interaction plays only a minor role. It is not finally clarified to which extent spin and charge fluctuations contribute via a retarded pairing or exchange coupling via an instantaneous interaction.

Much attention has been paid to the phase diagram, since the correlation of superconducting and pseudogap is still unclear. Three different scenarios have been proposed:

1. Figure 4.5(a) shows the pseudogap to be the origin of the antiferromagnetism and the superconductivity. The electron-electron interaction triggers the pairing at T^*, while the condensation into the coherent state occurs below T_c [Mil06]. Thus one finds preformed Cooper pairs with energy E_{pg}. The condensation then leads to an additional gain of energy E_{sc}.
2. Figure 4.5(b) considers the pseudogap and the superconducting phase as two distinct phenomena on the same Fermi surface. Thus we find two bandgaps with energies E_{pg} and E_{sc}, respectively, independent of each other. Measurements with Angle-Resolved Photo-Electron Spectroscopy favors this two-gap scenario [TLL$^+$06].
3. Figure 4.5(c) shows a scenario where T^* and T_c merge.

Recent far-infrared ellipsometry experiments [DYM$^+$10] are in favor of scenario 3. Here, c-axis conductivity reveals information on Δ_{sc} and Δ_{pg} as well, and the data suggest that Δ_{pg} vanishes close to a critical doping level of $\delta = 0.19$. This may be evidence of a competing pseudogap. Additionally, signatures of a precurser superconducting state have been found. Conclusions concerning the superconducting mechanism have not been drawn. Additional THz transmission measurements will complete this picture.

BSCCO

In 1988, the compound $Bi_2Sr_2CaCu_2O_{8-\delta}$ has been found [CBG$^+$88, MTFA88], also known as BSCCO or Bi2212. It shows a T_c of 92 K and includes no rare earth components. The unit cell is presented in Figure 4.6(a), showing two CuO_2 layers per unit cell. The mother compound obtains the lengths a = 3,817 Å and c = 30,5 Å in x-y- and z-direction, respectively. The energy gaps have been found to be $2\Delta_{\mathrm{pg}} \approx 76$ meV and $2\Delta_{\mathrm{sc}} \approx 41-68$ meV [HTG07]. Here, differences arise from the preparation of the samples in combination with the relation for $\delta(T_c)$ from Equation(4.7). Figure 4.6(b) shows the electronic structure of BSCCO. Here, the strong bonds in the CuO_2 layers as well as the weakly bound BiO_3 layers are likely to be recognized.

4.2.2 Cuprates vs. BCS Superconductors

Finally, the differences between the cuprates and the BCS superconductors shall be analyzed. In both cases, the coherent superconducting phase occurs, formed by Cooper pairs. For the BCS type, the pairing mechanism is based on interaction with lattice vibrations. The resulting coherence length is in the order of 100 nm. The BCS ground state requires s-symmetry and thus metals and alloys mainly show this type of superconductivity. In contrast, the coherence length is just a few nanometers in the cuprates. The superconducting gap shows d-symmetry according to the antiferromagnetic mother compounds, thus interaction with phonons can be excluded as superconducting mechanism. A pseudogap phase occurs above T_c. Whether pseudogap and superconducting gap are competing properties or related to each other has not been clarified so far.

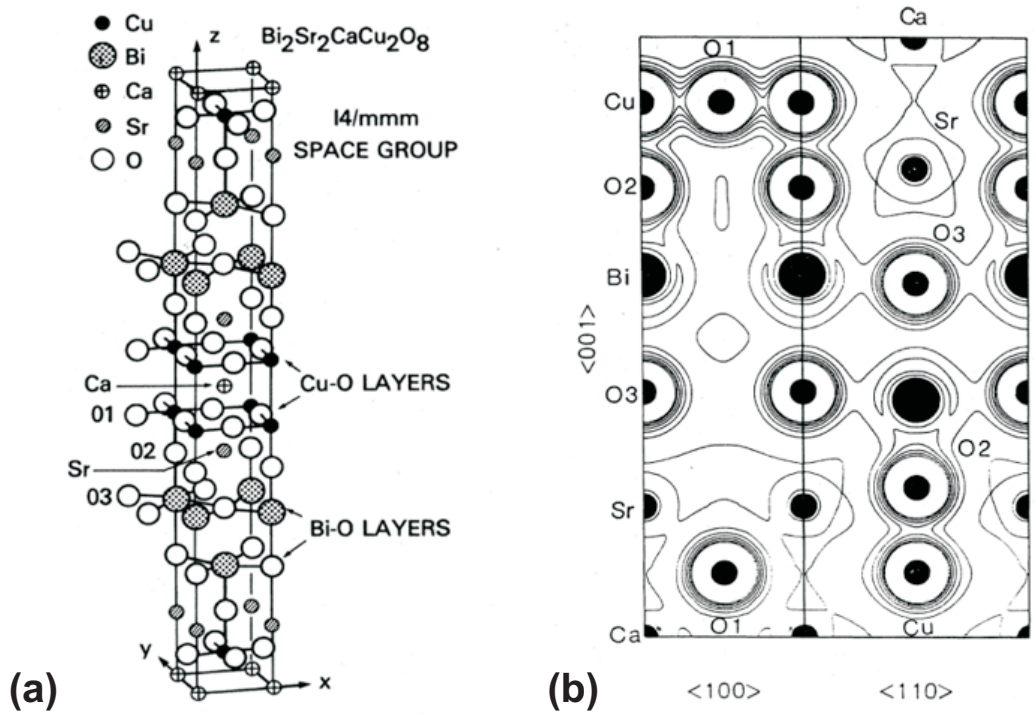

Figure 4.6: *(a) Lattice structure and (b) electronic structure of BSCCO, taken from [Pic89]. Superconductivity occurs in CuO_2 layers, marked by O1. Two CuO_2 layers are found, seperated by different spacing layers. Further description is given in the text.*

4.3 BSCCO at Equilibrium Conditions

The investigation of cuprates has been done by using various different experimental techniques, such as ARPES and optical spectroscopy. ARPES is sensitive to energy and momentum of the electrons and thus reveals band structure information and maps the d-shaped Fermi surface [RKF+98] (see Figure 4.4) as well as the superconducting gap [TLL+06, PLL+07, CRY+10]. In contrast, most optical experiments integrate over the BZ and therefore reveal limited information on the band structure [Bon07, HTG04, HTG07, HTSC07, GCC+09]. Nevertheless, far-infrared ellipsometry reveals the sizes of the energy gaps for different doping levels in YBCO [DYM+10] and find further evidence for a precursor superconducting state below an onset temperature $T_c < T^{\mathrm{ons}} < T^*$.

We make use of THz spectroscopy in the frequency range above 10 THz which is a promising tool for studying high-T_c superconductors because the gap energy of optimally doped BSCCO is $2\Delta_{\mathrm{sc}} \approx 68\ \mathrm{meV} \hat{=} 16$ THz. Therefore, THz spectroscopy is well suited to study low energy excitations of superconductors. Moreover, it allows for a contactless conductivity measurement [KWE+00, ARL+01, CKO+04, KCC+05]. The frequency-dependent measurements on BSCCO are taken for various temperatures and different doping levels. We analyze our data in terms of an optical electron scattering rate, combining the information on absorption and dispersion. The obtained electron scattering rate is found to show significant features that coincide with T_c and T^*. A discussion on consequences for the phase diagram closes this section.

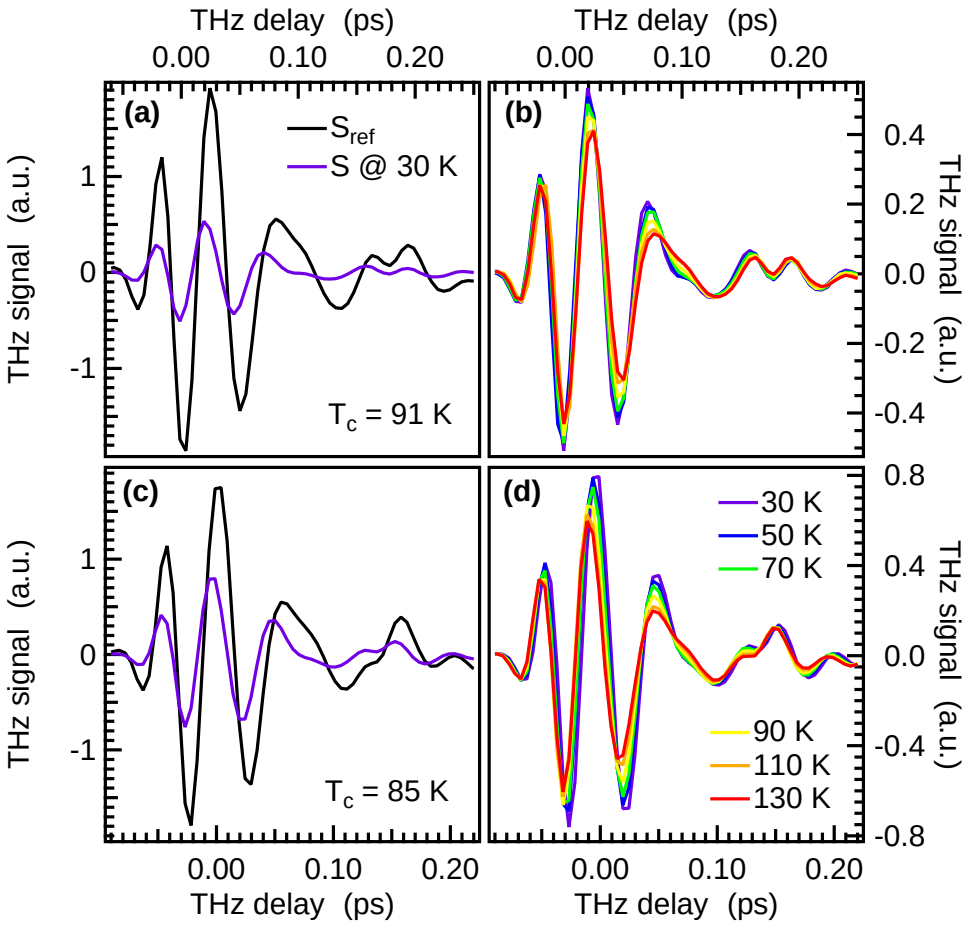

Figure 4.7: *Temperature dependence of the THz transmission for temperatures above and below T_c for two different doping levels. (a) Transmitted THz waveform of sample and reference, respectively, and (b) transmitted THz waveforms between 30 K and 130 K for optimally doped BSSCO with $T_c = 91$ K. (c) Transmitted THz waveform of sample and reference and (d) THz waveforms between 30 K and 130 K for underdoped BSSCO with $T_c = 85$ K. For both samples an increase in absorption with temperature is observed as well as a slight shift in phase.*

Experimental Data

Figures 4.7(a) and (c) show transmitted THz waveforms for two different BSCCO films with $T_c = 91$ K and $T_c = 85$ K together with the reference signals. The measured difference in amplitude is caused by the different sample thicknesses. Figure 4.7(b) shows the transmitted THz waveforms for different sample temperatures below and above T_c in the case of optimally doped BSCCO with $T_c = 91$ K. Here, a change in transmission is found. With increasing temperature, the amplitude decreases. Also changes in the phase are observed mainly at later times. This trend is similar also for different doping levels δ as presented in Figure 4.7(d).

In contrast to graphite, the optical properties of superconductors are usually discussed in terms of the optical conductivity $\sigma(\omega)$. Dielectric function and conductivity are linked to each other by

$$\sigma(\omega) = \frac{\mathrm{i}\omega}{4\pi}\left[1 - \varepsilon(\omega)\right] \ .$$

Here, the real part σ_1 accounts for the absorption whereas the imaginary part σ_2 quantifies (along

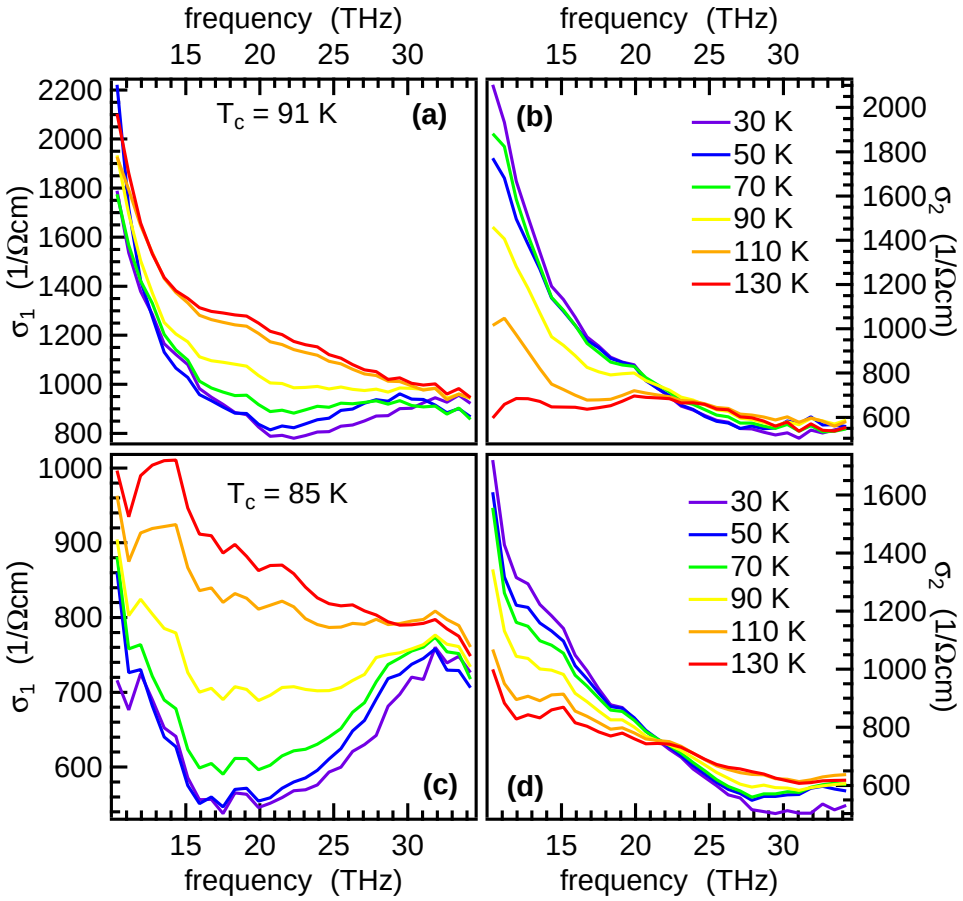

Figure 4.8: *Frequency dependence of the optical conductivity for temperatures above and below T_c for two different doping levels. (a) Real part $\sigma_1(\omega)$ and (b) imaginary part $\sigma_2(\omega)$ for optimally doped BSSCO with $T_c = 91$ K, (c) real part $\sigma_1(\omega)$ and (d) imaginary part $\sigma_2(\omega)$ for underdoped BSCCO with $T_c = 85$ K. Here, the absorption part $\sigma_1(\omega)$ shows an increase with temperature that can be understood in terms of the gap. Additionally, the dispersion part $\sigma_2(\omega)$ shows a temperature dependence below the gap energy $2\Delta \cong 18$ THz. Above 2Δ it remains virtually constant.*

with σ_1) the phase shift between $\boldsymbol{E}$ and $\boldsymbol{j}$. Again, the thin-film formula was applied, leading to the conductivity shown in Figure 4.8. Panels (a) and (c) show $\sigma_1(\omega)$ for two different δ and various sample temperatures. As was seen in the transmitted THz waveforms, a decrease in the absorption is observed below T_c for lower frequencies. At higher frequencies only small changes are found as has been reported by [vdMMZ$^+$03, BT05, CKO$^+$04] whereas at frequencies below 11 THz the Drude contribution dominates the response [LNW06]. Figures 4.8(a) and (b) also show, that the decrease in absorption is not sharp neither in the frequency domain at $2\Delta_{sc}$ nor the temperature domain at T_c.

Figures 4.8(b) and (d) show the corresponding changes in phase. At higher frequencies no significant changes are observed, while a strong decrease with temperature for frequencies below the corresponding gap energies takes place. This is due to the changes previously observed in the THz transient. Additionally, a crossing point is observed at about 22 THz that shifts slightly towards lower frequencies with decreasing δ.

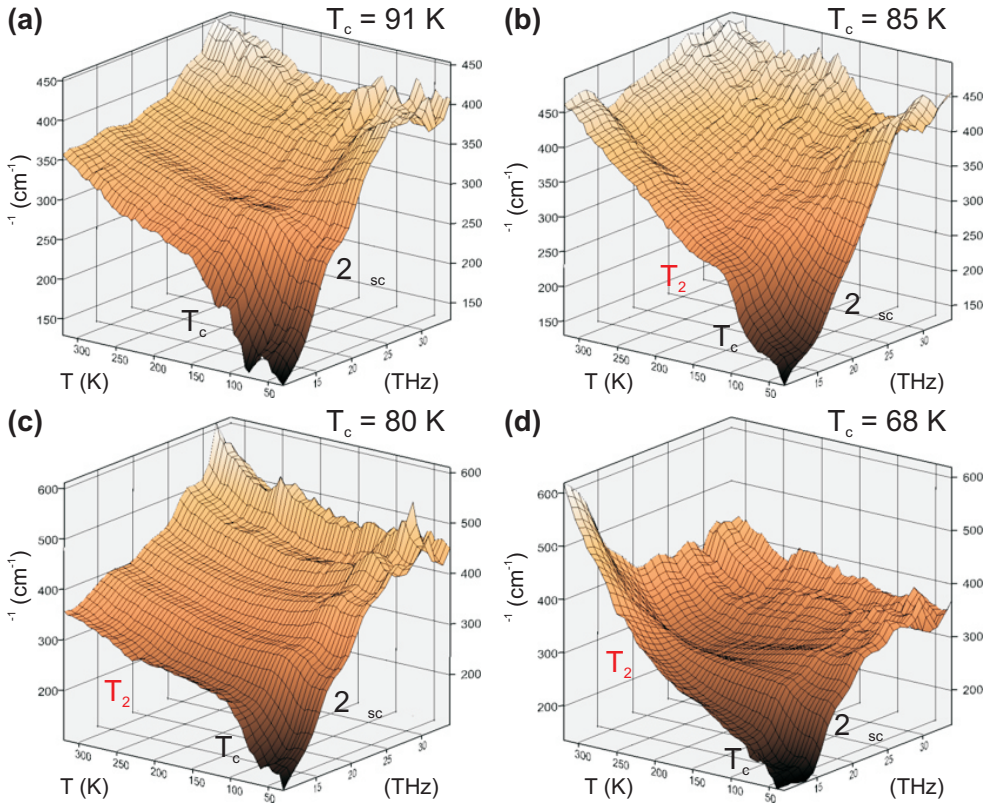

Figure 4.9: *Temperature and frequency dependence of the electron scattering rate τ^{-1} for BSCCO with different doping levels. (a) Optimally doped with $T_c = 91$ K, (b) underdoped with $T_c = 85$ K, (c) underdoped with $T_c = 80$ K, (d) strongly underdoped with $T_c = 68$ K. For all doping levels, similar behavior is found: Below T_c and 2Δ, a valley is formed. At T_c and 2Δ, respectively, an abrupt rise occurs followed up by an slow increase.*

Much effort has been devoted to model the optical conductivity in order to understand the mechanism of superconductivity [HPS93]. So far, qualitative and quantitatve agreement has been reached only in the vicinity of the superconducting phase transition $T \cong T_c$. Here, a combination of amplitude and phase information is given by the electron scattering rate τ^{-1}, [BT05]. It represents the imaginary part Σ_2^{op} of the optical single-particle self-energy $\Sigma^{\mathrm{op}}(\omega) = \Sigma_1^{\mathrm{op}}(\omega) + \mathrm{i}\Sigma_2^{\mathrm{op}}(\omega)$ [HTG04] and thus is accessible by theoretical calculations [QTK$^+$99, HTG07]. Here, a Drude-like description is convenient [QTK$^+$99]:

$$\tau^{-1}(\omega) = \frac{\omega_{\mathrm{pl}}^2}{4\pi} \mathrm{Re}\left(\frac{1}{\sigma(\omega)}\right) . \tag{4.8}$$

Figure 4.9 displays the resulting temperature- and frequency-dependent electron scattering rates at four different doping levels. All curves provide similar slopes: at low temperatures as well as low frequencies, a structural low plateau is observed, followed up by a distinctive step that can be associated with the superconducting phase transition. Excitation energy and temperature are due to 2Δ and T_c as will be disussed below. Cuts are applied to investigate the temperature dependence as well as the frequency dependence. Results for the temperature domain are shown in Figures 4.10 (a) and (b) for two different δ. Both panels account for the frequency range below 14 THz. A step-like feature occurs at $T_1 = T_c$ due to the superconducting gap for all doping levels considered. This step is linked to the previously observed changes in σ_1 and σ_2 and can be explained by the opening of a gap of 2Δ below T_c.

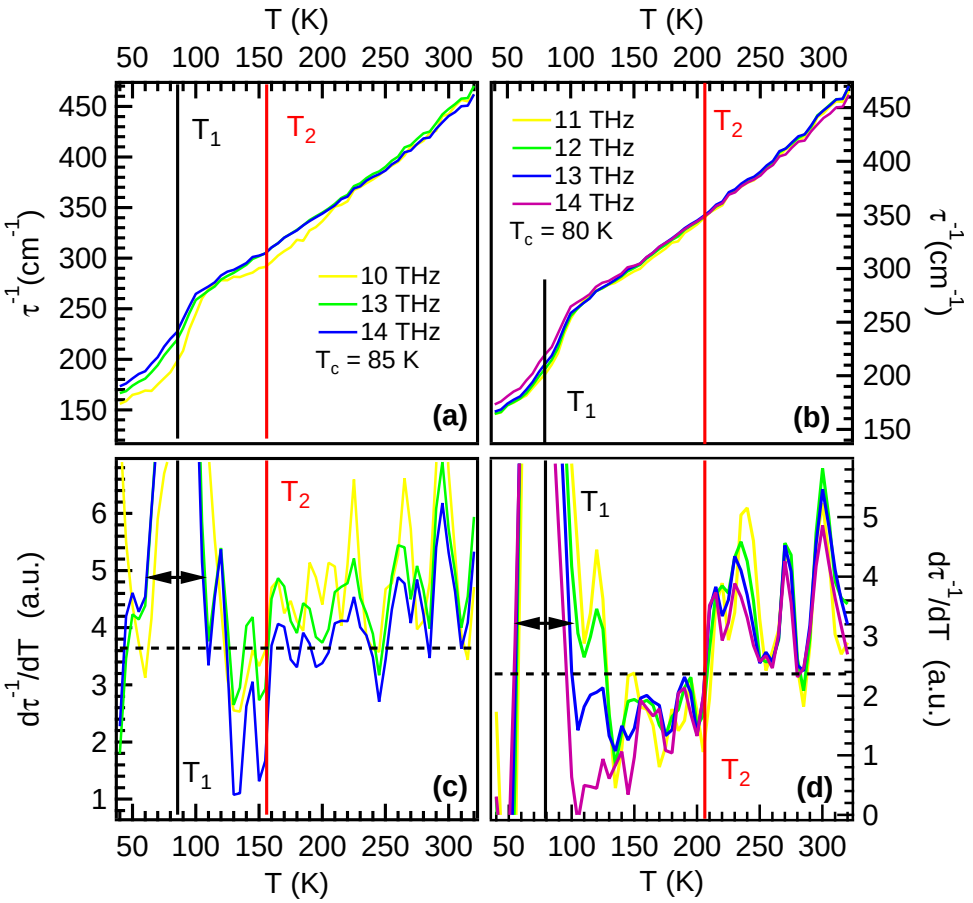

Figure 4.10: *Temperature dependence of the electron scattering rate at two different doping levels of BSCCO: (a) $T_c = 85$ K and (b) $T_c = 80$ K and at various photon energies below the gap energy. The superconducting phase transition can be adressed to T_1, while a kink at T_2 can be guessed only. (c) and (d) Derivative of the measured curves of (a) and (b). Here, T_1 and T_2 are derived from the marked significant changes.*

An interpretation of these observations is as follows: the electron scattering rate shows a significant decrease at T_c due to the occurance of blocked states, that undermine scattering events. Below T_c the scattering rate remains virtually constant on a lower level, indicating the opening of the superconducting band gap. However, there is no sharp transition, neither in temperature (see Figure 4.10) nor in the frequency range (see Figure 4.8). This may be caused by the d-wave gap character, leading to a not well-defined size of Δ_{sc}, and the contribution of the normal conducting spacers between the superconducting CuO_2-planes to the conductivity. For the latter, another indicator is the existing offset in conductivity and the still high values of τ^{-1} below T_c. It is known, that unpaired electrons rule the MIR response of BSCCO [BT05, HTSC07, QTK+99]. Here, the decrease is found to be in the order of $1/3$. Additional simulations have been done previously by [HPS94] for the microwave regime, confirming the interpretation of a band gap opening.

Evaluation of the Transition Temperatures

Previously obtained measurements and simulation mainly focussed on the frequency dependence in the vicinity of T_c [QTK+99, CSH+91, HTG07, RSC+91, RSC+92, vdMMZ+03, HPS94] or

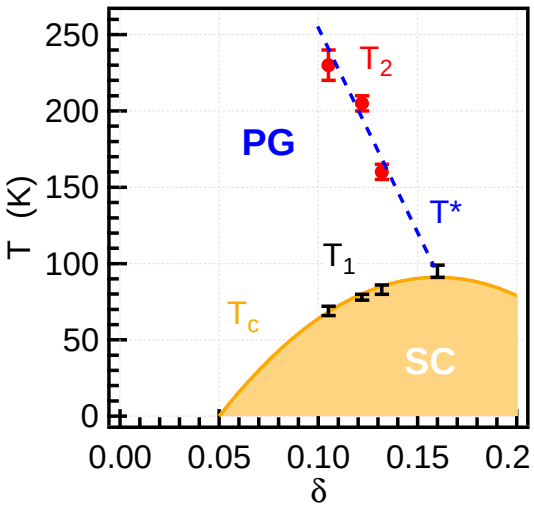

Figure 4.11: *Phase diagram with temperatures T_1 and T_2 as were obtained from the electron scattering rates. The superconducting dome (T_c) was calculated from Equation (4.7), the pseudogap phase (T^*) corresponds to [NPK]. Here, T_1 and T_2 match T_c and T^*, respectively. For optimal doping no T_2 has been found, indicating that superconducting phase and pseudogap phase merge at $T_c^{\max}$.*

the temperature dependence of Δ_{pg} [DYM+10]. In contrast, measurements performed here are done on a broad temperature range showing a narrow grid. Besides the step-like feature at temperatures T_1, the obtained curves exhibit an additional kink (bending) at temperatures $T_2 \gg T_1$, showing also a dependence on the doping level (see Figure 4.9). We may assign this particular feature at T_2 to the pseudogap at T^* since both temperatures match each other as will be investigated in detail below.

To extract the temperatures T_1 and T_2 more precisely it is usful to investigate the temperature derivative $\partial\tau^{-1}/\partial T$. This is done by choosing an appropriate numerical method [Hol]. In order to evaluate small changes with less noise in the derivative, several neighboring points were included. This procedure is enabled by the narrow temperature grid and the high-quality data. In addition, this was applied to different THz frequencies, obtaining similar curves. Results are presented in Figures 4.10(c) and (d) for different frequencies below $2\Delta_{\mathrm{sc}}$. The common result shows a peak at T_1 (corresponding to T_c) due to the step-like feature and an additional step for the kink at T_2. This is marked in Figures 4.10(c) and (d). In combination with the curves for τ^{-1}, one can address temperatures T_1 and T_2 to both features, since no dependence on the excitation energy is observed within a certain doping level δ. The temperature T_1 was extracted from the curves of Figures 4.10(a) and (b) by evaluating the mean value from the broading of the step and from Figures 4.10(c) and (d) by evaluating the mean value from the broadening of the peak. The temperature T_2 was extracted from the step in temperature derivative.

From the frequency dependence, it is also possible to evaluate the gap energy $2\Delta_{\mathrm{sc}}$ due to the clear phase transition. Values agree with literature and show the expected shift to lower frequencies with deceasing δ. For $2\Delta_{\mathrm{pg}}$ no indicator is found in the frequency dependence. Hence, an estimation of the pseudogap energy from the electron scattering rate seems not to be possible by only considering the frequency dependence [DYM+10]. Thus, the temperature dependence and its relation to the phase diagram will be exploited in detail below.

Discussion

The resulting values for T_1 and T_2 are displayed in a phase diagram in Figure 4.11 showing the measured transition temperatures as function of the doping δ. For optimally doped BSCCO no T_2 value was extracted, since both features in the curves occur at once. In addition the superconducting dome is plotted, as a result from Equation 4.7. Here, experimentally obtained T_1 match the theoretical curve for T_c, while the measured T_2 values match the pseudogap temperatures T^* as found with other experimental methods [HHDS08]. Here, the favorite scenario as result from

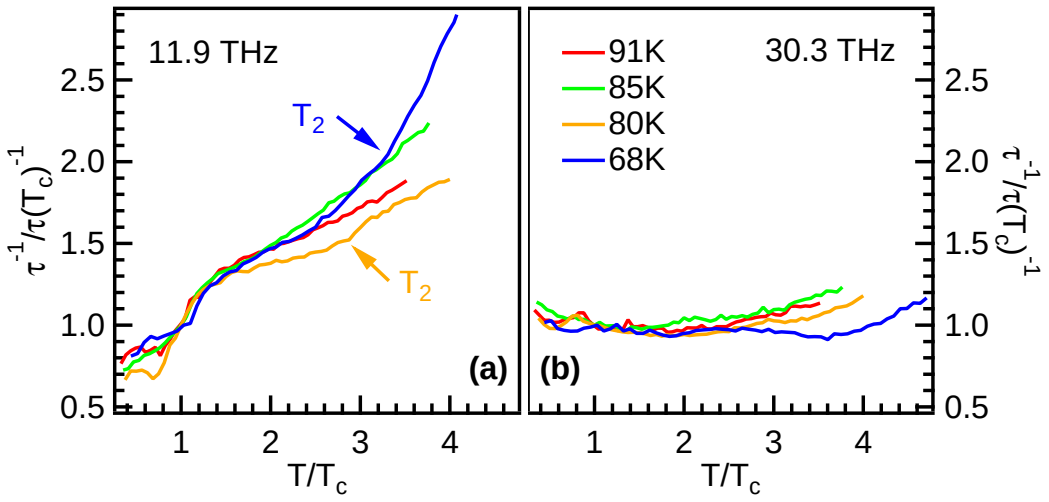

Figure 4.12: *Temperature dependence of the normalized electron scattering rate for BSCCO with different doping levels showing a T_c ranging from 68 K to 91 K to different excitation energies. (a) $\tau^{-1}(T)/\tau^{-1}(T_c)$ at an excition energy of 49 meV (11.9 THz) below the gap energies for all dopings, (b) for an excitation energy of 124 meV (30.3 THz) above the gap energies.*

THz-transmission measurements is the merging of superconducting and pseudogap at $T_c^{\max}$ (see Figure 4.5(c)).

It is interesting to normalized τ^{-1} to its value at T_c as a function of T/T_c. Here, the superconducting phase transition is observed for optical excitation energies $\hbar\omega = 49$ meV below $2\Delta_{\mathrm{sc}}$ as presented in Figure 4.12(a). Additionally, the kink (bending) is observed at higher temperatures T_2 especially for $T_c = 68$ K and $T_c = 80$ K. Also the doping-dependence is seen from these curves, finding lower T_2 for higher transition temperatures as previously in Figure 4.10. Investigating τ^{-1} at excitation energies $\hbar\omega = 124$ meV significantly higher than $2\Delta_{\mathrm{sc}}$, as presented in Figure 4.12(b), a step at T_c is not observed. Those large frequencies are insensitive to the smaller superconducting gap. The bending at higher temperatures can still be found, however much smaller than at lower frequencies. This indicates a larger pseudogap with $\Delta_{\mathrm{pg}} > \Delta_{\mathrm{sc}}$. A consistent model, describing the optical conductivity in the superconducting and the normalconducting phase is not available so far. The found results from the electrons scattering rate can be interpreted as follows.

On the one hand, an explanation for the slope above T_c might be provided in terms of preformed Cooper pairs [HHDS08]. Above T^*, the electron scattering rate τ^{-1} shows a strong increase with temperature. This is flattened between T^* and T_c. Since unpaired electrons rule the temperature dependence of τ^{-1}, here, the presence of preformed Cooper pairs reduces the temperature dependence. Scattering then occurs by breaking up pairs into quasi-particles. At T_c these Cooper pairs then condense into the coherent state, leading to a virtually constant τ^{-1}. In addition, the observed dependence on the temperature below T^* may also be a result of the normal conducting electrons in the spacing layers.

On the other hand, one would expect both gaps to close on the overdoped site if the pseudogap phase is a precursor for superconductivity [DYM+10], i.e. T_c and T^* should merge at zero and not at $T_c^{\max}$, the top of the superconducting dome in Figure 4.11. The found scenario by THz spectroscopy as well as far-infrared ellipsometry suggests, that both gaps do not share the same

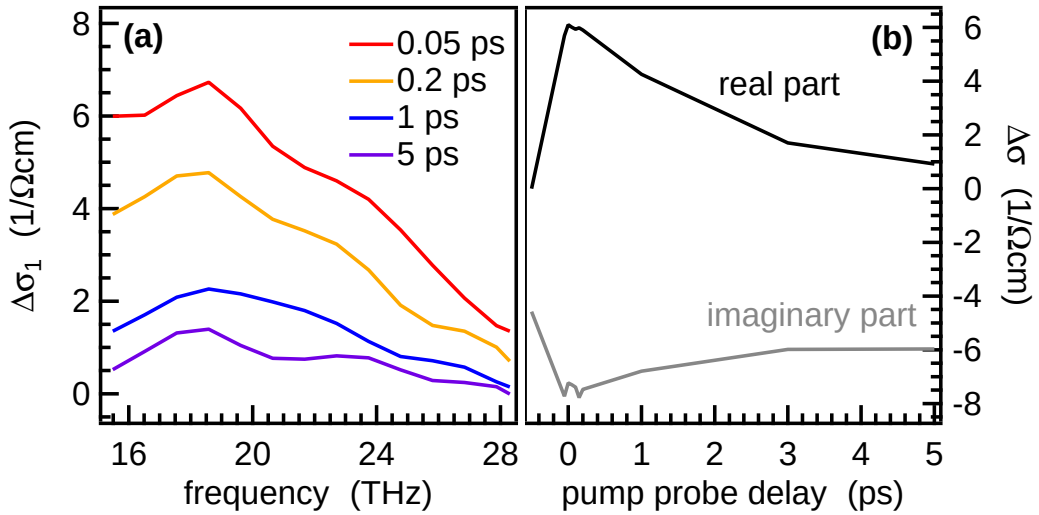

Figure 4.13: *(a) Photoinduced changes to the absorption $\Delta\sigma$ of BSCCO with $T_c = 91$ K at a sample temperature of $T_a = 30$ K for various pump probe delays. (b) Photoinduced changes to the real and the imaginary part of $\Delta\sigma$ as a function of the pump probe delay at a frequency of 15.5 THz below 2Δ. An initial increase in absorption due to quasi-particle emission is found that agrees with [CKO+04].*

electronic states, since they do not just add up to spectroscopic gap. However, both phases seem to be linked to each other.

Summary

Temperature and frequency dependent measurements on BSCCO for different doping levels were performed, leading to the conductivity and the electron scattering rate. These quantities show very similar temperature and frequency dependence. The superconducting phase transition can be seen clearly, which allows us to extract T_c. In addition, a doping-dependence bending in the temperature domain is observed, that is assigned to the pseudogap at T^*. A theoretical description including the whole temperature range has not been provided so far. The observed presumably pseudogap contribution can be partially understood in terms of preformed Cooper pairs. Unfortunately, no overdoped samples were available. Here, THz measurements would provide additional information due to the merging of superconducting gap and pseudogap.

4.4 Photoexcited BSCCO

Pump-probe measurements have also been performed on the BSCCO samples. The measured changes in the conductivity are presented in Figure 4.13. Panel (a) shows the changes in absorption vs. frequency to different times after photoexcitation. Here, the pump-probe delay $\tau = 0$ ps was fixed at the maximum of the pump-induced changes. A large increase in absorption is found immediately after photoexcitation, that decreases to later times on a picosecond timescale (see Figure 4.13(b)). At higher frequencies the found increase in absorption becomes smaller. This behaviour may be explained by the filling of the spectral gap as has been found for the equilibrium data (see Figure 4.8(a)). In Figure 4.13(b) also $\Delta\sigma_2(\tau)$ is shown. Here, a decrease after photoexcitation is observed. This also corresponds to the equilibrium case (seen in Figure 4.8(b)).

The observed increase in absorption is understood in terms of an ultrafast depletion of the con-

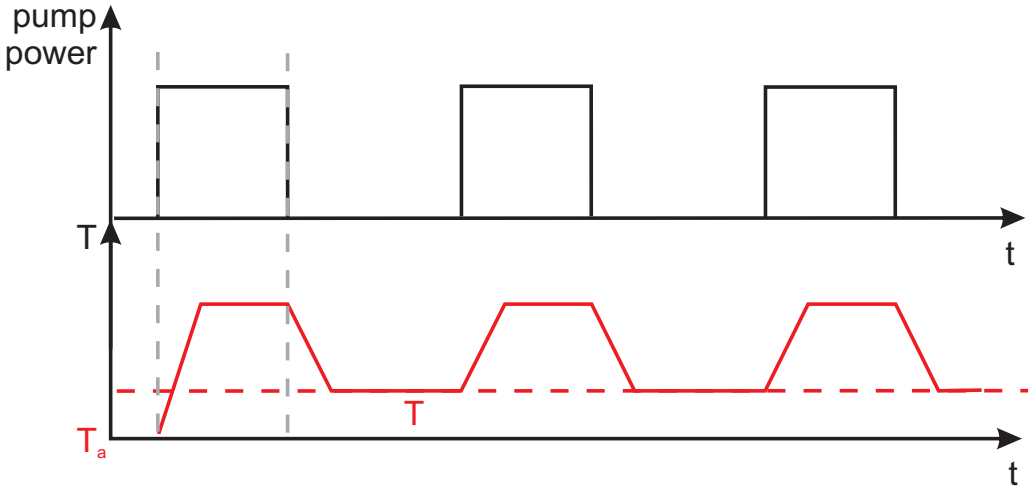

Figure 4.14: *Pump-probe scheme for the pump power and the sample temperature. The pump pulse excites the sample. After blocking of the pump pulse, the sample thermalizes to a higher temperature* $T_a + \Delta T$.

densate and a concurrent increase of the number of quasiparticles (ultrafast phase transition). The recovery is found on a picosecond timescale and thus similar to YBCO, where a decay of 3.7 ps was observed [PPB$^+$10]. Measurements previously obtained at THz frequencies far below the gap energy (< 3 THz) [CKO$^+$04, KCC$^+$05] also show the increase in absorption but a slower decay. Unfortunately, more accurate modeling (as e.g. done for graphite in Section 3.3) is difficult as a theory for the THz response of equilibrium and photoexcited cuprates is still missing. Nevertheless, the strong modulation of the THz optical properties are promising for MIR photonics.

4.5 Temperature Modulation Spectroscopy

Besides the changes of the optical properties after photoexcitation, attention was also paid on PP-scans. These measurements reveal two different kinds of information:

1. an immediate change of the signal after photoexcitation followed up by a relaxation with decay times dependent on the sample temperature. This has been used previously [Sch08] to estimate the transition temperature T_c.

2. prior to photoexcitation a signal at delays $\tau < 0$ is observed because the sample is not fully recovered but thermalized.

Thus, PP-scans to delays $\tau < 0$ contain information on the equilibrium response of the sample. This is used for a comparison with the previoulsy obtained $\partial\tau^{-1}/\partial T$ from Section 4.3.

In pump-probe experiments, a delay of 12 ns between the measurement of the perturbed and unperturbed sample can be found (see Section 2.1.1), caused by the repetition rate of the Ti:Sapphire oscillator. By this time, the sample is not fully recovered, thus at negative pump-probe delays $\tau < 0$, a difference signal $\Delta S_{\tau<0} = S(T_a+\Delta T) - S(T) \neq 0$ is expected, due to a quasi-equilibrium temperature $T_a + \Delta T$ with $\Delta T \ll T_a$. This situation is schematically shown in Figure 4.14. Expansion to first order yields

$$\Delta S_{\tau<0} = S(T_a + \Delta T) - S(T_a) = \frac{\partial S(T_a)}{\partial T}\Delta T \,.$$

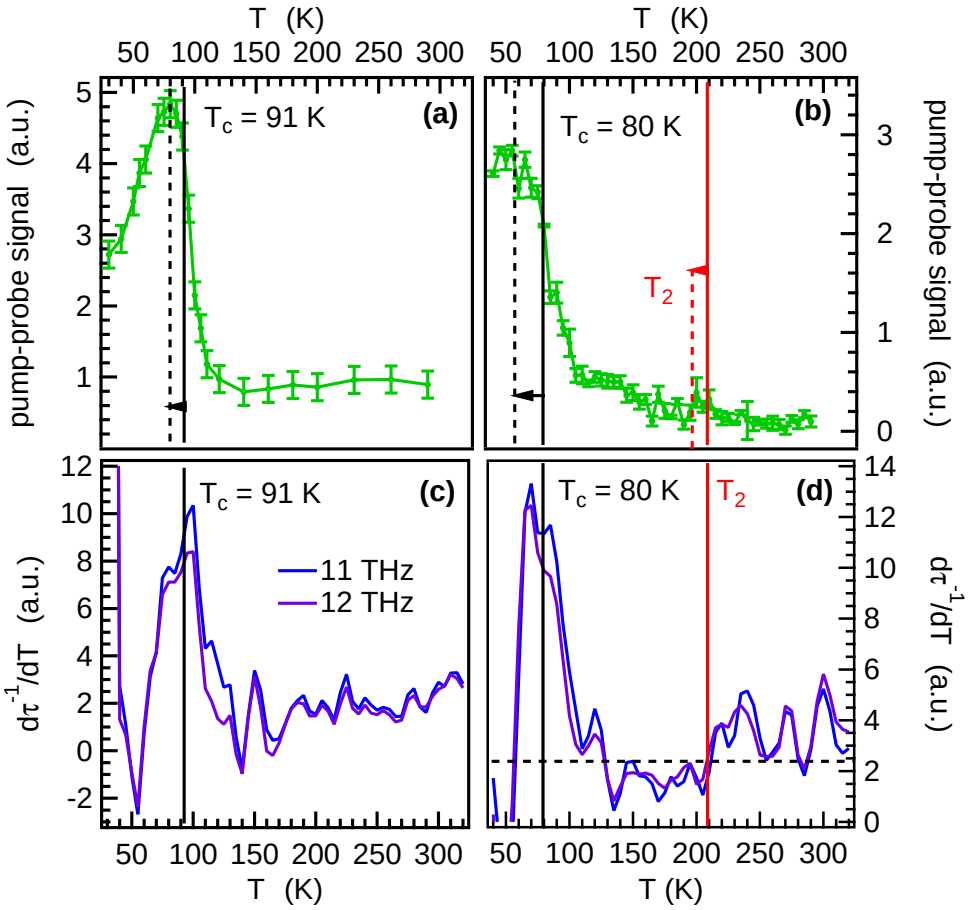

Figure 4.15: *Temperature dependence of the difference signal* $\Delta S_{\tau<0} = S(T_a + \Delta T) - S(T) \neq 0$ *for negative pump-probe delays* $\tau < 0$. *(a) Optimally doped BSCCO with* $T_c = 91$ *K and (b) underdoped BSCCO with* $T_c = 80$ *K. Panels (c) and (d) show the temperature derivative of the electron scattering rate measured on the same samples.*

Here, the change ΔT is expected to depend on the sample temperature T_a via e.g. the specific heat c_e.

Figure 4.15 displays the obtained curves for optimally doped and underdoped BSCCO in panels (a) and (b) together with equilibrium data obtained by the temperature derivative of the electron scattering rate (panels (c) and (d)). Above T_c, the resulting curves remain constant at a low level. At T_c, a peak occurs showing a broad maximum as previously found for T_1. A peak-shift to lower temperatures is observed, caused by the change ΔT.

Above T_c, the obtained curves remain virtually constant (errors result from the mean values obtained from different delays $\tau < 0$ as well as a different number of repeated runs on the same sample). Unlike in $\partial\tau^{-1}/\partial T$, the occurance of $T_2 = T^*$ is not clearly observed (see Figure 4.15(d)). This may be caused, by the different origin of both quantities. The electron scattering rate τ^{-1} includes information on phase and absorption via σ_1 and σ_2 and has been exploited at THz frequencies below the energy of the superconducting gap. In contrast, the pump-probe signal ΔS is integrated over all THz frequencies and mainly sensitive to the changes in absorption

$\Delta\sigma_1$. Thus, it seems resonable that τ^{-1} is more sensitive to the pseudogap, since it includes the complex conductivity. The superconducting phase transition is observed in both cases, since it has large impact on the absorption.

In conclusion, pump-probe experiments are useful to obtain complementary data for the measurements of equilibrium properties. Both static and quasistatic measurements require a long-term stability of the experimental setup. An advantage are the complementary sources for errors in the measurements that may cancel each other out. Equilibrium measurements are prone to instabilities in the laser performance and slight changes in the sample quality, e.g. thickness. Pump-probe measurements in contrast, require a narrow grid of temperatures and must be corrected for a temperature shift. This can be done from the prominent peak found at T_c in both experiments. Therefore a combination of both, THz transmission experiments and NIR-pump THz-probe experiments improve the quality of the data.

4.6 Summary and Outlook

Temperature-dependent THz-transmission measurements on the cuprate BSCCO have been performed in the frequency domain for four different doping levels. Here, from the electron scattering rate the superconducting gap energy can be evaluated as well as T_c. This is possible because the superconducting coherent state leads to a strong decrease in absorption. The measured values correspond to ones, previously obtained by other techniques. In addition, evidence for a second phase transition has been found, that may be related to the pseudogap phase. A comparison to previous measurements confirms this interpretation.

Photoexcitation leads to an ultrafast depletion of the superconducting gap as indicated by an increased absorption immediately after photoexcitation. This effect depends on frequency and shows a decay on a picosecond timescale. Quasi-equilibrium optical properties can also be measured by applying pump-probe technique. This may be a source for complementary information for the equilibrium measurements.

Consequences for the phase diagram have been discussed, since a doping dependence for the second phase transition has been found. In agreement with measurements for the gap energies, the critical temperature of the superconducting phase transition and the pseudogap temperature merge at $T_c^{\max}$. This is not understood in terms of a precurser superconductivity by the pseudogap phase.

A deeper understanding of the cuprate superconductivity may be provided by compairing this results to similar experiments performed on BCS superconductors. Here, MgB_2 is well-suited due to its high transition temperature. First results will be presented in Chapter 5. Especially, differences in the conductivity as well as the electron scattering rate above T_c should reveal information on the pseudogap phase since such behavior has not been found for BCS type superconductors.

Chapter 5

Magnesium Diboride

In 2001 magnesium diboride was found to be superconducting below a critical temperature of 39 K [NNM+01]. Besides the remarkably high transition temperature, that makes it possible to achieve the superconducting phase by closed-cycle refrigerators instead of LHe, MgB_2 is a simple compound of two inexpensive elements instead of rare earth metals as used in cuprate superconductors [CC03]. Further investigation showed magnesium diboride to be a BCS superconductor [QLYT02] with two gaps and thus two distinct superconducting coherent states [CKI01].

This chapter presents first THz-transmission measurements on MgB_2 thin films on silicon and diamond substrates, respectively. The measured optical conductivity and electron scattering rate will be discussed in terms of sample preparation with special interest on the achieved T_c on different substrates. Further interest is given to a compairison of BCS and cuprate superconductors.

5.1 Properties of Magnesium Diboride

5.1.1 General Remarks

Magnesium diboride has been known for a long time. Therefore, the discovery of superconductivity was somehow surprising. It is also a very simple compound and consists of inexpensive elements. Due to the transition temperature of 39 K there is no need for cooling with liquid helium. Furthermore, a critical field of more than 30 T makes MgB_2 interesting for applications at high magnetic fields. Additional a low surface resistivity was found [JKK+05, JDK+06], promising applications in planar circuits and passive microwave devices.

5.1.2 Electronic and Phononic Properties

Electronic and phononic properties of MgB_2 were studied using various experimental techniques [UTS+03, HJ03, LLC+08] as well as by theory [CCL03, MA03]. MgB_2 has a simple AlB_2 structure with graphite-like hexagonal boron layers separated by layers of hexagonal close-packed magnesium atoms. The crystal structure is presented in Figure 5.1(a). Thus, this structure may be regarded as that of completely intercaleted graphite with carbon replaced by boron. Furthermore, magnesium diboride is formally isoelectronic to graphite. Again, only s and p electrons are involved in the electronic structure. As in graphite, the intralayer bonds are shorter than the interlayer bonds. Here, only a factor of 2 occurs, whereas graphite shows a factor of 2.4. This enables significant interlayer hopping [MA03].

Contrary to graphite, MgB_2 shows an incomplete filling of the two σ bands corresponding to strongly covalent sp^2-hybrid bonding within the boron layers. The holes at the top of these σ bands show two-dimensional properties and are localized within the boron sheets. In contrast to

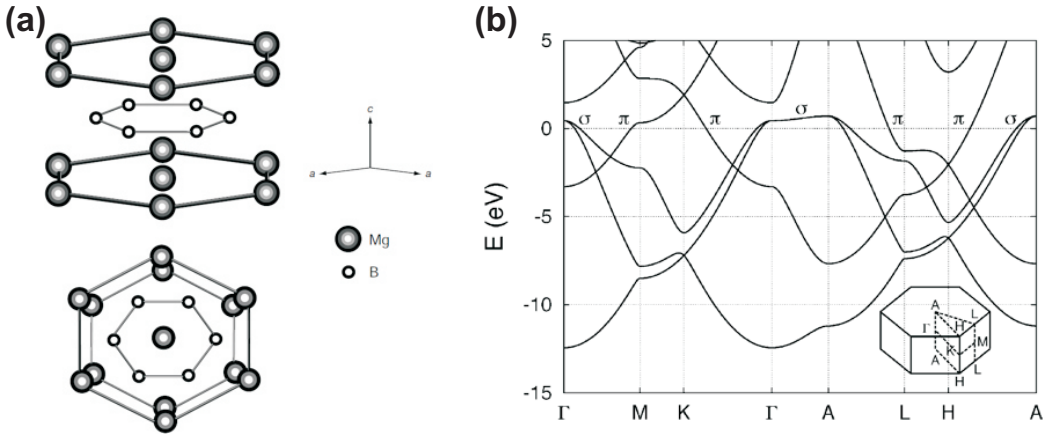

Figure 5.1: *(a) Crystal structure of MgB_2 showing its hexagonal layered structure. Taken from [NNM+01]. (b) Electronic structure of MgB_2, showing the hole-like σ and the electron-like π bands. Taken from [CCL03].*

σ bands, three-dimensional electrons and holes occur in the π bands, which are delocalized over the whole crystal [HJ03]. These two-dimensional covalent and three-dimensional metallic states contribute almost equally to the eDOS at E_F, while the unfilled covalent bands experience strong interaction with longitudinal phonons in the boron layer [MA03]. The calculated band structure is shown in Figure 5.1(b).

Four zone center optical phonon modes have been found [HJ03, KDJA01, BHR01]:

- $\mathrm{B_{1g}}$: two B atoms move out-ouf-plane in opposite directions, $E_{\mathrm{B_{1g}}} = 40 - 43\ \mathrm{meV}$,
- $\mathrm{A_{2u}}$: Mg and B planes move out-of-plane in opposite directions, $E_{\mathrm{A_{2u}}} = 48 - 53\ \mathrm{meV}$,
- $\mathrm{E_{1u}}$: Mg and B planes move in-plane in opposite directions, $E_{\mathrm{E_{1u}}} = 64 - 75\ \mathrm{meV}$,
- $\mathrm{E_{2g}}$: B atoms move in-plane in opposite directions, $E_{\mathrm{E_{2g}}} = 86 - 89\ \mathrm{meV}$.

The calculated phonon dispersion together with the corresponding DOS is shown in Figure 5.2. The calculated EPC is found to be strong for the $\mathrm{E_{2g}}$, while there is only small coupling to the other optical phonon modes.

5.1.3 MgB_2 as Two-Gap BCS Superconductor

The first measurements of the isotope effect revealed the importance of the EPC for Cooper pairing in MgB_2. T_c shifts by 1 K when ^{11}B is substituted for ^{10}B [BLP+01]. Also for magnesium an isotopic effect can be measured. Suprisingly, the substitution of ^{24}Mg for ^{25}Mg produces almost no shift in T_c. These results suggest a highly selective EPC.

From Equation (1.10) one finds, that the gap depends on three parameters: the characteristic phonon energy $\hbar\omega_D$, the eDOS $D(E_F)$ and the EPC W_0. While phonon energies are rather high but comparable to other compounds and the eDOS is relavely low because MgB_2 has no d-electrons, the EPC must be the source for the remarkably high T_c. Here, the two nearly noninteracting bands of different dimensionality and the band's specific EPC have to be considered.

In MgB_2, the high energy $\mathrm{E_{2g}}$ optical phonon mode has a strong EPC to the two-dimensional σ band. The strong coupling of the boron motion to the σ states originates from the covalent nature

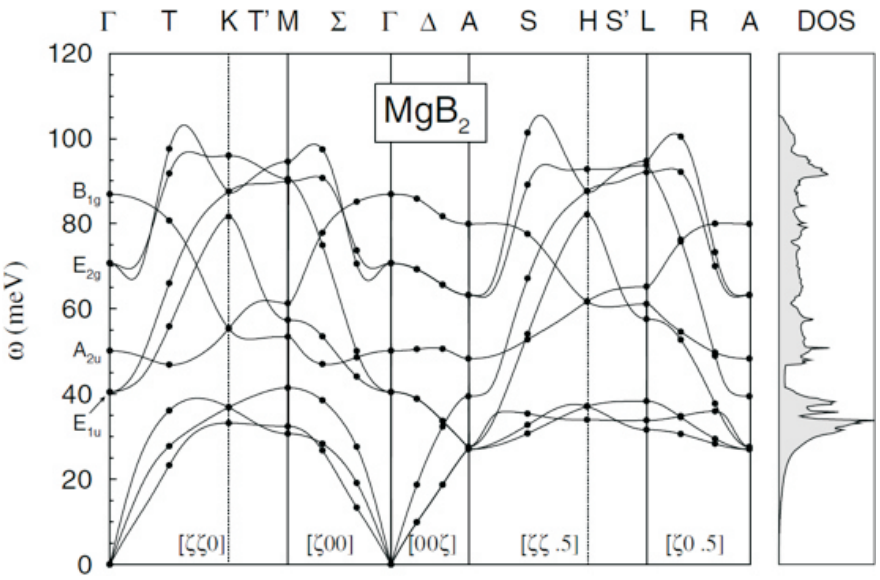

Figure 5.2: *Phonon dispersion relation for MgB_2 with optical phonon modes labeled, and phononic density of states (DOS) taken from [BHR01]. Here, the E_{2g} phonon modes shows highest phonon energies up to* 0.1 *eV.*

of the σ band, where the charge is concentrated along the B - B direction. Thus, when boron atoms move in-plane, the charge must redistribute significantly to accomodate the change. This distortion shifts the energy of the electronic states and accounts for the large EPC. Because it affects the conducting electrons, the $\mathrm{E_{2g}}$ mode has a large impact on the superconducting properties of MgB_2 [YGL$^+$01].

Already in the first month after the discovery of superconductivity in magnesium diboride, experiments appeared that where inconsistent with a conventional BCS scenario, even though the EPC pointed toward this [YGL$^+$01]. It was observed, that specific heat measurements are easier to explain if two gaps are assumed instead of one [BWF$^+$01]. In fact, two distinct gaps appear associated with σ and π Fermi surfaces. This two-gap model then was applied to EPC calculations performed separately for the two sets of bands [MA03].

The strong EPC in the two-dimensional σ bands and weak EPC in the three-dimensional π bands lead to this striking qualitative feature of superconductivity in MgB_2: the simultaneous existence of two energy gaps in the same material. Such model has been proposed before [SMW59, BBHB80], but MgB_2 is the first example in which this effect is so dramatically expressed. In MgB_2, the two bands and the two very different sized gaps are quite distinct and manifest themselves clearly [TYK$^+$01]. The two gap sizes [TYK$^+$01,UTS$^+$03] have been evaluated to:

1. larger gap: $\Delta_1 = 5.6\ \mathrm{meV}$,
2. smaller gap: $\Delta_2 = 1.7\ \mathrm{meV}$.

Both gaps close at T_c. The smaller gap appears in the π bands, while the larger gap is associated with the σ bands [CKI01, TSS$^+$01].

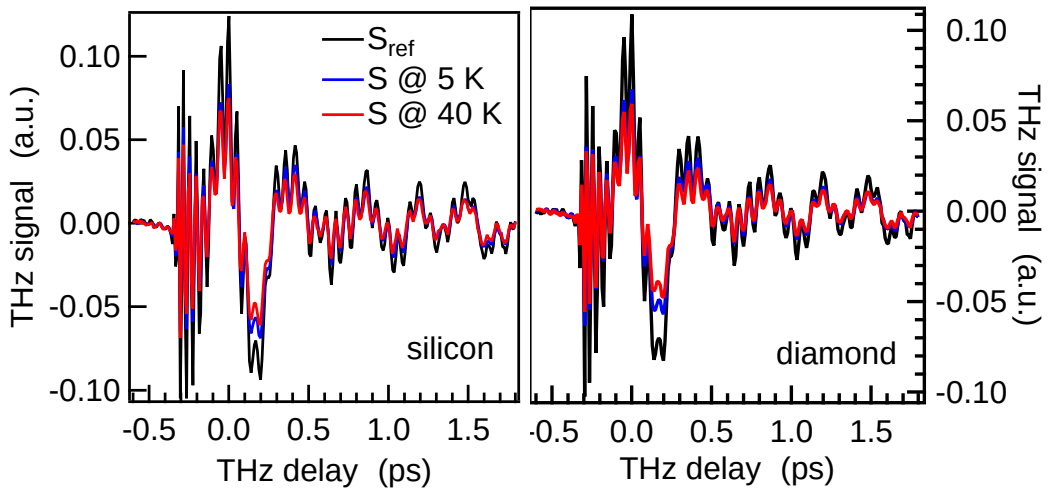

Figure 5.3: *Transmitted THz waveforms below and above T_c for both substrates: (a) Silicon substrate, (b) Diamond substrate. For both samples a significant change in absorption is observed.*

5.2 THz Measurements on MgB_2 Thin Films

THz-transmission measurements have been performed with thin MgB_2 films in the low frequency range (0.8 to 4 THz), with photon energies corresponding to the gap sizes. In order to optimize the sample preparation process, several substrates and thicknesses were used. The sample preparation was done in a collaboration at Universität Bielefeld, Department of Physics - Thin Films and Physics of Nanostructures [FTMT10]. Here, first results from 30 nm thick MgB_2 samples grown on silicon and diamond substrates are presented. They show that the samples are superconducting on both substrates. The transition temperature can be evaluated from the data as well as the energy of the larger band gap. Additional DC measurements revealed a T_c of 20 K. A comparison to the cuprates closes this chapter.

5.2.1 Experimental Results

Raw Data

Figure 5.3(a) shows THz waveforms transmitted through the MgB_2 sample on a silicon substrate. A GaP crystal was used to generate THz radiation below 4 THz. Also THz radiation with higher frequencies was generated as can be seen from the raw data. However, this information was not used in data evaluation, since it reveals no further insights for the superconducting phase transition. The chosen sample thickness seems to be adequate for transmission measurements. The THz-pulse duration is found to be in the range of 1 ps in the low frequency range. The THz waveforms for two sample temperatures above and below T_c are displayed. Again, as in the case of the cuprates, a change in transmission is observed, leading to an increase in absortion at higher temperatures. This can be understood in terms of the opening of a superconducting gap, as was presented in detail in Section 4.3.

Figure 5.3(b) shows THz waveforms transmitted through the MgB_2 sample on a diamond substrate. Except slight changes due to the substrates transmission all findings are similar to the sample on the silicon substrate.

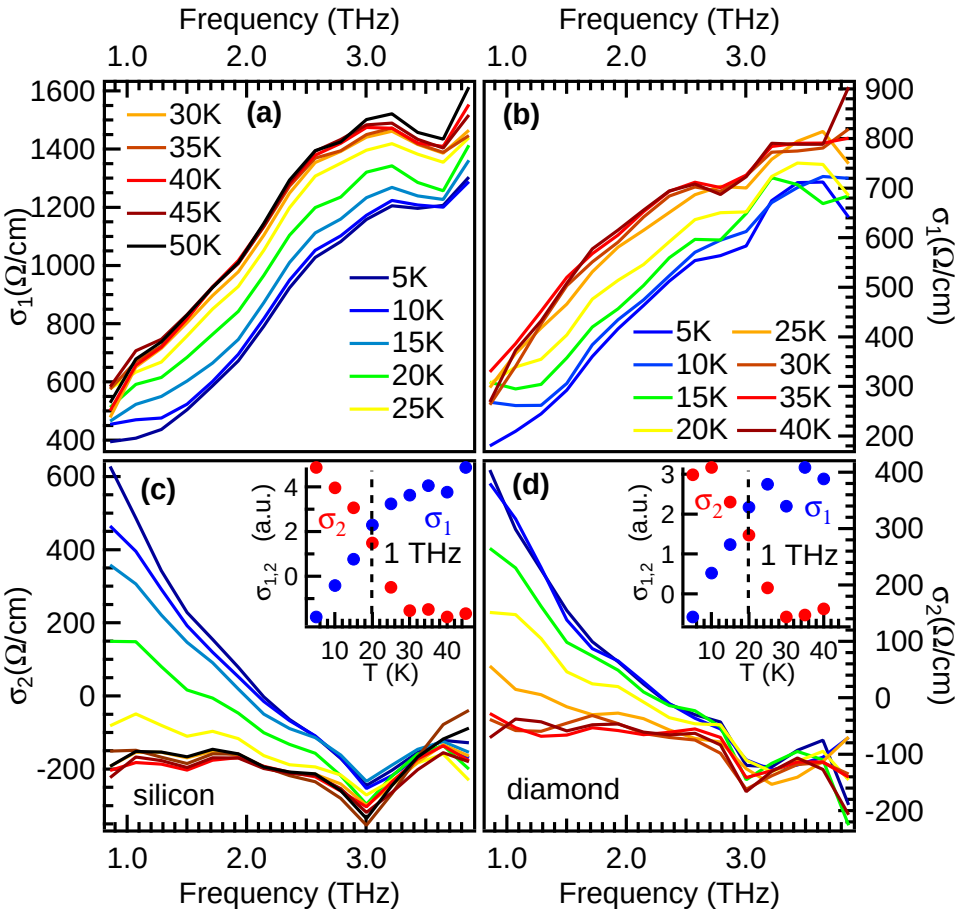

Figure 5.4: *Temperature dependence of the optical conductivity for both MgB_2 samples, on silicon and diamond substrates, respectively. Real parts σ_1 for (a) the silicon substrate and (b) the diamond substrate. Both show a large increase at $T = 20$ K, found to be the transition temperature for both samples. Imaginary parts σ_2 for (c) the silicon substrate and (d) the diamond substrate. A decrease for low excitation energies is observed resulting in a virtually constant σ_2 above T_c. Insets show real (blue) and imaginary parts (red) of the conductivity vs. temperature at a frequency of 1 THz.*

Optical Conductivity

The optical conductivity has been evaluated similar to the cuprates as presented in Section 4.3. Figure 5.4 presents the temperature dependence of the real and imaginary parts of the optical conductivity in the frequency domain for both substrates. Since no qualitative changes can be observed due to the substate the conductivity will be discussed by neglecting the substate. The real part σ_1, represents the absorption site of magnesium diboride. It increases with temperature as expected from the raw data. In contrast to the cuprates a clear increase in a small temperature range around T_c is found. Above and below this intervall the conductivity remains almost constant. The imaginary part σ_2, represents the phase information. Here, a large shift with temperature below T_c is observed. Above the critical temperature σ_2 remains almost constant. In contrast to the cuprates, σ_2 changes sign below T_c, while it shows negative values above T_c.

The insets in Figures 5.4(c) and (d) show the values of both real and imaginary part of σ at a frequency of 1 THz as a function of temperature. In both cases a clear transition is observed.

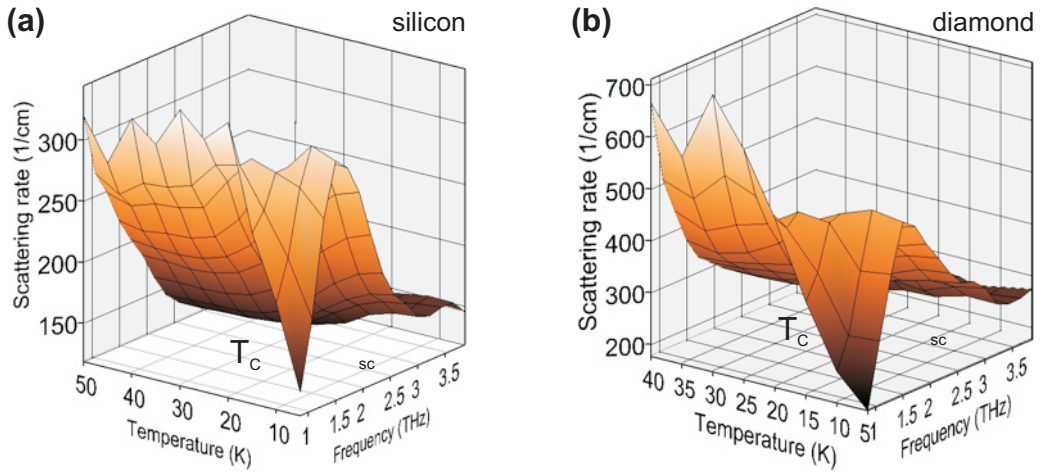

Figure 5.5: *Temperature and frequency dependence of the electron scattering rate τ^{-1} for both substrates, (a) silicon and (b) diamond, respectively. Both show an abrupt rise due to the superconducting phase transition, followed up by a decease in the frequency domain.*

From the slopes, T_c can be evaluated. Both samples show a critical temperature of $T_c = 20$ K. As in the case of the cuprates, the mean value of the broadening of the step was used.

These findings are in good agreement with previous results [PDJ+03, KCO+02, ODC+08]. Here usually small single crystals have been applied or instead, thick epitaxial films ($d \approx 200$ nm) to reduce the optical effect of the substrates.

Electron Scattering Rate

As previously in Section 4.3, the electron scattering rate τ^{-1} has been derived from the conductivity data (Equation (4.8) [BT05]). The curves obtained are displayed in Figure 5.5. The electrons scattering rate shows the same frequency dependence and the same trend in the temperature dependence for both substrates.

In the frequency domain a step is observed at temperatures below T_c followed up by a strong decrease with increasing photon energy. At temperatures above T_c this step does not appear. Figure 5.6(a) shows the frequency dependence at three different temperatures below T_c. From the step in the curves (note that the lower limit of the frequency range is 0.8 THz), the gap energy may be estimated: the step appears at $\nu = 1.2 \pm 0.3$ THz. This corresponds to an energy of $2\Delta_{\mathrm{exp}} = 4.9 \pm 1.23$ meV and thus is in agreement with the larger gap $\Delta_1 = 5.6$ meV, if one consideres a smaller gap size due to the lower T_c. As expected from BCS theory, this value decreases at temperatures close to T_c, here seen for $T = 15$ K.

Figure 5.6(b) shows the temperature dependence of the scattering rate for frequencies below and close to $2\Delta_{\mathrm{exp}}$. Here, the closing of the superconducting gap can be seen clearly: while at $\nu = 0.8$ THz $= 3.3$ meV a step associated to the phase transition is found, this is not the case at $\nu = 1.2$ THz $= 4.9$ meV, where τ^{-1} is almost constant.

Again, an interpretation in terms of the band gap opening can be given. At T_c, electrons condensate as Cooper pairs into the superconducting state and do not contribute to the scattering rate anymore. Therefore, a sharp decrease in the electron scattering rate at the transition temperature

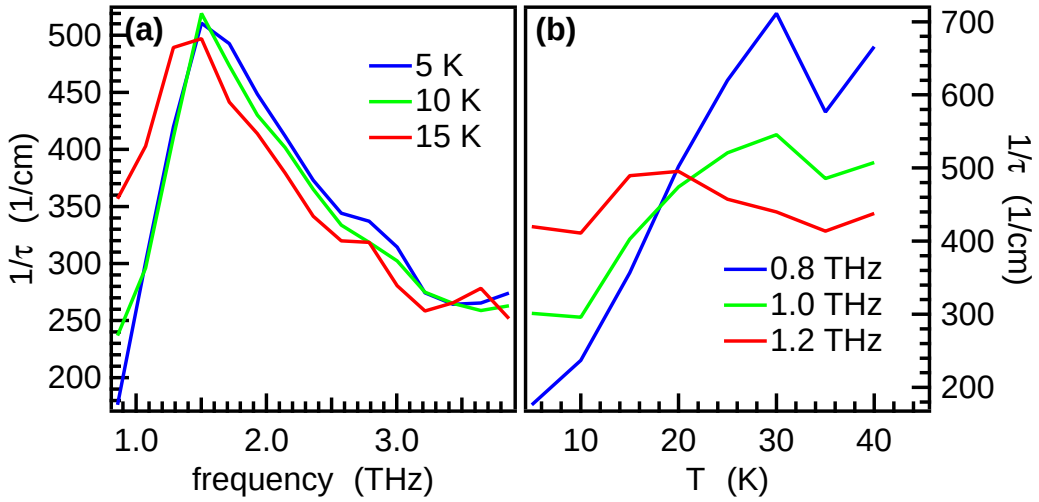

Figure 5.6: *(a) Frequency dependence of the electron scattering rate measured for the sample on diamond substrate for different sample temperatures below T_c, showing the rise at $2\Delta_1$. (b) Temperature dependence of the electron scattering rate for different frequencies, indicating the closing of the superconducting gap above 1.2 THz.*

characterizes the superconducting phase transition.

For all measured temperatures, the frequency dependence of the electron scattering rate shows a decrease with increasing frequency immediately after $2\Delta_{\mathrm{exp}}$. This is in contrast to the cuprates. Here, τ^{-1} increases further (for BSCCO: see Figure 4.9). This difference may be related to the existence of the pseudogap in cuprate superconductors.

5.2.2 Comparison between Cuprates and MgB_2

As in the case of the cuprates, the electron scattering rate has been normalized to it value at T_c and plotted vs. T/T_c. This is displayed for photon energies above and below the gap energy in Figure 5.7 in combination with the corresponding curves measured on optimally doped BSCCO with a T_c of 91 K.

In both cases, the measured data agree with each other in the considered temperature range. Below the gap energy, a larger step in the case of MgB_2 is found, leading to lower τ^{-1} values below T_c. Here, the s-type superconducting phase plays an important role, since virtually all electrons participate to the coherent state. This is not the case for the cuprates: here, superconductivity occurs only in the CuO_2 layers, while the remaining normally conducting electrons in the spacing layers are simply short-circuited [Pic89]. Above T_c, for MgB_2 the trend is not clear. It seems that τ^{-1} remains virtually constant, while for BSCCO the electron scattering rate shows a further increase. Here, the temperature range has to be increased in further measurements.

For excitation energies above the gap energy, no step appears in both cases and τ^{-1} remains constant. This indicates the normal conductance in both materials.

Altogether, the measurements on both, BCS-superconductors and cuprates show several differences but also similarities. A step-like feature appears in the electron scattering rate at T_c as well as 2Δ, that has to be found more pronounced in the BCS-superconductor. Photon energies above 2Δ lead to a flat τ^{-1}. The frequency dependence shows a significant difference for photon ener-

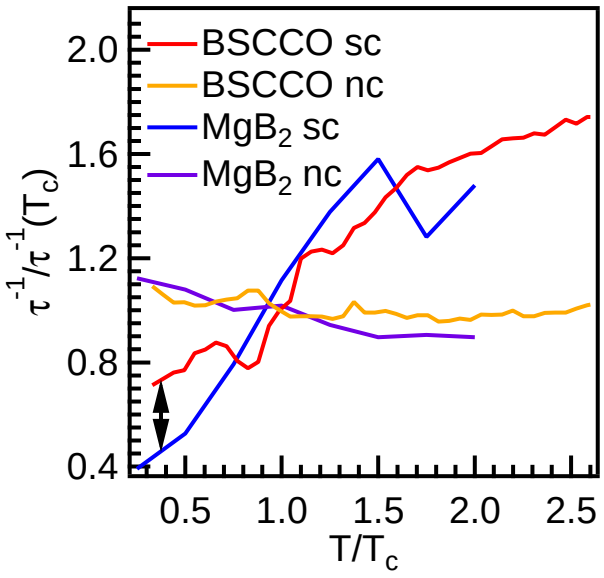

Figure 5.7: *Compairison of the normalized electron scattering rate of MgB_2 to BSCCO with $T_c = 91$ K for excitation energies above and below the superconducting gap. Both materials reveal similar behavior, while MgB_2 shows a significant larger decrease of τ^{-1} in the superconducting phase.*

gies above the gap energy. For cuprates τ^{-1} shows a further increase, while in the BCS case an opposite trend has been found.

Conclusions concerning the pseudogap phase cannot be drawn due to the limited information on the temperature behavior and the low frequency resolution in the low THz frequency range. Here, the experiment has to be improved in further measurements.

In case of magnesium diboride, no pump-probe measurements have been attempted. For the used experimentel setup the pump-fluence would decrease significantly due to the required larger pump-focus, which would be necessary, because the THz focus on the sample is much larger at lower THz frequencies. In addition, the temporal resolution would decrease due to the longer THz-pulse length. However, VIS-pump THz probe experiments have been done by [DAT+03, DAT04]. Here, similar behavior to the cuprates has been found, showing a slower recovery of the superconducting condensate on a 100 ps timescale.

5.3 Summary and Outlook

THz-transmission is a powerful tool to measure the sample quality and thus T_c of superconductors contactlessly. Here, the frequency range has to match the size of the superconducting gap. Hence, the focus has been on magnesium diboride, due to its high T_c and the gap size corresponding to about 1 THz. Thin films were prepared in a collaboration on finally two different substrates, silicon and diamond, respectively. Due to the lattice mismatch between MgB_2 and the substrates, both samples show a smaller T_c than usual. Nevertheless, superconducting MgB_2 samples on diamond and silicon have been prepared and characterized by THz transmission experiments for the first time.

The obtained data for optical conductivity and electron scattering rate have been compared to the findings from the cuprate BSCCO. Both show clear significance for the superconducting gap in phase and absorption. The BCS superconductor MgB_2 shows a sharp transition, while the effect seems to be smeared out in BSCCO. Above T_c the measurements of the electron scattering rate indicate differences for both superconductors. This may be related to the occurance of the pseudogap phase in the cuprates. Here, further measurements have to be done, especially

for BCS-type superconductors. Therefore, the resolution in frequency and temperature must be improved.

The performed experiments show MgB_2 to be a good material for THz-transmission measurements, due to its gap size of about 1 THz and its high T_c. Measurements on a broader temperature range should reveal the differences between BCS-type and cuprate superconductors more clearly. Experiments in the normal conducting phase of magnesium diboride than can be compared to the pseudogap phase as well as the antiferromagnetic and normal conducting phase in cuprates. Additional time-resolved measurements on MgB_2 would lead to information on quasi-particle dynamics. One may think of excitation with energies in the NIR as well as the THz range. Here, the advantage is the computability of the samples response for BCS superconductors [PAK07, PKA08, PKA09]. This also enables a comparison with non-equilibrium states of the cuprates. To perform time-resolved measurements on BCS superconductors, further improvements in the experimental setup have to be made. Especially time and frequency resolution have to be improved.

Summary

Terahertz spectroscopy was used to investigate the THz optical properties of graphite and the superconducting materials $Bi_2Sr_2CaCu_2O_{8+\delta}$ and MgB_2 following thermal heating or excitation with a femtosecond laser pulse. These materials are promising candidates for applications as THz-optical switches or modulators.

In graphite, a decrease in the optical absorption with temperature is found in the covered spectral range from 12 to 26 THz. This behavior is explained by the blocking of direct optical transition due to the population of normally unoccupied states by thermally excited electrons. This effect is partially compensated by indirect optical transitions that represent additional absorption channels at higher temperatures. In this context, an increase of the plasma frequency and the Drude scattering rate with rising temperature is observed, which can be traced back to the strongly varying eDOS of graphite around the Fermi energy.

Similar to thermal heating, photoexcitation of graphite leads to a bleaching at frequencies above 15 THz. At low temperatures, this effect becomes significantly larger than at room temperature because thermally excited electrons play only a minor role in the sample response. After photoexcitation, the electrons thermalize on a femtosecond timescale as expected for metals. Whereas the plasma frequency is found to be completely determined by the instantaneous electronic temperature, the Drude scattering rate is also sensitive to the ambient temperature. Theoretical calculations show that the excitation energy per electron is much higher at low temperatures, resulting in higher electronic temperatures immediately after photoexcitation.

Within 0.5 ps after photoexcitation, few strongly coupled optical phonon modes have reached thermal equilibrium with the electrons, while the remaining phonon modes are still cold. On a picosecond timescale, these hot phonon modes scatter with low-energy acoustic phonons. This decay becomes faster at higher ambient temperatures.

The cuprate superconductor $Bi_2Sr_2CaCu_2O_{8+\delta}$ and the BCS superconductor MgB_2 show a significant decrease of the absorption below the superconducting transition temperature. This is explained by the opening of the superconducting bandgap. A close-mesh of measured temperatures reveals a feature that can be interpreted as the critical temperature of a pseudogap phase in $Bi_2Sr_2CaCu_2O_{8+\delta}$. Here, the behavior of the electron scattering rate in the pseudogap phase might be explained by preformed Cooper pairs. In contrast to that interpretation, the phase diagram derived from our data shows the pseudogap phase to exist only in the underdoped regime. This favors the interpretation that pseudogap and superconducting phase are of competing order. For $Bi_2Sr_2CaCu_2O_{8+\delta}$, photoexcitation below T_c leads to an increase in absorption due to quasiparticle excitation. In addition, photoexcitation can be used to modulate the sample temperature, which yields the temperature derivative of the THz conductivity.

MgB_2 thin films have been grown on THz-transparent substrates, showing a T_c of 20 K. Here, the transition temperature T_c and the gap energy have been measured contactlessly. THz-conduct-

ivity measurements of this BCS superconductor enable a comparison to other superconducting compounds. In MgB_2, the normalized electron scattering rate decreases to significantly lower values below T_c than in $Bi_2Sr_2CaCu_2O_{8+\delta}$. This behavior points to a participation of almost all electrons to the coherent state in MgB_2.

To summarize, graphite's optical properties show a significant temperature dependence. The response after photoexcitation is also highly sensitive to the ambient temperature. Thus graphite is a promising material for photonic devices. In addition, the energy relaxation was found to be more effective at higher temperatures. This must be taken into account in future applications that require fast relaxation of a THz-optical switch or modulator. In cuprates, superconducting phase and pseudogap phase are found to be of competing order. Further insights are expected from measurement on overdoped samples.

Appendix A

Quantities and Abbreviations

A.1 Quantities

$\hat{A}$, $\boldsymbol{A}$, $\bar{\bar{A}}$	operator, vector, tensor A
$\hat{b}$, $\hat{b}^\dagger$	annihilation and creation operator for bosons
b	Bose distribution
$\hat{c}$, $\hat{c}^\dagger$	annihilation and creation operator for fermions
D	eDOS; thickness of substrate
d	thickness of sample
f	Fermi distribution
$\boldsymbol{k}$	electronic wavevector
m, M	electron and ion mass
N	refractive index; number of ions
n	band index
N_e	number of electrons
$\boldsymbol{P}$, $\boldsymbol{p}$	momentum of ions and electrons
Q	quotient of sample and reference signals
$\boldsymbol{q}$	phononic wavevektor
R	response function
$\boldsymbol{R}$, $\boldsymbol{r}$	displacement of ions and electrons
S	signal
T^*	pseudo gap temperature
T_a	ambient temperature (sample temperature)
T_c	critical temperature
T_e	electronic temperature
Γ	Drude scattering rate; parameter in SWM
γ	decay rate
Δ	SWM parameter; order parameter for SC
δ	doping level
ε	dielectric function
σ	conductivity
Σ^{op}	optical single-particle self-energy
τ^{-1}	electrons scattering rate
τ_{p}	decay time
ω_{pl}	plasma frequency

A.2 Abbreviations

ARPES	Angle-Resolved Photo-Electron Spectroscopy
BSCCO	$Bi_2Sr_2CaCu_2O_{8+\delta}$
BZ	Brillouin Zone
CM	Chirped Mirror
DFG	Difference Frequency Generation
DFT	Density Functional Theory
DOT	Direct Optical Transition
ECDC	External Cavity Dispersion Control
eDOS	electronic Density Of States
EELS	Electron Energy Loss Spectroscopy
EM	End Mirror
EPC	Electron-Phonon Coupling
E_F	Fermi energy
FM	Focussing Mirror
GVD	Group Velocity Dispersion
HOPG	Highly Oriented Pyrolytic Graphite
HTSC	High-T_c Superconductor
interDOT	Direct Optical Transition between different electronic bands
intraDOT	Direct Optical Transition in one electronic band
IR	Infrared
IOT	Indirect Optical Transition
LA	Longitudinal Acoustic phonon mode
LHe	Liquid Helium
LIA	Lock-In Amplifier
LN	Liquid Nitrogen
LO	Longitudinal Optic phonon mode
MIR	Mid-Infrared
NIR	Near-Infrared
OC	Output Coupler
OR	Optical Rectification
PG	Pseudogap
PM	Parabolic Mirror
SCOPs	Strongly Coupled Optical Phonons
SFG	Sum Frequency Generation
SC	Superconductor
SWM	Slonczewski-Weiss-McClure model
TA	Transversal Acoustic in-plane phonon mode
TO	Transversal Optic in-plane phonon mode
Xtal	crystal
YBCO	$YBa_2Cu_3O_{6+\delta}$
ZA	Transversal Acoustic out-of-plane phonon mode
ZO	Transversal Optic out-of-plane phonon mode

Appendix B

Measurement of Sample Thickness

Sample thicknesses of graphite and BSCCO have been measured by transmission of visible light. A HeNe laser ($\lambda = 632.8$ nm, $E_{\mathrm{h}\nu} = 2$ eV) in combination with a photodiode have been used to measure the ratio of sample and reference transmission.

B.1 Data Evaluation

The basics of the data evaluation is almost the same as presented in Section 2.3.3. Again, Fresnel reflection and transmission coefficients from Equation (2.5) have been applied, including multiple reflections by the factor M from Equation (2.6). From the resulting relation, the sample thickness can be evaluated if the total transmission is measured and the refractive indices N are known for sample and substrate, respectively.

B.2 Refractive Indices

Refractive indices N for $E_{\mathrm{h}\nu} = 2$ eV have to be known for all materials. Here, the used values are:

	N	Reference	evaluated d (nm)
graphite	2.83+1.73i	[Pal91]	32 ± 0.4
	2.73+1.4i	[GHBT69]	39.4 ± 0.4
BSCCO (68 K)	1.62+0.36i	[HTG07]	139 ± 4
BSCCO (80 K)			66 ± 4
BSCCO (85 K)			62 ± 4
BSCCO (91 K)			123 ± 2
diamond	2.4	[Pal91]	-

Different values for N have been given in the literature: Here, the values lead to differences in the evaluated sample thickness. Consequences arise concerning the applied model given by Equation (3.5), since d enters linearly to first order in the thin-film formula of Equation 2.8. Thus, the ratio of $C = d_{\mathrm{real}}/d_{\mathrm{exp}}$ changes. Here, all given values seem to be reasonable. The value from [Pal91] was used in the data evaluation even if the value from [GHBT69] would lead to $C = 1$.

Bibliography

[AAHH07] M. Aichhorn, E. Arrigoni, Z. B. Huang, and W. Hanke. Superconducting Gap in the Hubbard Model and the Two-Gap Energy Scales of High-T_c Cuprate Superconductors. *Physical Review Letters*, **99**(257002), 2007.

[All71] P. B. Allen. Electron-Phonon Effects in the Infrared Properties of Metals. *Physical Review B*, **3**(305), 1971.

[All87] P. B. Allen. Theory of Thermal Relaxation of Electrons in Metals. *Physical Review Letters*, **59**(1460), 1987.

[And07] P. W. Anderson. Is There Glue in Cuprate Superconductors? *Science*, **316**(1705), 2007.

[ARL+01] R. D. Averitt, G. Rodriguez, A. I. Lobad, J. L. W. Siders, S. A. Trugman, and A. J. Taylor. Nonequilibrium superconductivity and quasiparticle dynamics in $YBa_2Cu_3O_{7-\delta}$. *Physical Review B*, **63**(140502(R)), 2001.

[Bar72] J. Bardeen. *Electron-Phonon Interactions and Superconductivity*. Nobel Lecture, December 11, 1972.

[BBHB80] G. Binnig, A. Baratoff, H. E. Hoenig, and J. G. Bednorz. Two-Band Superconductivity in Nb-Doped $SrTiO_3$. *Physical Review Letters*, **45**(1352), 1980.

[BCS57] J. Bardeen, L. N. Cooper, and J. R. Schrieffer. Theory of Superconductivity. *Physical Review*, **108**(5), 1957.

[BHM+10] S. Berciaud, M. Y. Han, K. F. Mak, L. E. Brus, P. Kim, and T. F. Heinz. Electron and Optical Phonon Temperatures in Electrically Biased Graphene. *Physical Review Letters*, **104**(227401), 2010.

[BHR01] K.-P. Bohnen, R. Heid, and B. Renker. Phonon Dispersion and Electron-Phonon Coupling in MgB_2 and AlB_2. *Physical Review Letters*, **86**(5771), 2001.

[BLM+09] A. Barreiro, M. Lazzeri, J. Moser, F. Mauri, and A. Bachtold. Transport Properties of Graphene in the High-Current Limit. *Physical Review Letters*, **103**(076601), 2009.

[BLMM07] N. Bonini, M. Lazzeri, N. Marzari, and F. Mauri. Phonon Anharmonicities in Graphite and Graphene. *Physical Review Letters*, **99**(176802), 2007.

[BLP+01] S. L. Bud'ko, G. Lapertot, C. Petrovic, C. E. Cunningham, N. Anderson, and P. C. Canfield. Boron Isotope Effect in Superconducting MgB_2. *Physical Review Letters*, **86**(1877), 2001.

[Blu09] S. Blundell. *Superconductivity. A Very Short Introduction*. Oxford University Press, 2009.

[BM86] J.G. Bednorz and K.A. Müller. Possible High T_c Superconductivity in the Ba-La-Cu-O System. *Zeitschrift für Physik B - Condensed Matter*, **64**:189–193, 1986.

[BMH+07] S. Butscher, F. Milde, M. Hirtschulz, E. Malic, and A. Knorr. Hot Electron Relaxation and Phonon Dynamics in Graphene. *Applied Physics Letters*, **91**(203103), 2007.

[BMR+12] L. G. Booshehri, C. H. Mielke, D. G. Rickel, S. A. Crooker, Q. Zhang, L. Ren, E. H. Hároz, A. Rustagi, C. J. Stanton, Z. Jin, Z. Sun, Z. Yan, J. M. Tur, and J. Kono. Circular polarization dependent cyclotron resonance in large-area graphene in ultrahigh magnetic fields. *Physical Review B*, **85**(205407), 2012.

[BO27] M. Born and J. R. Oppenheimer. Zur Quantentheorie der Molekeln. *Annalen der Physik*, **84**(457), 1927.

[Bon07] N. Bontemps. Optical spectroscopy as a probe of gaps and kinetic electronic energy in p- and n-type cuprates. *Physica C*, **460-462**(162-165), 2007.

[BRE09] M. Breusing, C. Ropers, and T. Elsaesser. Ultrafast Carrier Dynamics in Graphene. *Physical Review Letters*, **102**(086809), 2009.

[BRR+08] N. Bonini, R. Rao, A. M. Rao, N. Marzari, and J. Menéndez. Lattice anharmonicity in low-dimensional carbon systems. *physica status solidi (b)*, **245**(2149), 2008.

[BT05] D.N. Basov and T. Timusk. Electrodynamics of high-T_c superconductors. *Reviews of Modern Physics*, **77**(721), 2005.

[BTS02] M. C. Beard, G. M. Turner, and C. A. Schmuttenmaer. Terahertz Spectroscopy. *Journal of Physical Chemistry B*, **106**(7146), 2002.

[Buc94] W. Buckel. *Supraleitung*. VCH, 5. edition, 1994.

[BWF+01] F. Bouquet, Y. Wang, R. A. Fisher, D. G. Hinks, J. D. Jorgensen, A. Junod, and N. E. Phillips. Phenomenological two-gap model for the specific heat of $\mathrm{MgB_2}$. *Europhysics Letters*, **56**(856), 2001.

[CBG+88] C. W. Chu, J. Bechthold, L. Gao, P. H. Hor, Z. J. Huang, R. L. Meng, Y. Y. Sun, Y. Q. Wang, and Y. Y. Xue. Superconductivity up to 114 K in the Bi-Al-Ca-Sr-Cu-O Compound System without Rare-Earth Elements. *Physical Review Letters*, **60**(10), 1988.

[CC03] P. C. Canfield and G. W. Crabtree. Magnesium Diboride: Better Late than Never. *Physics Today*, **3**, 2003.

[CCG+08] M. Civelli, M. Capone, A. Georges, K. Haule, O. Parcollet, T. D. Stanescu, and G. Kotliar. Nodal-Antinodal Dichotomy and the Two Gaps of a Superconducting Doped Mott Insulator. *Physical Review Letters*, **100**(046402), 2008.

[CCL03] H. J. Choi, M. L. Cohen, and S. G. Louie. Anisotropic Eliashberg theory of $\mathrm{MgB_2}$: T_c, isotope effects, superconducting energy gaps, quasiparticles, and specific heat. *Physica C*, **385**(66-74), 2003.

[Cho06] A. Cho. High T_c: The Mystery That Defies Solution. *Science*, **314**:1072–1075, 2006.

[CKI01] X. K. Chen, M. J. Konstantinovic, and J. C. Irwin. Evidence for Two Superconducting Gaps in $\mathrm{MgB_2}$. *Physical Review Letters*, **87**(157002), 2001.

[CKO+04] M. A. Carnahan, R. A. Kaindl, J. Orenstein, D. S. Chemla, S. Oh, and J. N. Eckstein. Nonequilibrium THz conductivity of $\mathrm{Bi_2Sr_2CaCu_2O_{8+\delta}}$. *Physica C*, **408-410**(729-730), 2004.

[Coo56] L. N. Cooper. Bound Electron Pairs in a Degenerate Fermi Gas. *Physical Review*, **31**(1189), 1956.

[Coo72] L. N. Cooper. *Microscopic Quantum Interference Effects in the Theory of Superconductivity*. Nobel Lecture, December 11, 1972.

[Cry] CryoVac GmbH und Co. KG, 53842 Troisdorf, Deutschland. *Bedienungsanleitung KONTI-Kryostat für Mikroskop*.

[CRY+10] R. Cortés, L. Rettig, Y. Yoshida, H. Eisaki, M. Wolf, and U. Bovensiepen. Momentum-Resolved Ultrafast Electron Dynamics in Superconducting $Bi_2Sr_2CaCu_2O_{8+\delta}$. *arXiv:1011.1171v1*, 2010.

[CSH+91] R. T. Collins, Z. Schlesinger, F. Holtzberg, C. Feild, U. Welp, G. W. Crabtree, J. Z. Liu, and Y. Fang. Dynamic properties of a high-T_c superconductor: Direct evidence for non-BCS behavior. *Physical Review B*, **43**(8701), 1991.

[CTPP03] C.-Y. Chen, T.-R. Tsai, C.-L. Pan, and R.-P. Pan. Room temperature terahertz phase shifter based on magnetically controlled birefringence in liquid crystals. *Applied Physics Letters*, **83**(4497), 2003.

[CYS+11] I. Chatzakis, H. Yan, D. Song, S. Berciaud, and T. F. Heinz. Temperature dependence of the anharmonic decay of optical phonons in carbon nanotubes and graphite. *Physical Review B*, **83**(205411), 2011.

[Czy04] G. Czycholl. *Theoretische Festkörperphysik*. Springer-Verlag Berlin Heidelberg, 2004.

[DAT+03] J. Demsar, R. D. Averitt, A. J. Taylor, V. V. Kabanov, W. N. Kang, H. J. Kim, E. M. Choi, and S. I. Lee. Pair-Breaking and Superconducting State Recovery Dynamics in MgB_2. *Physical Review Letters*, **91**(267002), 2003.

[DAT04] J. Demsar, R. D. Averitt, and A. J. Taylor. Nonequilibrium Superconductivity Probed by Time-Resolved Far-Infrared Conductivity Dynamics: Comparison Between MgB_2 and $YBa_2Cu_3O_7$. *Journal of Superconductivity: Incorporating Novel Magnetism*, **17**(143), 2004.

[DBM01] T. Dorney, R. Baraniuk, and D. Mittleman. Material parameter estimation with terahertz time-domain spectroscopy. *Journal of the Optical Society of America A*, **18**(7), 2001.

[DDS+88] M. S. Dresselhaus, G. Dresselhaus, K. Sugihara, J. L. Spain, and H. A. Goldberg. *Graphite Fibers and Filaments*. Springer, 1988.

[DG02] M. Dressel and G. Grüner. *Electrodynamics of Solids*. Cambridge University Press, 2002.

[Dru04a] P. Drude. Optische Eigenschaften und Elektronentheorie. *Annalen der Physik*, **319**(9):677, 1904.

[Dru04b] P. Drude. Optische Eigenschaften und Elektronentheorie. *Annalen der Physik*, **319**(10):936, 1904.

[DYM+10] A. Dubroka, L. Yu, D. Munzar, K. W. Kim, M. Rössle, V. K. Malik, C. T. Lin, B. Keimer, Th. Wolf, and C. Bernhard. Pseudogap and precursor superconductivity in underdoped cuprate high temperature superconductors: A far-infrared ellipsometry study. *The European Physical Journal Special Topics*, **188**(73-88), 2010.

[Eis] H. Eisaki. AIST Tsukuba Central 2. Umenzono, Tsukuba, Ibaraki 305-8568, Japan.

[Fem] Femtolasers, Floragasse 7, 1070 Wien, Österreich. *Users manual for Mirrors-dispersion-controlled Ti:Sapphire Oscillator FEMTOSOURCE COMPACT M1*.

[FM10] J. Federici and L. Moeller. Review of terahertz and subterahertz wireless communications. *Journal of Applied Physics*, **107**(111101), 2010.

[Fre31] J. Frenkel. On the Transformation of Light into Heat in Solids. *Physical Review*, **31**(1276), 1931.

[Frö50] H. Fröhlich. Theory of the Superconducting State. I. The Ground State at the Absolute Zero of Temperature. *Physical Review*, **79**(845), 1950.

[Frö52] H. Fröhlich. Interaction of Electrons with Lattice Vibrations. *Proceedings of the Royal Society of London. Series A. Mathematical and Physical Sciences*, **215**(291), 1952.

[FTMT10] S. Fabretti, P. Thomas, M. Meinert, and A. Thomas. Fabrication of superconducting MgB_2 thin films by magnetron co-sputtering on (001) MgO substrates. *arXiv:1008.3325v3*, 2010.

[FW03] A. L. Fetter and J. D. Walecka. *Quantum Theory of Many-Particle Systems*. Dover Publications, Inc., 2003.

[GCC+09] C. Giannetti, G. Coslovich, F. Cilento, G. Ferrini, H. Eisaki, N. Kaneko, M. Greven, and F. Parmigiani. Discontinuity of the ultrafast electronic response of underdoped superconducting $Bi_2Sr_2CaCu_2O_{8+\delta}$ strongly excited by ultrashort light pulses. *Physical Review B*, **79**(224502), 2009.

[GHBT69] D. L. Greenaway, G. Harbecke, F. Bassani, and E. Tosatti. Anisotropy of the Optical Constants and the Band Structure of Graphite. *Physical Review*, **178**(1340), 1969.

[GR86] E. K. U. Gross and E. Runge. *Vielteilchentheorie*. B. G. Teubner, Stuttgart, 1986.

[Gre02] W. Greiner. *Klassische Elektrodynamik*. Verlag Harri Deutsch, Frankfurt am Main, 2002.

[Gro05] E. K. U. Gross. *Vielteilchentheorie*. Lecture sommer term 2005, 2005.

[Gro06] E. K. U. Gross. *Theorie der Supraleitung*. Lecture winter term 2005/06, 2006.

[Hag05] A. Hagen. *Ladungsträgerdynamik in Kohlenstoff-Nanoröhren*. Dissertation am Fachbereich Physik der Freien Universität Berlin, 2005.

[HBTL00] R. Huber, A. Brodschelm, F. Tauser, and A. Leitenstorfer. Generation and field-resolved detection of femtosecond electromagnetic pulses tunable up to 41 THz. *Applied Physics Letters*, **76**(3191), 2000.

[HH10] R. Hackl and W. Hanke. Towards a better understanding of superconductivity at high transition temperatures. *The European Physical Journal Special Topics*, **188**(3-14), 2010.

[HHDS08] S. Hüfner, M.A. Hossain, A. Damascelli, and G.A. Sawatzky. Two Gaps Make a High-Temperature Superconductor? *arXiv:0706.4282v2*, 2008.

[HHM+11] P. J. Hale, S. M. Hornett, J. Moger, D. W. Horsell, and E. Hendry. Hot phonon decay in supported and suspended exfoliated graphene. *Physical Review B*, **83**(121404(R)), 2011.

[HJ03] D. G. Hinks and J. D. Jorgensen. The isotope effect and phonons in MgB_2. *Physica C*, **385**(98-104), 2003.

[HK08] K. Haule and G. Kotliar. Coherence-incoherence crossover in the normal state of iron-oxypnictides and importance of the Hund's rule coupling. *arXiv:0805.0722v1*, 2008.

[HM00] T. Hertel and G. Moos. Electron-phonon interaction in single-wall carbon nanotubes: A time domain study. *Physical Review Letters*, **84**(5002), 2000.

[Hol] P. Holoborodko. Smooth low-noise differentiators, www.holoborodko.com.

[HPS93] P. J. Hirschfeld, W. O. Puttika, and D. J. Scalapino. Microwave Conductivity of a d-wave superconductors. *Physical Review Letters*, **71**(3705), 1993.

[HPS94] P. J. Hirschfeld, W. O. Puttika, and D. J. Scalapino. d-wave model for microwave response of high-T_c superconductors. *Physical Review B*, **50**(250), 1994.

[HTG04] J. Hwang, T. Timusk, and G. D. Gu. High-transition-temperature superconductivity in the absence of the magnetic-resonance mode. *Nature*, **427**(714), 2004.

[HTG07] J. Hwang, T. Timusk, and G. D. Gu. Doping dependent optical properties of $Bi_2Sr_2CaCu_2O_{8+\delta}$. *Journal of Physics: Condensed Matter*, 19(125208), 2007.

[HTSC07] J. Hwang, T. Timusk, E. Schachinger, and J. P. Carbotte. Evolution of the bosonic spectral density of the high-temperature superconductor $Bi_2Sr_2CaCu_2O_{8+\delta}$. *Physical Review B*, 75(144508), 2007.

[Hub63] J. Hubbard. Electron correlations in narrow energy bands. *Proceedings of the Royal Society of London. Series A, Mathematical and Physical*, **276**(1365), Nov. 1963.

[IHK+08] K. Ishioka, M. Hase, M. Kitajima, L. Wirtz, A. Rubio, and H. Petek. Ultrafast electron-phonon decoupling in graphite. *Physical Review B*, **77**(121402(R)), 2008.

[IRH09] T. H. Isaac, J. Gómez Rivas, and E. Hendry. Optical control over transmission of terahertz radiation through arrays of subwavelength holes of varying size. *Physical Review B*, **80**(193412), 2009.

[ITY+11] Y. Ishida, T. Togashi, K. Yamamoto, M. Tanaka, T. Taniuchi, T. Kiss, M. Nakajima, T. Suemoto, and S. Shin. Non-thermal hot electrons ultrafastly generating hot optical phonons in graphite. *Scientific Reports*, **1**(64), 2011.

[JD73] L. G. Johnson and G. Dresselhaus. Optical Properties of Graphite. *Physical Review B*, **7**(2275), 1973.

[JDK+06] B. B. Jin, T. Dahm, F. Kadlec, P. Kuzel, A. I. Gubin, E.-M. Choi, H. J. Kim, S.-I. Lee, W. N. Kang, S. F. Wang, Y. L. Zhou, A. V. Pogrebnyakov, J. M. Redwing, X. X. Xi, and N. Klein. Microwave and Terahertz Surface Resistance of MgB_2 Thin Films. *Journal of Superconductivity and Novel Magnetism*, **19**(617), 2006.

[JKK+05] B. B. Jin, P. Kuzel, F. Kadlec, T. Dahm, J. M. Redwing, A. V. Pogrebnyakov, X. X. Xi, and N. Klein. Terahertz surface impedance of epitaxial MgB_2 thin films. *Applied Physics Letters*, **87**(092503), 2005.

[KACS10] K. Kang, D. Abdula, D. G. Cahill, and M. Shim. Lifetimes of optical phonons in graphene and graphite by time-resolved incoherent anti-Stokes Raman scattering. *Physical Review B*, **81**(165405), 2010.

[KAK+09] S. Kumar, M. Anija, N. Kamaraju, K. S. Vasu, K. S. Subrahmanyam, A. K. Sood, and C. N. R. Rao. Femtosecond carrier dynamics and saturable absorption in graphene suspensions. *Applied Physics Letters*, **95**(191911), 2009.

[Kam05] T. Kampfrath. *Charge-Carrier Dynamics in Solids and Gases Observed by Time-Resolved Terahertz Spectroscopy*. Doktorarbeit am Fachbereich Physik der Freien Universität Berlin, 2005.

[KCC+05] R. A. Kaindl, M. A. Carnahan, D. S. Chemla, S. Oh, and J. N. Eckstein. Dynamics of Cooper pair formation in $Bi_2Sr_2CaCu_2O_{8+\delta}$. *Physical Review B*, **72**(060510(R)), 2005.

[KCO+02] R. A. Kaindl, M. A. Carnahan, J. Orenstein, D. S. Chemla, H. M. Christen, H.-Y. Zhai, M. Paranthaman, and D. H. Lowndes. Far-Infrared Optical Conductivity Gap in Superconducting MgB_2 Films. *Physical Review Letters*, **88**(027003), 2002.

[KDJA01] Y. Kong, O. V. Dolgov, O. Jepson, and O. K. Andersen. Electron-phonon interaction in the normal and superconducting states of MgB_2. *Physical Review B*, **64**(020501(R)), 2001.

[KEWE99] R. A. Kaindl, F. Eickemeyer, M. Woerner, and T. Elsaesser. Broadband phase-matched difference frequency mixing of femtosecond pulses in GaSe: Experiment and theory. *Applied Physics Letters*, **75**(1060), 1999.

[KH07] K. Kopitzki and P. Herzog. *Einführung in die Festkörperphysik*. B. G. Teubner Verlag, Wiesbaden, 5. edition, 2007.

[KLK+08] H.-H. Klauss, H. Luetkens, R. Klingeler, C. Hess, F. J. Litterst, M. Kraken, M. M. Korshunov, I. Eremin, S.-L. Drechsler, R. Khasanov, A. Amato, J. Hamann-Borrero, N. Leps, A. Kondrat, G. Behr, J. Werner, and B. Büchner. Commensurate Spin Density Wave in LaOFeAs: A Local Probe Study. *arXiv:0805.0264v1*, 2008.

[KNW07] T. Kampfrath, J. Nötzold, and M. Wolf. Sampling of broadband terahertz pulses with thick electro-optic crystals. *Applied Physics Letters*, **90**(231113), 2007.

[KO08] H. Kamerlingh-Onnes. Experiments on the condensation of helium by expansion. *KNAW, Proceedings 10 II,1907-1908, Comm. Leiden, Amsterdam*, **108**:744–747, 1908.

[KO11a] H. Kamerlingh-Onnes. Further experiments with liquid helium. C. On the change of electric resistance of pure metals at very low temperatures etc. IV. The resistance of pure mercury at helium temperatures. *KNAW, Proceedings 13 II,1910-1911, Comm. Leiden, Amsterdam*, **122b**:744–747, 1911.

[KO11b] H. Kamerlingh-Onnes. Further experiments with liquid helium. D. On the change of electric resistance of pure metals at very low temperatures etc. V. The disappearance of the resistance of mercury. *KNAW, Proceedings 14 I,1911, Comm. Leiden, Amsterdam*, **124c**:113–115, 1911.

[KO12] H. Kamerlingh-Onnes. Further experiments with liquid helium. G. On the electric resistance of pure metals at very low temperatures etc. VI. On the sudden change in the rate at which the resistency of mercury disappeares. *KNAW, Proceedings 14 II,1911-1912, Comm. Leiden, Amsterdam*, 818-821, 1912.

[Koh59] W. Kohn. Image of the Fermi Surface in the Vibration Spectrum of a Metal. *Physical Review Letters*, **2**(393), 1959.

[KPS+05] T. Kampfrath, L. Perfetti, F. Schapper, C. Frischkorn, and M. Wolf. Strongly Coupled Optical Phonons in the Ultrafast Dynamics of the Electronic Energy and Current Relaxation in Graphite. *Physical Review Letters*, **95**(187403), 2005.

[KWE+00] R. A. Kaindl, M. Woerner, T. Elsaesser, D. C. Smith, J. F. Ryan, G. A. Farnan, M. P. McCurry, and D. G. Walmsley. Ultrafast Mid-Infrared Response of $YBa_2Cu_3O_{7-\delta}$. *Science*, **287**(470), 2000.

[Leg07] A. J. Leggett. *Quantum Liquids*. Oxford University Press, 2007.

[Lev07] B. Goss Levi. New experiments fuel debate over the nature of high T_c- superconductors. *Physics Today*, **60**(12), 2007.

[LLC+08] W. X. Li, Y. Li, R. H. Chen, R. Zeng, M. Y. Zhu, H. M. Jin, and S. X. Dou. Electron-phonon coupling properties in MgB_2 observed by Raman scattering. *Journal of Physics: Condensed Matter*, **20**(255235), 2008.

[LNW06] P. A. Lee, N. Nagaosa, and X.-G. Wen. Doping a Mott insulator: Physics of high-temperature superconductivity. *Reviews of Modern Physics*, **78**(17), 2006.

[LvdLK71] A. Laubereau, D. von der Linde, and W. Kaiser. Decay Time of Hot Phonons in Diamond. *Physical Review Letters*, **27**(12), 1971.

[MA03] I. I. Mazin and V. P. Antropov. Electronic structure, electron-phonon coupling, and multiband effects in MgB_2. *Physica C*, **385**(49-65), 2003.

[Max50] E. Maxwell. Isotope Effect in the Superconductivity of Mercury. *Physical Review*, **78**(487), 1950.

[MBB07] J. Moser, A. Barreiro, and A. Bachtold. Current-induced cleaning of graphene. *Applied Physics Letters*, **91**(163513), 2007.

[McC57] J. W. McClure. Band Structure of Graphite and de Haas-van Alphen Effect. *Physical Review*, **108**(612), 1957.

[MGF+01] G. Moos, C. Gahl, R. Fasel, M. Wolf, and T. Hertel. Anisotropy of Quasiparticle Lifetimes and the Role of Disorder in Graphite from Ultrafast Time-Resolved Photoemission Spectroscopy. *Physical Review Letters*, **87**(267402), 2001.

[Mil06] A.J. Millis. Gaps and Our Understanding. *Science*, **314**:1888–1889, 2006.

[MMD80] E. Mendez, A. Misu, and M. Dresselhaus. Magnetoreflection study of graphite under pressure. *Physical Review B*, **21**(827), 1980.

[Mot49] N. F. Mott. The Basis of the Electron Theory of Metals, with Special Reference to the Transition Metals. *Proceedings of the Physical Society (London) Section A*, **62**(416), 1949.

[MPB08] A. Melnikov, A. Povolotskiy, and U. Bovensiepen. Magnon-Enhanced Phonon Damping at Gd(0001) and Tb(0001) Surfaces Using Femtosecond Time-Resolved Optical Second-Harmonic Generation. *Physical Review Letters*, **100**(247401), 2008.

[MRT+04] J. Maultzsch, S. Reich, C. Thomsen, H. Requardt, and P. Ordejón. Phonon Dispersion in Graphite. *Physical Review Letters*, **92**(075501), 2004.

[MTFA88] H. Maeda, Y. Tanaka, M. Fukutomi, and T. Asano. A New High-T_c Oxide Superconductor without a Rare Earth Element. *Japanese Journal of Applied Physics*, **27**(L209), 1988.

[MWBK11] E. Malic, T. Winzer, E. Bobkin, and A. Knorr. Microscopic theory of absorption and ultrafast many-particle kinetics in graphene. *Physical Review B*, **84**(205406), 2011.

[NDSvD09] R. W. Newson, J. Dean, B. Schmidt, and H. M. van Driel. Ultrafast carrier kinetics in exfoliated graphene and thin graphite films. *Optics Express*, **17**(2326), 2009.

[NGM+04] K. S. Novoselev, A. K. Geim, S. V. Morozov, D. Jiang, Y. Zhang, S. V. Dubonos, I. V. Grigorieva, and A. A. Firsov. Electric Field Effect in Atomically Thin Carbon Films. *Science*, **306**(666), 2004.

[NGP+09] A. H. Casto Neto, F. Guinea, N. M. R. Peres, K. S. Novoselov, and A. K. Geim. The electronic properties of graphene. *Reviews of Modern Physics*, **81**(109), 2009.

[NNM+01] J. Nagamatsu, N. Nakagawa, T. Muranaka, Y. Zenitani, and J. Akimitsu. Superconductivity at 39 K in magnesium diboride. *Nature*, **410**(63), 2001.

[Nöt07] J. Nötzold. *Ultraschnelle Entmagnetisierung laserangeregter Ferromagneten untersucht mit zeitaufgelöster Terahertz-Emissions-Spektroskopie*. Diplomarbeit am Fachbereich Physik der Universität Konstanz, 2007.

[NPK] M. R. Norman, D. Pines, and C. Kallin. The pseudogap: friend or foe of high T_c? *Advances in Physics*, **54**.

[OBM+97] M. Ohler, J. Baruchel, A. W. Moore, P. Galez, and A. Freund. Direct Observation of Mosaic Blocks in Highly Oriented Pyrolytic Graphite. *Nuclear Instruments and Methods in Physics Research B*, **129**(257), 1997.

[ODC+08] M. Ortolani, P. Dore, D. Di Castro, A. Perucchi, S. Lupi, V. Ferrando, M. Putti, I. Pallecchi, C. Ferdighini, and X. X. Xi. Two-band parallel conductivity Gap at terahertz frequencies in the superconducting state of MgB_2. *Physical Review B*, **77**(100507(R)), 2008.

[OeYK+06] M. Oh-e, H. Yokoyama, M. Koeberg, E. Hendry, and M. Bonn. High-frequency dielectric relaxation of liquid crystals: THz time-domain spectroscopy of liquid crystal colloids. *Optics Express*, **14**(11433), 2006.

[Ohk07] F. J. Ohkawa. Origin and roles of a strong electron-phonon interaction in cuprate oxide superconductors. *arXiv:0701088v1*, 2007.

[Orb67] R. Orbach. Phonon Breakdown. *IEEE transctions on sonics and ultrasonics*, **14**(140), 1967.

[PAK07] T. Papenkort, V. M. Axt, and T. Kuhn. Coherent dynamics and pump-probe spectra of BCS superconductors. *Physical Review B*, **76**(224522), 2007.

[Pal] Ecole Polytechnique. 91128 Palaiseau cedex, France.

[Pal91] E.D. Palik. *Handbook of Optical Constants of Solids II*. Academic Press, 1991.

[PDJ+03] A. Perucchi, L. Degiorgi, J. Jun, M. Angst, and J. Karpinski. Far-infrared optical properties of MgB_2 single crystals. *Physica C*, **385**(273-277), 2003.

[Ped03] T. G. Pedersen. Analytic calculation of the optical properties of graphite. *Physical Review B*, **67**(113106), 2003.

[Phi77] H. R. Philipp. Infrared optical properties of graphite. *Physical Review B*, **16**(2896), 1977.

[Pic89] W. E. Pickett. Electronic structure of the high-temperature oxide superconductors. *Review of Modern Physics*, **61**(2), 1989.

[PKA08] T. Papenkort, T. Kuhn, and V. M. Axt. Coherent control of the gap dynamics of BCS superconductors in the nonadiabatic regime. *Physical Review B*, **78**(132505), 2008.

[PKA09] T. Papenkort, T. Kuhn, and V. M. Axt. Ultrafast coherent dynamics in optically driven BCS systems. *Physica status solidi B*, **246**(325), 2009.

[PKG+09] P. Plochocka, P .Kossacki, A. Golnik, T. Kazimierczuk, C. Berger, W. A. de Heer, and M. Potemski. Slowing hot-carrier relaxation in graphene using a magnetic field. *Physical Review B*, **80**(245415), 2009.

[PL91] C. Priester and M. Lannoo. Analog of the $\boldsymbol{k} \cdot \boldsymbol{p}$ Theory for a Localized-Orbital Description of the Band Structure of Zinc-Blende-Structure Semiconductors. *Physical Review B*, **44**(10559), 1991.

[PLL+07] L. Perfetti, P. A. Loukakos, M. Lisowski, U. Bovensiepen, H. Eisaki, and M. Wolf. Ultrafast Electron Relaxation in Superconducting $\mathrm{Bi_2Sr_2CaCuO_{8+\delta}}$ by Time-Resolved Photoelectron Spectroscopy. *Physical Review Letters*, **99**(197001), 2007.

[PLM+04] S. Piscanec, M. Lazzeri, F. Mauri, A. C. Ferrari, and J. Robertson. Kohn Anomalies and Electron-Phonon Interaction in Graphite. *Physical Review Letters*, **93**(185503), 2004.

[Por07] M. Porfath. *Numerical Study of Quantum Transport in Carbon Nanotube Based Transistors*. Dissertation eingereicht an der Technischen Universität Wien Fakultät für Elektrotechnik und Informationstechnik, 2007.

[PPB+10] A. Pashkin, M. Porer, M. Beyer, K. W. Kim, A. Dubroka, C. Bernhard, X. Yao, Y. Dagan, R. Hackl, A. Erb, J. Demsar, R. Huber, and A. Leitenstorfer. Femtosecond Response of Quasiparticles and Phonons in Superconducting $\mathrm{YBa_2Cu_3O_{7-\delta}}$ Studied by Wideband Terahertz Spectroscopy. *Physical Review Letters*, **105**(067001), 2010.

[PWK07] I. Pupeza, R. Wilk, and M. Koch. Highly accurate optical material parameter determination with THz time-domain spectroscopy. *Optics Express*, **15**(4335), 2007.

[QLYT02] J. W. Quilty, S. Lee, A. Yamamoto, and S. Tajima. Superconducting Gap in $\mathrm{MgB_2}$: Electronic Raman Scattering Measurements of Single Crystals. *Physical Review Letters*, **88**(087001), 2002.

[QTK+99] M. A. Quijada, D. B. Tanner, R. J. Kelley, M. Onellion, H. Berger, and G. Margaritondo. Anisotropy in the ab-plane optical properties of $Bi_2Sr_2CaCu_2O_8$ single-domain crystals. *Physical Review B*, 60(21), 1999.

[RKF+98] F. Ronning, C. Kim, D. L. Feng, D. S. Marshall, A. G. Loeser, L. L. Miller, J. N. Eckstein, I. Bozovic, and Z.-X. Shen. Photoemission Evidence for a Remnant Fermi Surface and a d-Wave-Like Dispersion in Insulating $\mathrm{Ca_2CuO_2Cl_2}$. *Science*, **282**(2067), 1998.

[RSC+91] L. D. Rotter, Z. Schlesinger, R. T. Collins, F. Holtzberg, C. Field, U. W. Welp, G. W. Crabtree, J. Z. Liu, Y. Fang, K. G. Vandervoort, and S. Fleshler. Dependence of the Infrared Properties of Single-Domain $\mathrm{YBa_2Cu_3O_{7-y}}$ on Oxygen Content. *Physical Review Letters*, **67**(2741), 1991.

[RSC+92] L. D. Rotter, Z. Schlesinger, R. T. Collins, F. Holtzberg, C. Field, U. W. Welp, G. W. Crabtree, Y. Fang, K. G. Vandervoort, S. Fleshler, and J. Z. Liu. Properties of the Normal and Superconducting States of High-T_c Superconductors Determined by the Infrared Conductivity. *Chinese Journal of Physics*, **30**(271), 1992.

[RSWN50] C. A. Reynolds, B. Serin, W. H. Wright, and L. B. Nesbit. Superconductivity of Isotopes of Mercury. *Physical Review*, **78**(477), 1950.

[Rul98] C. Rullière. *Femtosecond Laser Pulses. Principles and Experiments*. Springer-Verlag Berlin Heidelberg, 1998.

[Sch72] J. R. Schrieffer. *Macroscopic Quantum Phenomena from Pairing in Superconductors*. Nobel Lecture, December 11, 1972.

[Sch05] F. Schapper. *THz-Spektroskopie von Graphit und Erzeugung geformter Laserpulse im mittleren Infrarot*. Diplomarbeit am Fachbereich Physik der Freien Universität Berlin, 2005.

[Sch08] M. Scheuch. *Ladungsträgerdynamik in hochkorrelierten Elektronensystemen untersucht mit zeitaufgelöster THz-Spektroskopie*. Diplomarbeit am Fachbereich Physik der Freien Universität Berlin, 2008.

[SCK+90] K. Seibert, G. C. Cho, W. Kütt, H. Kurz, D. H. Reitze, J. I. Dadap, H. Ahn, M. C. Downer, and A. M. Malvezzi. Femtosecond carrier dynamics in graphite. *Physical Review B*, **42**(2842), 1990.

[SKW+11] M. Scheuch, T. Kampfrath, M. Wolf, K. von Volkmann, C. Frischkorn, and L. Perfetti. Temperature dependence of ultrafast phonon dynamics in graphite. *Applied Physics Letters*, **99**(211908), 2011.

[SLZ11] S. Schäfer, W. Liang, and A. H. Zewail. Primary structural dynamics in graphite. *New Journal of Physics*, **13**(063030), 2011.

[SMW59] H. Suhl, B. T. Matthias, and L. R. Walker. Bardeen-Cooper-Schrieffer Theory of Superconductivity in the Case of Overlapping Bands. *Physical Review Letters*, **3**(552), 1959.

[Söl] J. Sölle. Mathematisch-Naturwissenschaftliche Fakultät I, Institut für Physik, Brook-Taylor Str. 6,. Humboldt Universität Berlin.

[SW58] J. C. Slonczewski and P. R. Weiss. Band Structure of Graphite. *Physical Review*, **109**(272), 1958.

[TBS+95] J. L. Tallon, C. Bernhard, H. Shaked, R. L. Hitterman, and J. D. Jorgensen. Generic superconducting phase behaviour high-T_c: T_c variation with hole concentration in $\mathrm{YBa_2Cu_3O_{7-\delta}}$. *Phys. Rev. B*, **51**(18), 1995.

[TH90] U. Teschner and K. Hübner. IR-Spectroscopic Data of Thin Insulating Films on Semiconductors. *phys. stat. sol. (b)*, **159**(917), 1990.

[THM+11] M. Theuer, S. S. Harsha, D. Molter, G. Torosyan, and R. Beigang. Terahertz Time-Domain Spectroscopy of Gases, Liquids and Solids. *European Journal of Chemical Physics and Physical Chemistry*, **12**(2695-2705), 2011.

[TLL+06] K. Tanaka, W. S. Lee, D. H. Lu, A. Fujimori, T. Fujii, Risdiana, I. Terasaki, D. J. Scalapino, T. P. Devereaux, Z. Hussain, and Z.-X. Shen. Distinct Fermi-Momentum-Dependent Energy Gaps in Deeply Underdoped Bi2212. *Science*, **314**(165107), 2006.

[TR82] R. C. Tatar and S. Rabii. Electronic properties of graphite: A unified theoretical study. *Physical Review B*, **25**(4126), 1982.

[TSS+01] T. Takahashi, T. Sato, S. Souma, T. Muranaka, and J. Akimitsu. High-Resolution Photoemission Study of $\mathrm{MgB_2}$. *Physical Review Letters*, **86**(4915), 2001.

[TYK+01] S. Tsuda, T. Yokoya, T. Kiss, Y. Takano, K. Togano, H. Kito, H. Ihara, and S. Shin. Evidence for a Multiple Superconducting Gap in $\mathrm{MgB_2}$ from High-Resolution Photoemission Spectroscopy. *Physical Review Letters*, **87**(177006), 2001.

[UTS+03] H. Uchiyama, S. Tajima, K. M. Shen, D. H. Lu, and Z.-X. Shen. Photoemission studies in $\mathrm{MgB_2}$. *Physica C*, **385**(85-90), 2003.

[vdMMZ+03] D. van der Marel, H. J. A. Molegraaf, J. Zaanen, Z. Nussinov, F. Carbone, A. Damascelli, H. Eisaki, M. Greven, P. H. Kes, and M. Li. Quantum critical behaviour in a high-T_c superconductor. *Nature*, **425**(271), 2003.

[vL49] M. von Laue. *Theorie der Supraleitung*. Springer-Verlag, 2. edition, 1949.

[vV04] K. von Volkmann. *Charakterisierung komplex geformter, verstärkter Laserpulse mit einem Differenzfrequenz-XFROG-Aufbau*. Diplomarbeit am Fachbereich Physik der Freien Universität Berlin, 2004.

[vV09] K. von Volkmann. *Ultraschnelle Relaxationsdynamik über Phononen-Wechselwirkungen in Festkörpersystemen*. Dissertation am Fachbereich Physik der Freien Universität Berlin, 2009.

[Wal47] P. R. Wallace. The Band Theory of Graphite. *Physical Review*, **71**(9), 1947.

[WAT+87] M. K. Wu, J. R. Ashburn, C. J. Torng, P. H. Hor, R. L. Meng, L. Gao, Z. J. Huang, Y. Q. Wang, and C. W. Chu. Superconductivity at 93 K in a New Mixed-Phase Y-Ba-Cu-O Compound System at Ambient Pressure. *Physical Review Letters*, **58**(9), 1987.

[Web09] M. Weber. *Terahertz Transmission Spectroscopy of the Organic Polymer PEDOT:PSS*. Diplomarbeit am Fachbereich Physik der Freien Universität Berlin, 2009.

[WKM10] T. Winzer, A. Knorr, and E. Malic. Carrier Multiplication in Graphene. *Nano Letters*, **10**(4839), 2010.

[WOP+11] S. Winnerl, M. Orlita, P. Plochocka, P. Kossacki, M. Potemski, T. Winzer, E. Malic, A. Knorr, M. Sprinkle, C. Berger, W. A. de Heer, H. Schneider, and M. Helm. Carrier Relaxation in Epitaxial Graphene Photoexcited Near the Dirac Point. *Physical Review Letters*, **107**(237401), 2011.

[WR04] L. Wirtz and A. Rubio. The phonon dispersion of graphite revisited. *Solid State Communication*, **131**(141), 2004.

[WSG+10] H. Wang, J. H. Strait, P. A. George, S. Shivaraman, V. B. Shields, M. Chandrashekhar, J. Hwang, F. Rana, M. G. Spencer, C. S. Ruiz-Vargas, and J. Park. Ultrafast relaxation dynamics of hot optical phonons in graphene. *Applied Physics Letters*, **96**(081917), 2010.

[YGL+01] T. Yildirim, O. Gülseren, J. W. Lynn, C. M. Brown, T. J. Udovic, Q. Huang, N. Rogado, K. A. Regan, M. A. Hayward, J. S. Slusky, T. He, M. K. Haas, P. Khalifah, K. Inumaru, and R. J. Cava. Giant Anharmonicity and Nonlinear Electron-Phonon Coupling in MgB_2: A Combined Firts-Principles Calculation and Neutron Scattering Study. *Physical Review Letters*, **87**(037001), 2001.

[YLC+12] H. Yan, X. Li, B. Chandra, G. Tulevski, Y. Wu, M. Freitag, W. Zhu, P. Avouris, and F. Xia. Tunable infrared plasmonics devices using graphene/insulator stacks. *Nature Nanotechnology*, **7**(330), 2012.

[YSM+09] H. Yan, D. Song, K. F. Mak, I. Chatzakis, J. Maultzsch, and T. F. Heinz. Time-resolved Raman spectroscopy of optical phonons in graphite: Phonon anharmonic coupling and anomalous stiffening. *Physical Review B*, **80**(121403(R)), 2009.

Publications

M. Scheuch, T. Kampfrath, M. Wolf, K. von Volkmann, C. Frischkorn, and L. Perfetti. *Temperature dependence of ultrafast phonon dynamics in graphite.* Applied Physics Letters **99**, 211908 (2011).

M. Scheuch, M. Wolf, K. von Volkmann, C. Frischkorn, L. Perfetti, and T. Kampfrath. *Mid-infrared optical properties of equilibrium and photoexcited graphite: Competition of direct and indirect optical transitions.* Physical Review B (in preparation).

Deutsche Kurzfassung

In dieser Arbeit wurde THz-Spektroskopie genutzt um einerseits Graphit temperaturabhängig zu untersuchen, andererseits supraleitende Materialen wie das Kuprat $Bi_2Sr_2CaCu_2O_{8+\delta}$ und der BCS-Supraleiter MgB_2. Im Halbmetall Graphit führt die sich stark um die Fermi-Energie herum ändernde elektronische Zustandsdichte zu einer starken Temperaturabhängigkeit der niederenergetischen elektronischen Anregungen. Hinzu kommt die starke Kopplung nur weniger Phononenmoden, die die Energierelaxation bestimmen. Für alle Arten von Supraleitern ist die Bandlücke unterhalb der kritischen Temperatur T_c charakteristisch und in der Größenordnung von 10 meV. Damit ist THz-Spektroskopie für diese Systeme hervorragend geeignet, um sowohl Gleichgewichtseigenschaften zu untersuchen als auch die Energierelaxation nach Anregung mit einem sichtbaren Laserpuls.

Graphit zeigt im Gleichgewicht einen starken Absorptionsrückgang im gemessenen Bereich von 12-26 THz. Dieser ist auf ein Blockieren von direkten optischen Übergängen durch bereits thermisch angeregte Elektronen zurückzuführen. Im Gegensatz hierzu kann eine Zunahme der indirekten optischen Übergänge beobachtet werden, die jedoch das Ausbleichen aufgrund blockierter direkter Übergange nicht ausgleichen können. Im Zusammenhang damit wird ein starker Anstieg sowohl der Plasmafrequenz als auch der Drude-Streurate mit steigender Temperatur beobachtet. Diese Abhängigkeit läßt sich im Fall der Plasmafrequenz über die elektronische Zustandsdichte von Graphit um die Fermi-Energie herum modellieren.

Photoangeregtes Graphit zeigt ebenfalls ein Ausbleichen bei THz-Frequenzen über 15 THz. Bei tiefen Temperaturen ist dieser Effekt wesentlich stärker ausgeprägt, da hier thermisch angeregte Elektronen weniger zur Probenantwort beitragen. Photoanregung führt zu einem ultraschnellen Thermalisieren der Elektronen untereinander innerhalb von wenigen 100 fs, wie es bei Metallen zu erwarten ist. Das wird durch ein rein thermisches Verhalten der Nichtgleichgewichts-Plasmafrequenz unabhängig von der Probentemperatur untermauert. Im Gegensatz hierzu ist die Drude-Streurate nach Photoanregung stark von der Probentemperatur abhängig. Theoretische Modellierung zeigt, daß hierfür die stärkeren Ungleichgewichte der Elektronenverteilung bei niederen Temperaturen verantwortlich sind. Durch wenig angeregte Ladungsträger bei tiefen Temperaturen treten höhere Anregungsdichten pro Elektron auf und führen zu höheren elektronischen Temperaturen unmittelbar nach der Anregung.

Interessanterweise können in Graphit mit zeitaufglöster THz-Spektroskopie auch Phononen-Streuprozesse beobachtet werden. Dies ist möglich, da die thermalisierten Elektronen auch im Gleichgewicht mit einigen wenigen stark gekoppelten optischen Phononenmoden (SCOPs) sind, während das restliche Gitter noch kalt ist. Auf einer Pikosekunden-Zeitskala streuen diese SCOPs mit anderen Phononenmoden. Dabei zeigt sich eine charakteristische Temperaturabhängigkeit der Streuraten, die nur mit Zerfällen in niederenergetische (thermische) Phononenmoden zu erklären ist. Solche Zerfälle sind aber nur für eine langlebige SCOP-Mode (A_1'-Mode am K-Punkt) unter Einhaltung der Energie- und Impulserhaltung möglich, die damit auch die Relaxation bestimmt.

Sowohl der Kuprat-Supraleiter $Bi_2Sr_2CaCu_2O_{8+\delta}$ als auch der BCS-Supraleiter MgB_2 zeigen unterhalb von T_c ein starkes Ausbleichen. Dieses ist über das Öffnen der supraleitenden Bandlücke erklärt. Durch die gewählte hohe Temperaturauflösung gibt es klare Anzeichen für einen zweiten Phasenübergang in die Pseudogap-Phase bei $Bi_2Sr_2CaCu_2O_{8+\delta}$. Zwar läßt sich der Verlauf der Elektronenstreurate im Pseudogap-Bereich über vorgeformte Cooper-Paare deuten, die nur wenig zur Temperaturabhängigkeit beitragen, jedoch steht der erhaltene Verlauf des Phasendiagrams dem entgegen, da die Pseudogap nur im unterdotierten Bereich existiert. Dieses Verhalten spricht für getrennte Ursachen dieser beiden Phasen. Photoanregung unterhalb von T_c führt bei $Bi_2Sr_2CaCu_2O_{8+\delta}$ zu einem Anwachsen der THz-Absorption, daß über die Anregung von Quasiteilchen erklärt wird. Das pumpinduzierte Signal kann aber auch verwendet werden, um Informationen über Gleichgewichtszustände zu erhalten, da vor Erreichen des nächsten Anregungspulses die Probe zwar thermalisiert aber noch nicht vollständig relaxiert.

Erstmals konnten dünne MgB_2-Filme auf den THz-transparenten Substraten Silizium und Diamant in einer Kooperation mit der Universität Bielefeld gewachsen werden, die ein entsprechend hohes T_c aufweisen um THz-Messungen an ihnen durchzuführen. Es wird so möglich BCS-Supraleiter auch bei Anregungsenergien im Bereich der supraleitenden Bandlücke zu untersuchen und die gewonnenen Ergebnisse mit denen anderer supraleitender Materialen zu vergleichen. Hierbei sollten Rückschlüsse auf die supraleitenden Mechanismen z.B. im Fall der Kuprate möglich sein. Für MgB_2 wurde die Sprungtemperatur und die Größe der größeren Bandlücke kontaktfrei bestimmt. Im Gegensatz zu $Bi_2Sr_2CaCu_2O_{8+\delta}$ sinkt die Elektronenstreurate unterhalb von T_c wesentlich stärker ab, da in BCS-Supraleitern alle Elektronen in den kohärenten Zustand kondensieren.

Curriculum vitae

For reasons of data protection, the curriculum vitae is not included in the online version.

Danksagung

Hier ist jetzt der Ort, an dem allen Personen gedankt werden soll, die zum Gelingen dieser Arbeit beigetragen haben.

An erster Stelle steht hier Martin Wolf, dem ich für die Möglichkeit danke, in seiner Arbeitsgruppe diese Arbeit anfertigen zu können, seine vielen Tipps und Anregungen, die einem meistens viel Arbeit erspart haben sowie die nach wie vor unglaubliche Laborausstattung. Auch die ganze Arbeitsgruppe/Abteilung verdient ein großes Dankeschön - geht nicht, gibt's nicht! Weiter danke ich

Karsten Heyne, der sich spontan als Zweitgutachter zur Verfügung gestellt hat und immer die richtigen Fragen parat hatte;

Tobias Kampfrath, der ein schier unerschöpfliches Wissen über THz und Graphit in sich trägt, immer zu Diskussionen (nicht nur über Physik) bereit war und diese Arbeit mit viel konstruktiver Kritik verbessert hat;

Christian Frischkorn für die großen Freiheiten und das Vertrauen aber auch für alles andere, dass das Arbeiten zumeist sehr entspannt gemacht hat;

Konrad von Volkmann für die perfekte Zusammenarbeit im Labor, ohne die diese ganzen Messungen nicht möglich gewesen wären;

Toru Shimada, meinem Lieblingsbüromitbewohner und Begleiter bei unzähligen Messnächten (Du kannst jetzt die Pumpe starten!);

Philipp Giese und Harald Kirsch, bei denen man auch mal Dampf ablassen konnte und die diverse Nächte bei Frühjahrstagungen mit mir überstanden haben;

Joachim Lehnert und Sabine Wasle für die unglaubliche Hilfsbereitschaft in allem, was das Leben am FHI so ausmacht - ich werde euch auch sicher nie wieder fragen, ob irgendwelche Katastrophen passiert sind...;

Dietgard Mallwitz, Peter West und Reinhard Franke, die Verwaltung und Technik immer im Griff hatten und so dazu beitrugen haben, dass ich mich auch hin und wieder der Wissenschaft widmen konnte;

Uwe Bovensiepen für seine begeisternde Art, seinen Humor und dafür, dass er immer die richtigen Antworten zum richtigen Zeitpunkt hatte;

Laura Foglia dafür, dass sie nicht nur immer die Dinge im Labor hatte, die ich gerade brauchte,

sondern auch dafür, dass ich alles immer gleich mitnehmen konnte;

Savio Fabretti für die aufwendige Herstellung der MgB_2-Proben und die hervorragende Zusammenarbeit - leider haben die Pump-Probe-Messungen vor dem Umzug nicht mehr geklappt;

Torben Winzer und Ermin Malic von der TU Berlin, dank denen ich endlich verstanden habe, was mein Graphit so alles treibt;

Silke Hutt für die unglaublichen Leistungen beim Korrekturlesen dieses Wälzers und natürlich insbesondere für das *lest*;

Anja Schillhaneck für Brüssel, Hoffnung und vieles andere mehr;

1987,4 und dem kleinen glücklichen Elephanten für unzählige Abende mit meist mehr Fragen als Antworten;

allen im *Celtic Cottage* für die ungezählten schönen Stunden und die Rundumversorgung in den letzten Monaten mit Nahrung in fester und flüssiger Form, insbesondere zu Frühstückszeiten - ohne euch wäre ich wohl verhungert;

Marijke, die großen Anteil an dieser Arbeit hat, einfach dadurch, dass sie immer für Gespräche über Wissenschaft zu haben war, nie aber über Physik;

natürlich Nadine, Daniel, Lars, Peter, Francis und Hauke die meine Eigenheiten stoisch ertragen haben und immer bei Problemen angerufen werden konnten - auch nachts;

Kristin - wenn heute noch was schief gehen kann, sag Bescheid!

Zuguterletzt danke ich meiner Familie, die stets für mich da war, gerade auch in schwierigen Zeiten - von denen es reichlich gab - und wenn ich wieder mal auf dem Zahnfleisch angekrochen kam.

Erklärung gemäß Paragraph 7 Abs. 4 der Promotionsordnung

Hiermit versichere ich, daß diese Arbeit von niemandem anderen als mir angefertigt wurde. Alle verwendeten Hilfsmittel wurden angegeben. Zitate und Abbildungen aus fremden Arbeiten sind als solche kenntlich gemacht. Diese Arbeit wurde bisher in gleicher oder ähnlicher Form keiner anderen Prüfungskommission vorgelegt und auch nicht veröffentlicht.

Berlin, den